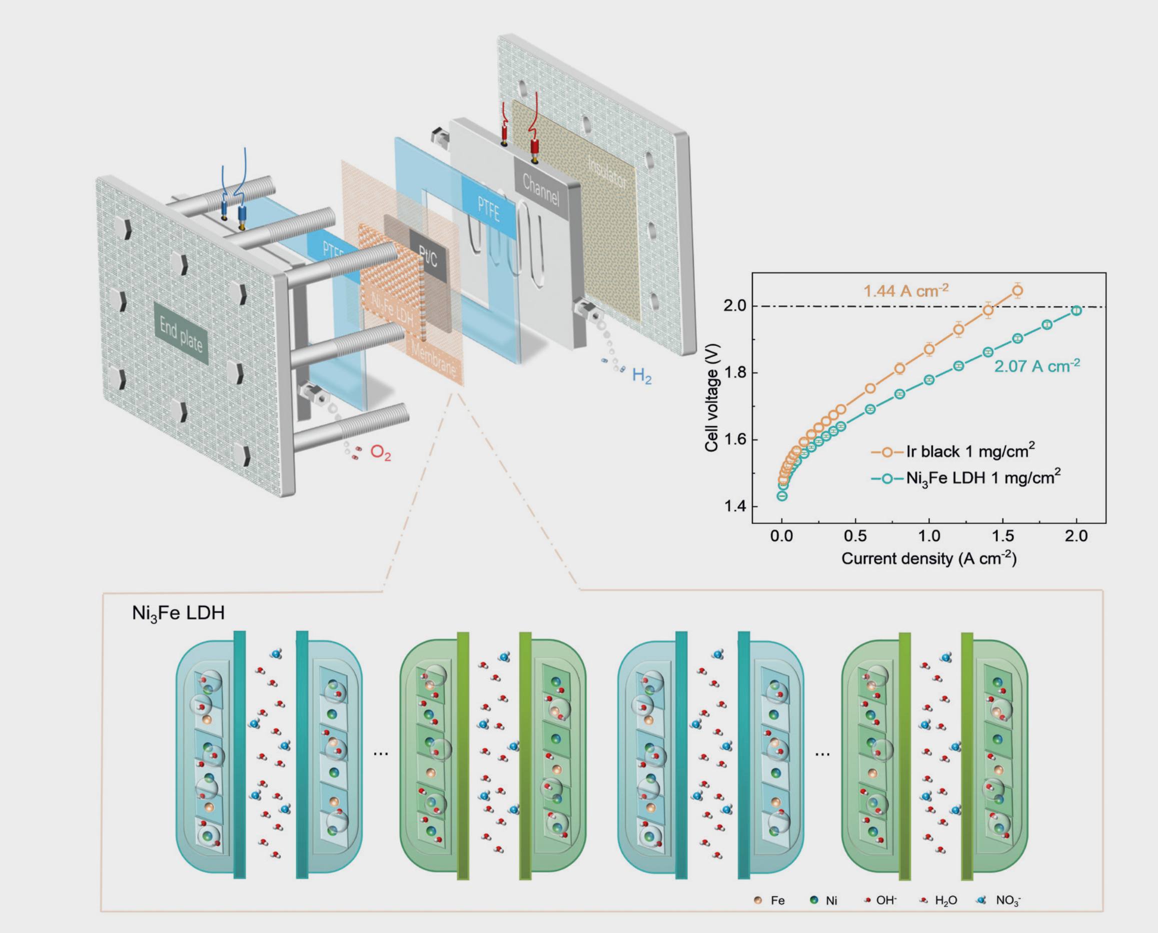

NiFe Layered Double Hydroxide Catalysts for Oxygen Evolution Reaction in Alkaline Water Electrolysis

Wulyu Jiang

Energie & Umwelt / Energy & Environment
Band / Volume 590
ISBN 978-3-95806-658-8

Mitglied der Helmholtz-Gemeinschaft

JÜLICH
Forschungszentrum

Schriften des Forschungszentrums Jülich
Reihe Energie & Umwelt / Energy & Environment Band / Volume 590

Forschungszentrum Jülich GmbH
Institut für Energie- und Klimaforschung
Elektrochemische Verfahrenstechnik (IEK-14)

NiFe Layered Double Hydroxide Catalysts for Oxygen Evolution Reaction in Alkaline Water Electrolysis

Wulyu Jiang

Schriften des Forschungszentrums Jülich
Reihe Energie & Umwelt / Energy & Environment Band / Volume 590

ISSN 1866-1793 ISBN 978-3-95806-658-8

Bibliografische Information der Deutschen Nationalbibliothek.
Die Deutsche Nationalbibliothek verzeichnet diese Publikation in der
Deutschen Nationalbibliografie; detaillierte Bibliografische Daten
sind im Internet über http://dnb.d-nb.de abrufbar.

Herausgeber und Vertrieb: Forschungszentrum Jülich GmbH
Zentralbibliothek, Verlag
52425 Jülich
Tel.: +49 2461 61-5368
Fax: +49 2461 61-6103
zb-publikation@fz-juelich.de
www.fz-juelich.de/zb

Umschlaggestaltung: Grafische Medien, Forschungszentrum Jülich GmbH

Druck: Grafische Medien, Forschungszentrum Jülich GmbH

Schriften des Forschungszentrums Jülich
Reihe Energie & Umwelt / Energy & Environment, Band / Volume 590

D 82 (Diss. RWTH Aachen University, 2022)

ISSN 1866-1793
ISBN 978-3-95806-658-8

Abstract

Efficient and durable oxygen evolution reaction (OER) catalysts for alkaline water electrolysis are highly required for future energy storage and energy conversion devices. However, objective evaluation and fair comparison of different catalysts remain a challenge due to differences in OER measurements. The evaluation criteria and the test protocol for the OER were investigated to compare the activity and stability of the electrocatalysts in the rotating disk electrode, and a standardized testing protocol was determined.

In the past decades, significant progress has been made in improving the activity and durability of catalysts by developing new materials. In particular, NiFe layered double hydroxides (LDH) electrocatalysts have been developed. Here, we synthesized NiFe LDH with tunable Ni/Fe composition, which exhibits corresponding dependent morphology, layer structure, and chemical states. The Ni_3Fe LDH, resulting from the optimized local chemical environment with more oxygen coordination and ordered atomic structure, exhibits superior OER activity than most reported NiFe LDHs on both half cell and single cell tests. In situ Raman spectra indicate the active species Ni(Fe)OOH at OER conditions and the dynamic phase transition during the cycling process.

Different strategies have been applied to further modulate the structure and improve the catalytical performance of NiFe LDHs. The introduction of formamide and permanganate ions into the interlayer could modify the layer structure and enhance the stability to some extent, while hydrothermal treatment can increase the crystallinity and form well defined nanocrystal of NiFe LDH and other NiFe-based catalysts.

Zusammenfassung

Effiziente und langlebige Katalysatoren für die Sauerstoffentwicklungsreaktion (OER) bei der alkalischen Wasserelektrolyse sind für zukünftige Energiespeicher- und Rückumwandlungstechnologien dringend erforderlich. Eine objektive Bewertung verschiedener Katalysatoren ist jedoch aufgrund der unterschiedlichen OER-Messmethoden nach wie vor eine Herausforderung. Die Bewertungskriterien und die Testprotokolle für die OER-Messungen wurden untersucht, um die Aktivität und Stabilität der Elektrokatalysatoren in der rotierenden Scheibenelektrode zu vergleichen. Hierauf basierend wurde ein standardisiertes Testprotokoll festgelegt.

In den letzten Jahrzehnten wurden durch die Entwicklung neuer Materialien erhebliche Fortschritte bei der Verbesserung der Aktivität und Haltbarkeit von Katalysatoren erzielt. Insbesondere wurden geschichtete NiFe Doppelhydroxid (LDH) Elektrokatalysatoren entwickelt. Im Rahmen der hier vorgestellten Arbeit wurden NiFe LDHs mit unterschiedlichen Ni/Fe-Zusammensetzung synthetisiert die verschiedene Morphologien, Schichtstrukturen und chemische Zustände aufweisen. Der Ni_3Fe LDH, der aus einer optimierten lokalen chemischen Umgebung mit mehr Sauerstoffkoordinationsstellen und einer geordneten atomaren Struktur resultiert, zeigt sowohl in Halbzellen- als auch in Einzelzellentests eine höhere OER-Aktivität als die meisten NiFe LDHs die aus der Literatur bekannt sind. In-situ-Raman-Spektren weisen auf die aktive Spezies Ni(Fe)OOH unter OER-Bedingungen und den dynamischen Phasenübergang während des Zyklusprozesses hin.

Abschließend wurden verschiedene Strategien angewandt, um die Struktur weiter zu modifizieren und die katalytische Leistung von NiFe LDHs zu verbessern. Die Einführung von Formamid im Lösungsmittel und Permanganat-Ionen in die Zwischenschicht konnte die Schichtstruktur verändern und die Stabilität in gewissem Maße verbessern, während eine hydrothermale Behandlung die Kristallinität erhöhen und gut definierte Nanokristalle von NiFe LDH und anderen Katalysatoren auf NiFe-Basis bilden.

Contents

Chapter 1 Introduction

1.1 Research background

1.1.1 Hydrogen economy

Due to the increased world's energy consumption over the last decades, the shortage of energy and awareness of environment protection have drawn more attention. Traditional fossil fuels (for instance, coal, oil, and natural gas), which are used as the primary source to meet the global energy requirements, however, are not endless and at the same time, promotes serious environmental pollution and greenhouse effect. Therefore, reduced or substituted fossil fuels lead to an urgent demand for the development of clean energy technologies. Owing to the progress of science and technology, several kinds of clean energy technologies have been developed and utilized. Among them, solar energy, hydro power, and wind energy can be converted into electricity, which is renewable and pollution-free, however, limited by its storage and transport process due to the splilled grid connection.

Thus, the development and application of efficient technologies to store and transport the clean excess electricity is necessary and meaningful. Meanwhile, electrochemical processes could act as a crucial role to convert the electricity to chemical energy, an indirect prerequisite for storage of renewable energy from solar and wind. In addition, water electrolysis is a promising technique to produce hydrogen for energy storage and transport. During the water electrolysis process, electricity from renewable sources could split water into hydrogen and oxygen. The produced green hydrogen can be either used directly in other fields as a chemical resource or stored and transported to other regions to produce electricity with zero emissions.

Utilizing and developing hydrogen as an intermediate energy carrier contains a few advantages, as shown in **Figure 1.1**. First, hydrogen is widely used in various industries, like chemical industry, aerospace industry, or more general in the transport sector. Second, hydrogen will not bring any extra emissions since its only product is water when converted back to electricity. Third, hydrogen possess high gravimetric energy density, with promising economic benefits.

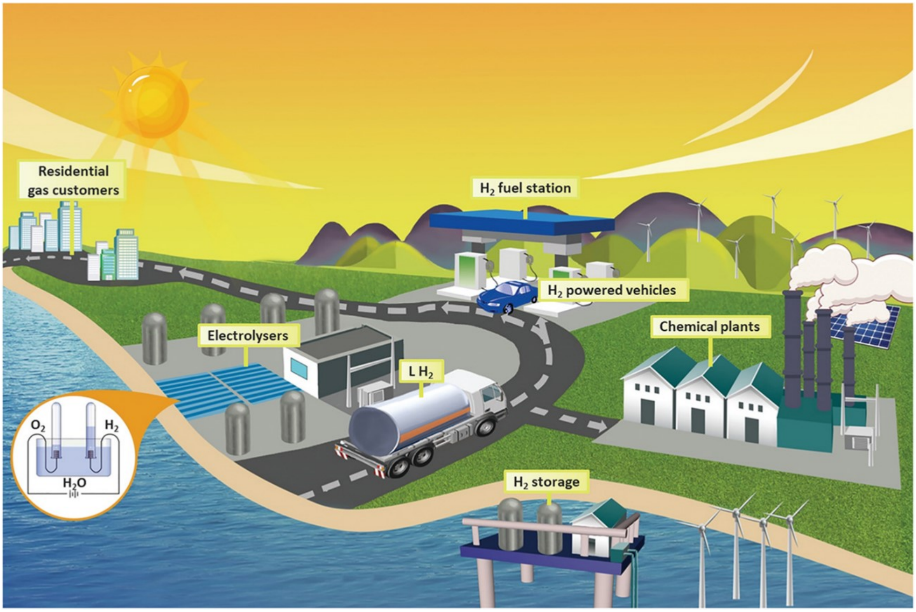

Figure 1.1 The production, storage, and usage of hydrogen.[1]

However, production of hydrogen also needs appropriate infrastructures with the consumption of extra energy. Therefore, highly efficient, and economic technique is very important to develop and apply hydrogen energy in a commercial scale. The employment of water electrolysis to generate hydrogen is the only mature technology currently. But the hydrogen amount via water electrolysis is very limited in today's hydrogen production market, due to economic consideration. The efficiency, cost and durability of water electrolysis needs to be improved for wider commercial applications.

1.1.2 Water electrolysis technology

In essence, water electrolysis consists of two half reactions, the hydrogen evolution reaction (HER) and oxygen evolution reaction (OER).

The overall chemical reaction formula of water electrolysis is:

$$2H_2O \rightarrow 2H_2\uparrow + O_2\uparrow \tag{1-1}$$

According to the applied electrolyte and the corresponding ionic agent (OH^-,H^+,O^{2-}), water electrolyzers could be classified into mainly three types: alkaline (e.g. anion exchange membrane, AEM which is a zero gap technology in contrast to classical diaphragm based alkaline electrolyzers), proton-exchange membrane (PEM) and solid oxide electrolyzers (SOE). The different reactions, basic principle temperature and electrodes of these three kinds of electrolyzers are illustrated in **Figure 1.2**.

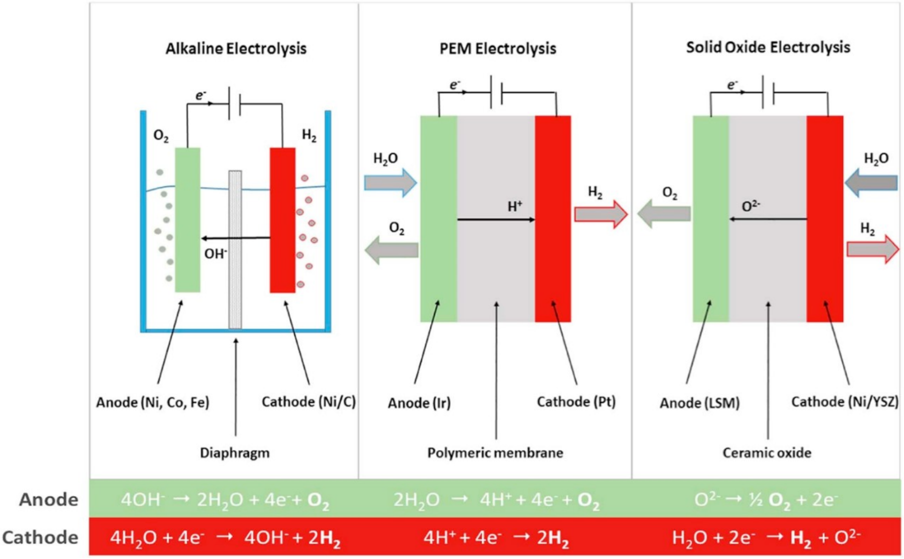

Figure 1.2 Illustration of three kinds of water electrolyzers, alkaline, PEM and SOE.[2]

When considering the commercial application of water electrolyzers, these metrics are usually emphasized: performance (activity and stability), and cost. Both parameters are mostly determined by the reaction pathways, electrodes, electrolyte (membrane) and temperature. For SOE, it exhibits the highest energy effciency, but works at the temperatures above 500 °C (up to 1000 °C) and utilize ceramic proton conductors，thus requiring higher expenses to build and operate and maintain it. In contrast, PEM and AEM work at relatively low temperatures, 20 - 80°C. At the acid condition in PEM, only noble metal or oxides, like IrO_2, RuO_2, could survive as anode catalysts, which limits its large-scale application due to the shortage stock and high price of noble metals. While AEM, whose anode and cathode electrodes are mostly immersed in an alkaline electrolyte, allow the application of non-precious catalysts, as a stable and mature technology. However, the slow dynamics and effciency are still the challenges for AEM, which need further attention and solution to solve them for commercial application.

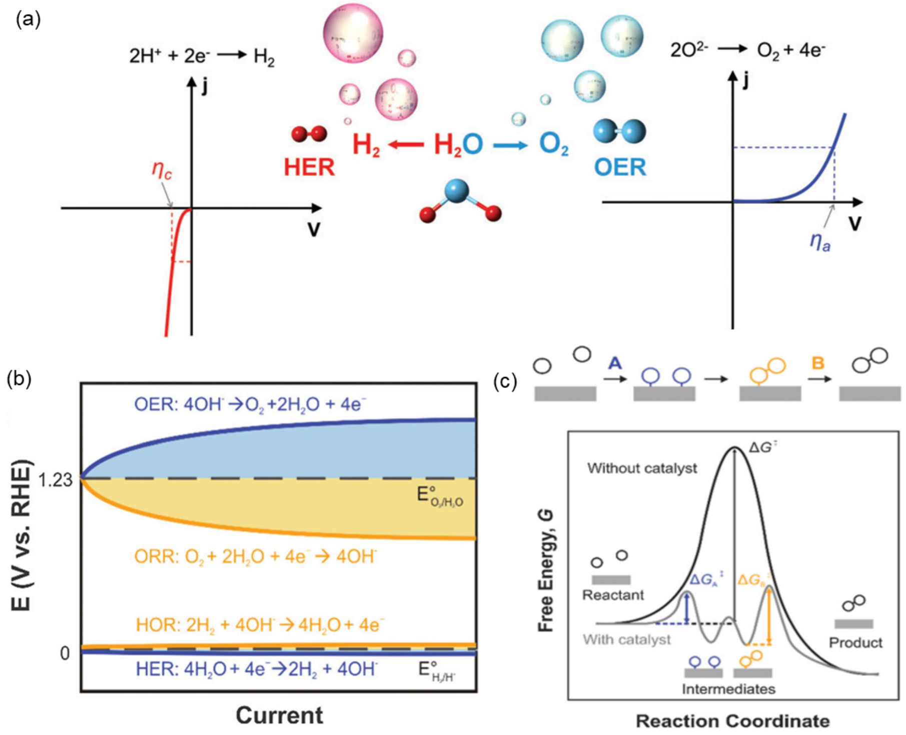

Figure 1.3 (a) polarization curves of the two half reactions of water electrolysis: OER and HER process.[3] (b) schematic diagram of the overpotentials of four half reactions.[4] (c) illustration of the reaction barrier, pathway with and without catalyst.[4]

Back to the reaction itself, it is well known that water electrolysis is a relatively slow kinetic process, especially the OER process at the anodes. The equilibrium potential of the overall four electron-proton coupled reaction is 1.23 V, but in practice, it requires an additional potential to overcome the energy barrier and trigger this reaction (named overpotential) (**Figure 1.3**). Therefore, it is necessary to utilize catalysts to facilitate reaction kinetics by providing an alternative pathway to lower activation energy. Detailed information about thermodynamics and kinetics in regard to electrolysis can be found in previous reviews.[4–6]

1.2 Progress of nickel based OER catalysts

Ni-based electrocatalysts have been extensively investigated for the OER in basic media due to their affordable prices, tunable structures, and promising properties. The effective strategies to fabricate highly efficient OER electrocatalysts are controlling the morphology, regulating the composition, tuning the electronic structure, and integrating hybrid structures into composites. So the reported efficient catalysts are not only pure nickel or oxides, but also mostly mixed metal and nonmetal compounds, like transition metal oxides and chalcogenides. These catalysts includ multiple crystal structures, such as various metal oxides belonging to perovskite, spinel and layer-structure families, as well as advanced designed nanostructures, for instance, shaped control, core−shell design and supported compounds. Part of the progress has been summarized in former reviews,[7–9] but particular advances are required for the Ni-based materials catalyzing the OER at the anode side. This part aims to summarize recent advances in the past five years of Ni-based electrocatalysts in oxygen evolution in alkaline media, to provide a new perspective on material design for OER catalysis.

1.2.1 Ni metal and Ni oxides

For the single nickel oxide electrocatalysts, their OER activities mainly depend on metal types, metal oxidation states, morphologies, and surface areas without the interference of other metal elements. For example, tuning the amount of precursor and reaction temperature leads to the shape-controlled synthesis of nickel nanoparticles and dependent OER activities[10] (**Figure 1.4**a, b). Two strategies are developed to address the limited surface area of nanoparticles. One is the three-dimensional design: Tingting Sun et al. enhance the OER activity of nickel nanocrystals by constructing ordered mesoporous nickel sphere arrays[11] (**Figure 1.4**c). The designed structure leads to an increase in the surface area, accelerated mass and charge transport, leading to superior OER activity than common nickel nanoparticles and RuO_2. The other idea is to reduce the particle size to increase electrocatalytically active sites, as such, the prepared ultrasmall (2.5-5 nm) NiO nanoparticles outperforms other nanocrystals with bigger sizes.[12]

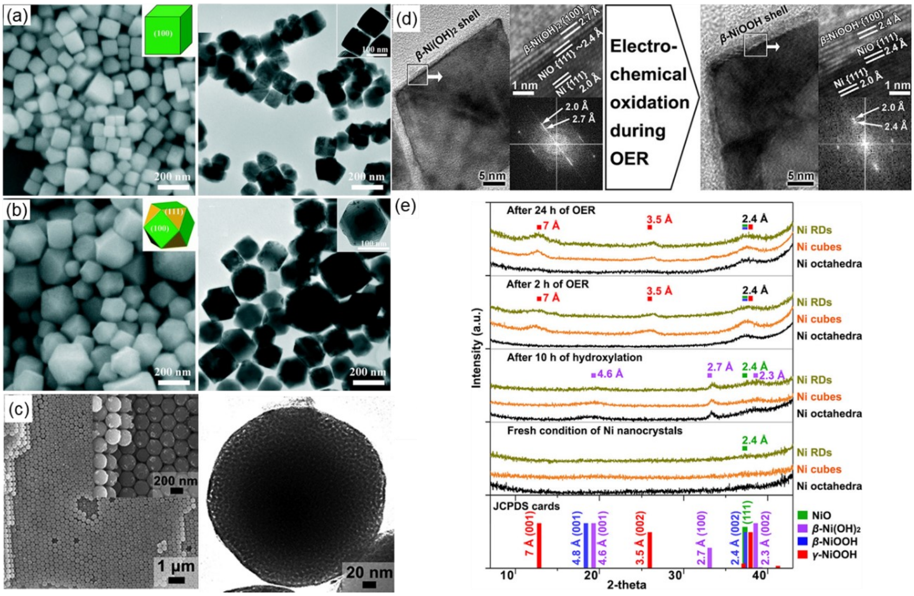

Figure 1.4 Ni nanocrystal electrocatalysts. (a,b) SEM and TEM image of (a) Ni nanocubes and (b) Ni cuboctahedra.[10] (c) SEM image of 3D ordered mesoporous Ni sphere arrays and TEM image of one of the mesoporous Ni spheres.[11] (d,e) Structural analyses of heteroepitaxial β-$Ni(OH)_2$ and β-NiOOH phases on Ni. (d) HRTEM images of the Ni octahedron after hydroxylation and after OER stability for 2 h. (e) Magnified XRD spectra of the Ni nanocrystals with different shapes under different conditions.[13]

As known from previous work, the dynamic phase transition of nickel catalysts can significantly affect their catalytic performance. The Bode cycle illustrates the Ni^{+2}/Ni^{+3} redox transition in hydroxide layer, where the α-$Ni(OH)_2$ and γ-NiOOH phases are hydrated phases in which water is incorporated, while the β-$Ni(OH)_2$ and β-NiOOH phases are not hydrated.[14,15] However, the interlayer spacing between these phases changes significantly because such an intermediate structure could transform under certain conditions, β-NiOOH will transform into γ-NiOOH after the incorporation of metal ions, which presents a different OER performance.[15] Recent work demonstrates the selective transition for the shaped nickel nanoparticles: The surfaces of Ni cubes and rhombic dodecahedra will transition from β-NiOOH to γ-NiOOH phase, while the more active β-NiOOH could be retained on the surfaces of Ni octahedra and exhibits resistance to further oxidation to γ-NiOOH, confirmed by TEM observation and XRD analysis, as shown in **Figure 1.4**d-e.[13] This finding provides new insight into understanding the OER properties of shape-dependent catalysts.

1.2.2 Ni oxyhydroxide

Since oxide structures convert to oxyhydroxides during the OER process, the development of oxyhydroxide electrocatalysts for OER attracted much research attention. Early work found that the OER activity of 3d-M oxyhydroxide systems followed the order of Ni > Co > Fe > Mn.[16] The activity of Ni oxyhydroxides could be further improved by various methods, such as coupling with the conductive substrate and embedding other components.[17,18] Qun He *et al.* developed efficient α-$Ni(OH)_2$ electrocatalysts with tunable nickel vacancies and showed that the increasing concentrations of nickel vacancies could improve the intrinsic conductivities of the catalysts, enhancing the formation of active species to promote electrochemical oxidation processes (**Figure 1.5**a).[19]

In addition, doping with other transition metals is a common strategy as reported in previous works, the effects of incorporating Ti, Mn, La, and Ce cations on the OER activity of $Ni_{1-z}M_zO_xH_y$ (**Figure 1.5**b).[20–22] Among them, the valuable role of iron should be highlighted, which exhibits significantly enhanced activity of mixed NiFe oxyhydroxides than the intentional and incidental iron incorporation.[23–25] These results lead to an increasing focus on the development of highly efficient NiFe-based oxyhydroxide catalysts, as summarized in previous reviews.[15,26,27]

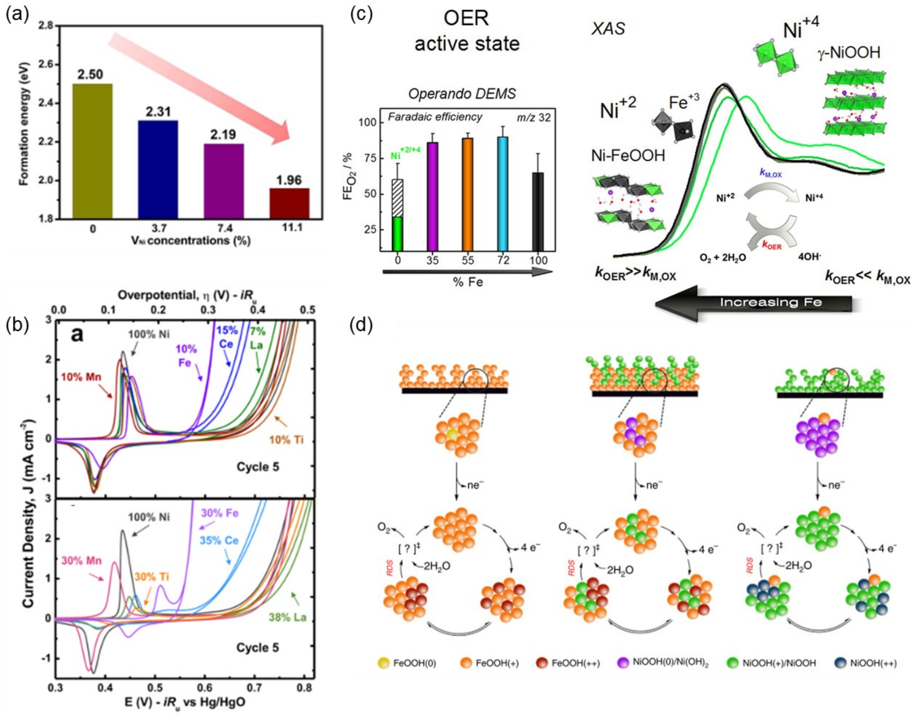

Figure 1.5 Ni-based oxyhydroxides. (a) The calculated formation energies for γ-NiOOH from α-$Ni(OH)_2$ with different V_{Ni} concentrations.[19] (b) Voltammetry $Ni_{1-z}M_zO_xH_y$ films, where M is a metal cation, at approximately upper $z \approx 0.1$ and lower $z \approx 0.3$.[56] (c) The role of Fe in mixed NiFe catalysts. The presence of Fe could promote a stabilization of low-valent Ni centers, and enhance the OER rate k_{OER}, which may exceed the rate of the metal oxidation k_{Mox}.[28] (d) schematic representations of the water oxidation process based on the experimental observations herein for FeOOH.[29]

However, the continuous discussion on the role of Ni/Fe and the actual active site is still ongoing due to the structure of oxyhydroxide.[15,30–35] The mixed metal nickel and iron both happen to occupy the equivalent site of the oxygen octahedron, early characterization techniques can hardly provide reliable and meaningful evidence to support any hypothesis. In 2015, the Bell group found Fe^{3+} cations in γ-$Ni_{1-x}Fe_xOOH$ have significantly lower overpotential than Ni^{3+} cations in either γ-$Ni_{1-x}Fe_xOOH$ or γ-$NiOOH$ by DFT+U calculation, proving that the OER occurs on Fe sites.[31] Experimental evidence from operando differential electrochemical mass spectrometry (DEMS) and X-ray absorption spectroscopy (XAS) also highlighted the special role of Fe in mixed NiFe catalysts (**Figure 1.5**c).[28] Nancy Li *et al.* demonstrated that percent Fe^{3+} doping promotes Ni^{4+} formation and correlates directly with increased catalyst activity in promoting OER.[34] This concept is consistent with the DFT work of Xueli Zheng et al. which emphasizes that the formation energy of the desired Ni^{4+} sites is systematically modulated by incorporating appropriate combinations of Co, Fe, and nonmetallic P resulting in the NiCoFeP oxyhydroxide catalyst performing better than IrO_2.[36] These seemingly contradictory conclusions could be reconciled by recent work on a series of Ni/Fe oxyhydroxide films, which showed that the atomic nature of the states of NiFe oxyhydroxides is related to the different elemental ratio of Ni: Fe and the environment of Fe in the NiOOH host matrix.[29] These internal different species could affect the catalytic kinetics with different active sites, namely Ni centers for Ni(Fe) OOH with incorporated Fe in small amounts, but Fe-centered oxidized states for FeOOHNiOOH with/and more Fe in isolated FeOOH islands (**Figure 1.5**d).[29]

1.2.3 Perovskite structure

Perovskites have attracted increasing attention in recent years because of their excellent catalytic performance for water oxidation.[8,37–41] Sabatier's principle suggested that suitable adsorption energy of Ni-based perovskite has potentially considerable activities towards OER. The general atomic model of Ni-based perovskite using $BaNiO_3$ as an example is shown in **Figure 1.6**a. The transition metal nickel is located in the oxygen-coordinated octahedra and is considered to be the active site, while the alkali metal sites are not OER active.[42] The corresponding STEM images in **Figure 1.6**b show the actual arrangement of all metal atoms in $BaNiO_3$ perovskite along the [001] direction, with Ni atoms (dark) surrounded by six Ba atoms (light), which is consistent with the crystal model in **Figure 1.6**a.[42]

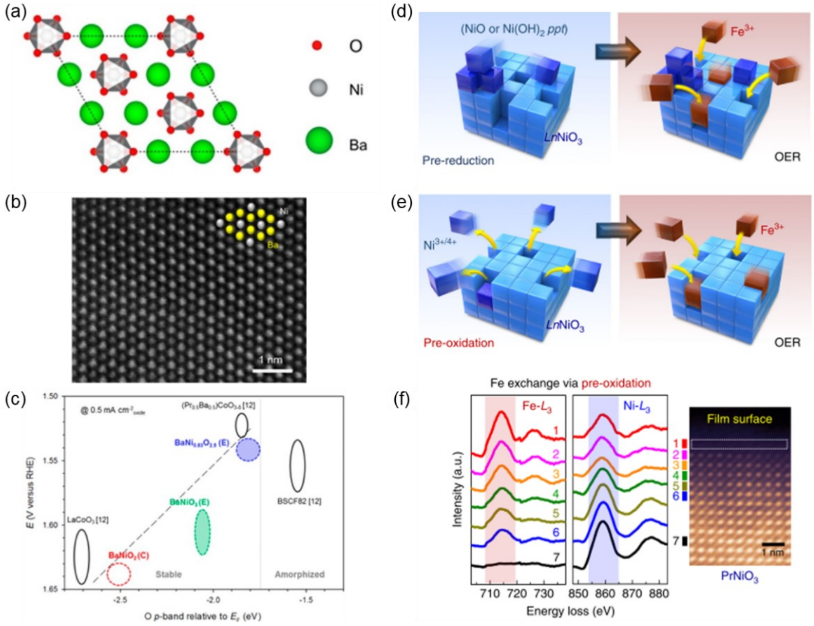

Figure 1.6 (a) Schematic of the $BaNiO_3$ crystal structure. (b) HADDF image of the $BaNiO_3$. (c) OER activity versus the O p band center relative to E_F (eV) of the $BaNiO_3$.[42] (d, e) Schematic illustrations surface Fe exchange by (d) pre-reduction and (e) pre-oxidation reactions in $LnNiO_3$ (Ln = La, Pr, Nd) perovskites. (f) A layer-by-layer EELS analysis of a $PrNiO_3$ film subject to the Fe exchange via pre-oxidation.[43]

Because of the unique active site, more researchers are trying to find the activity descriptor for perovskite catalysts to explain OER activity and guide the design of novel catalysts. Previous work discovered a volcanic relationship between the transition metal electron number and the OER activity.[39] This correlation was further optimized by considering metal-oxygen hybridization.[41,44]

Subsequently, further research has highlighted the relative energies of the transition metal 3d and oxygen 2p valence electron states in perovskites, termed the charge transfer energy. The energy difference could determine the catalytic mechanistic pathways, therefore, as the highlighting of O p-band center and d-band center in other work, are developed as a more universal descriptor for OER activity.[45–47] For example, the near-linear correlation between O p-band center and overpotential of $BaNiO_3$ with various defects and local electronic structure of Ni, as shown in **Figure 1.6**c, validates O p-band center as a good descriptor.[42]

Although there is no universal activity descriptor up to now, increased focus has been placed on the physical origin of the electronic structure and surface properties of perovskite oxides to improve their OER activities. Efficient strategies include tuning the electronic structure of transition metal and oxygen by varying their physical structure, applying lattice strain and introducing site defects we mentioned in $BaNiO_3$ system.[42,48] Moreover, a recent work reported a novel method to obtain a distorted oxygen octahedra $LnNiO_3$ (Ln = La, Pr, Nd) perovskite by Ni extraction during the pre-oxidation and pre-reduction steps (**Figure 1.6**d-e).[43] The electronic structure change of Ni at the surface area could be investigated by layer-by-layer EELS analysis (**Figure 1.6**f) with the substation by Fe, and DFT calculation further confirmed the significant variation in the O 2p and Ni/Fe 3d states, which enhance the charge transfer between metals and oxygen and the corresponding OER activity.[43]

1.2.4 Spinel structure

The spinel family is another group of promising OER catalysts. On the one hand, spinel usually exhibits moderate electrical conductivity and robust stability in the alkaline condition, which is well suited for OER. Moreover, in the spinel structure with the general formula AB2O4, in which A and B are metal ions in the oxygen-packed tetrahedra (T_d) and octahedra (O_h), illustrated in **Figure 1.7**a, the coexistence of two sites provides alternative accommodations for various transition-metal cations with specific valence states to form targeted catalysts.[49–52] The above features, therefore, make it possible to tailor the physical properties of spinel catalysts with different oxidation states and coordination environments, leading to fully tunable catalytic behavior and remarkable OER performance.[52–55]

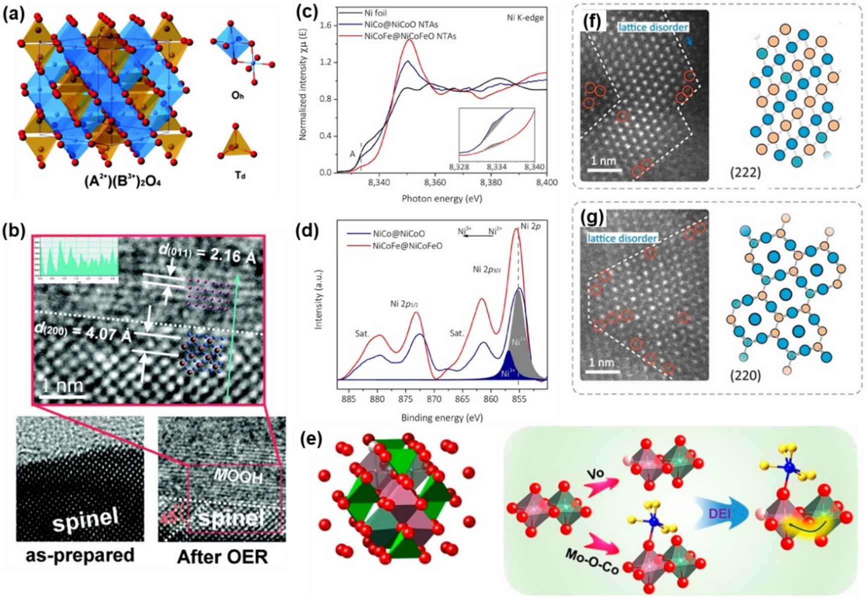

Figure 1.7 Ni-based spinel electrocatalysts. (a) Crystal structure of the spinel AB_2O_4 and corresponding octahedral sites (O_h) and tetrahedral sites (T_d). (b) HRTEM analysis of $NiFe_2O_4$ nanocubes before/after oxygen evolution reaction.[56] (c,d) XAS and XPS spectra of Ni in the incorporation of Fe into the binary Ni−Co inverse spinel NiCoFe@NiCoFeO.[104] (e) the creation of double-exchange interaction in spinel $NiCo_2O_4$.[52] (f,g) HAADF images of cycled $Zn_{0.4}Ni_{0.6}Co_2O_4$ nanoparticles.[55]

Most spinels for OER are Ni-based compounds, and the incorporation of other transition metals could effectively improve their OER performance, indicating the indispensable role of the effect of doped metals, while the most efficient spinel oxides for OER are NiFe-based spinels. As mentioned earlier, Ni-based oxide catalysts will form layered oxyhydroxides, which are also present in the NiFe spinel. TEM images in **Figure 1.7**b confirm the phase transition from the $NiFe_2O_4$ spinel to the spinel-derived metal oxyhydroxide MOOH, which dominates the electrocatalytic performance of the spinel structure.[56]

Optimizing the electronic structure of the active metal is another strategy to improve the OER performance of the spinel structure. However, a debate on the spinel active site is present, whether they are the cations in the T_d site or the O_h site. Tae Woo Kim *et al.* compared the activities of $ZnCo_2O_4$ with substituted Co by Zn in T_d site, and Co_3O_4 with both Co in T_d and O_h site, and their similar performances suggest Co in T_d site is not critical for OER.[57] Hsin-Yi Wang *et al.* reported the inconsistent OER activity of spinel with different site occupation: $ZnCo_2O_4$ showed significantly reduced activity due to the substitution of Co by Zn in the T_d site, while the activity of $CoAl_2O_4$ with octahedral Co replaced by Al is almost the same as that of Co_3O_4.[58] Further in situ XAS experiments also revealed that tetrahedral Co contributes to the formation of active structures and is ,therefore, the most important active site.[58] Guangping Wu *et al.* improved the OER activity by increasing the Fe content in the octahedral site in the $Co_{2-x}Fe_xO_4$ spinel and proved the dominant role of the octahedral site.[51] Similarly, in another $Ni_{1-y-z}Fe_yCr_zO_x$ system, the tetrahedral Fe can be reduced with increasing Cr content, leading to a continuous improvement in OER performance, suggesting that the Fe in the tetrahedral site may have a negative effect.[59] Therefore, it is generally believed that the transition metal in the octahedral site is the key to the catalytic activity, even if there are multiple sites in the spinel structure.

Based on this, recent work shows a similar volcano-shape trend between the e_g occupancy of the active cation in O_h with the OER activity for spinel,[53] which offers an overall view and guide to engineering spinels toward improved catalytic reactivity, for example, the modulation of site occupation. **Figure 1.7**c and d presented XAS and XPS spectra of Ni−Co spinel and NiCoFe@NiCoFeO by incorporating Fe into the T_d sites. The increased amount of Ni in O_h sites has been shown to increase the OER activity.[52] Another novel strategy to modulate the electronic configuration is the double-exchange interaction, as shown in **Figure 1.7**e. By constructing nano-heterojunctions and oxygen vacancies in

$NiCo_2O_4$ spinel, both octahedral coordinated Ni^{3+} and $Co^{(3-\delta)+}$ exhibit optimized binding energy with the intermediates and thus act as superior OER active sites.[60] A similar introduction of vacancy could also be achieved by leaching Zn from $Zn_{0.4}Ni_{0.6}Co_2O_4$ during cycling. HADD-STEM images in **Figure 1.7**f and g show abundant vacancies on the surface (marked by the red circles), which not only increase the active sites but also promote electron transfer for OER process.[55]

1.3 NiFe based LDH catalysts

1.3.1 OER activity of LDH catalysts

LDH is a special layer structure-type oxide, same as the mineral hydrotalcite. The compound could include nickel hydroxides incorporated with other cations, like Fe^{3+}, anion intercalation for charge compensation, together with water in the interlayer region, as illustrated in **Figure 1.8**a. Owing to its lamellar structure, LDH catalyst could expose more active sites towards electrolyte and present higher catalytical activity. **Figure 1.8**b and c compare a series of non-precious OER catalysts applied in half cell rotation disk electrode (RDE) and single cell water electrolyzer, NiFe LDH@DG10 catalyst is one of the best with the lower overpotential.[61]

Based on this, we further summarize the advanced Ni-based catalysts for OER in alkaline medium reported in recent decade, by comparing their activities in terms of the overvoltage required to reach 10 mA/cm^2 in **Figure 1.9** and **Table 1.1**. The overpotential of pure nickel material can reach up to ~400 mV while well-designed FeNi-LDH/FeNi catalyst with optimized structure exhibits favorable adsorption to the intermediates and finally enhances the OER process leading to a decreased overpotential at 130 mV even in 0.1 M KOH.[63] These results indicate LDH catalysts are promising for effective OER process.

In addition, the intrinsic activity of transition metal LDH were compared and the trend is found to be: NiFe LDH > CoFe LDH> CoCo LDH > NiCo LDH, CoMn

LDH > NiMn LDH (**Figure 1.8**d). The leading role in OER activity of NiFe LDH is due to the optimized OH-O scaling relationships from the dual-metals site feature of the reaction centers.[62] Therefore, the active NiFe-based LDH catalysts have attracted much attention with dedicated review about recent advancement in terms of NiFe oxyhydroxide/LDH.[15,30]

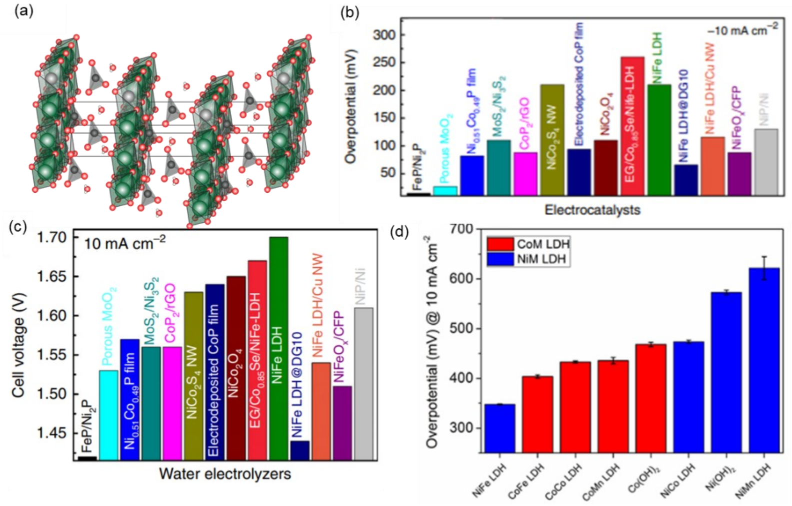

Figure 1.8 (a) Illustration of crystal structure of LDH. (b,c) comparison of various non-precious catalysts in half cell (RDE) and single cell (water electrolyzer) tests.[61] (d) Overpotential comparison at 10 mA/cm^2 of various Co- and Ni-based LDH catalysts.[62]

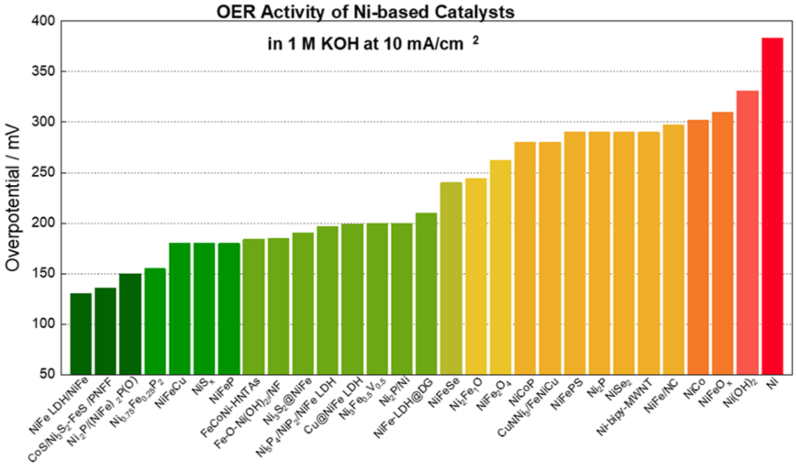

Figure 1.9 Benchmarking Ni-Based electrocatalysts for the oxygen evolution reaction by comparing the overpotential at 10 mA/cm^2 in 1M KOH. The details are given in Table 1.1.

Table 1.1 Comparison of the OER activities of different Ni-based catalysts

Catalysts	Shape/ Structure	Electrolyte@ KOH	Activity @10mA/cm^2 [mV]	Tafel slope [mV/decade]	Load [mg/cm^2]	Stability [h]	Refs
Ni	nanocube	1M	383	N/A	0.2	N/A	10
Ni	cuboctahedra	1M	402	N/A	0.2	N/A	10
Ni	3D sphere arrays	0.1M	254	39	0.2	10	11
NiO	nanoparticles	0.5M	300	N/A	0.02	N/A	12
Ni_2P	nanoparticle nanowire	1M	290, 330	59 47	0.14	10	64
Ni_2P/Ni	microsphere	1M	200	N/A	N/A	100	65
NiS_x	microsphere	1M	180	96	N/A	10	66
N-Ni_3S_2	3D network	1M	330/100	70	N/A	N/A	67
$NiSe_2$/Ni	3D nanowrinkles	1M	290	63	0.2	72	68
Cu-NiS_2	nanosheets	1M	232	46	0.2	60	69
$Ni(OH)_2$	hollow sphere	0.1M	331	42	0.2	N/A	70
Ni/$Ni(OH)_2$	nanosheets	1M	270	70	0.5	10	18
$NiFe_2O_4$	QDs	1M	262	37	0.21	100	71
Ni_2Fe_1O	nanowire	1M	244	39	0.15	60	72
Fe-O-$Ni(OH)_2$	nanosheets	1M	185	32	3	50	73
NiFeS/NF	vertical nanosheet	1M	65	119.4	N/A	N/A	74
$Ni_{0.75}Fe_{0.25}P_2$	porous nanosheet	1M	155	55	N/A	24	75
NiFeP	nanoplate arrays	1M	180	76	4.12	25	76
NiCoFeP	oxyhydroxides	$KHCO_3$	330	N/A	0.025	100	36
NiFePS	nanosheet	1M	≈290	56	0.5	50	77
NiFe/NC	nanoparticles	1M	330	45	0.2	20	78
NiFe/NC	nanoparticles	1M	297	48	0.5-0.6	20	79

NiFe LDH@DG	nanosheet@graphene	1M	210	52	0.283	10	17
Cu/NiFe LDH	3D core shell	1M	199	27.8	~2.2	48	80
Ni$_5$P$_4$/NiP$_2$/NiFe LDH	3D core shell	1M	197	46.6	2	24	81
Ni$_3$S$_2$@NiFe LDH	core shell	1M	190	10	N/A	40	82
NiFeSe	cubic nanocages	1M	240	24	0.1	22	83
Ni$_x$Fe$_{1-x}$Se$_2$	nanoplates	1M	195	28	4.1	24	84
NiCo/C	nanowires	1M	302	43.6	0.3	10	85
NiCoP	nanoplate	1M	280	87	1.6	24	86
NiCoP	hollow nanobricks	1M	270	76	2.0	20	87
NiCoP	nanoparticles	1M	310	52	0.75	N/A	88
NiFeCu	dendritic core shell	1M	180	33	1.6	20	89
NiFeSn/NiFe	nanospheres	1M	260	50	NA	~11	90
Ni-bipy-MWNT	CNT	1M NaOH	290	35	0.2	10	91
CuNNi$_3$/FeNiCu	porous core-shell	1M	280	52	0.367	24	92
NiCo@NiCoO$_2$/C	microrod arrays /core@shell NPs	1M	≈340	93.97	3.2	20	93
(Co$_{1-x}$Ni$_x$)(S$_{1-y}$P$_y$)$_2$/G	3D architecture	1M	285	105	N/A	100	94
CoS/Ni$_3$S-FeS/PNFF	3D architecture	1M	136	51	1.66	24	95
FeCoNi-HNTAs	hybrid nanotube arrays	1M	184	49.9	N/A	80	96

1.3.2 Progress of NiFe-based LDH catalysts

NiFe-based LDH catalysts exhibit promising catalytic performance with tunable structures and compositions. However, the number of active sites for raw LDHs is limited, the electron conductivity of NiFe LDH is usually quite poor, and the intrinsic activity with the electronic structure of active site of NiFe LDH could be further improved. Therefore, several kinds of strategies and promising approaches have been explored as follows:

(1) Hybrid with conductive substrates.

To improve the conductivity of LDHs, construction of hybrid LDH composites with conductive substrates, like various carbon supports or metal-based materials, is proved to reduce the charge and electron transfer resistances. Fabio Dionigi et. al [5] have summarized the NiFe LDH hybridized with carbon materials, as shown in **Figure 1.10**. For example, NiFe LDH nanoplates on three-dimensional electrochemically reduced graphene oxide (3D-ErGO) and NiFe-LDH nanoparticles on Co,N-codoped carbon nanoframes (Co,N-CNF) have both shown improved OER activity resulting from increased electrical conductivity.[97,98] But its effect not only contributes to the conductivity, the hybrid of NiFe LDH and single-walled carbon nanotubes (SWNT) exhibits strong interfacial electron coupling, leading to superior OER activity.[99] And the close coupling between NiFe LDH nanosheets and defective graphene discovers the synergetic effects of transition metal sites and carbon defects for OER catalysis.[17] In addition, integrated NiFe LDH/C hybridstructure exhibits excellent catalytical activity due to several aspects: (i) increased disorder from amorphous and distorted LDH structure, (ii) more active sites from enlarged surface area, and (iii) strong electron coupling between NiFe LDH and carbon.[100]

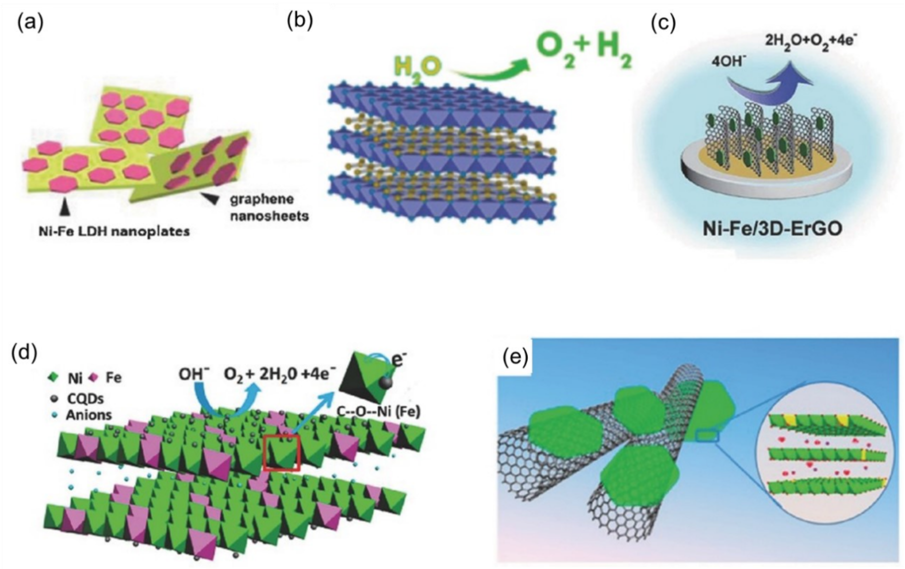

Figure 1.10 NiFe LDH hybridized with different nanocarbon materials. (a) NiFe LDH nanoplates on graphene, (b) NiFe LDH stacked with graphene, (c) NiFe LDH grown on 3D ErGO, (d) NiFe LDH with carbon quantum dots (CQDs), (d) NiFe LDH on carbon nanotubes.[15]

Besides of the carbon materials, other metal plates could also serve as supports. For instance, the introduction of NiO nanoplates into NiFe LDH nanosheet will lead to an intersection, which facilitates the adsorption of OER intermediates. [101] And the coupling of NiFe LDH/NiFe catalysts between the side surface of nanosheets and NiFe foil substrate boosts the electron and ion transfer process. Together with the synergistic enhanced adsorption of OH and the OER intermediates, a predominant OER performance appear for this NiFe LDH/NiFe catalyst.[63]

(2) Exfoliation of NiFe LDH

To increase surface area and active sites of LDH structure, numerous efforts have been devoted to get monolayers such as by exfoliation approach. As shown in **Figure 1.11**a, liquid phase exfoliation without changing the compositions of LDH could expose more active sites and increase the electronic conductivity. And the exfoliated monolayer LDH generally exhibits significantly improved OER activity than the corresponding bulk LDH. For instance, the exfoliated NiFe LDH exhibits remarkably decreased overpotentials at 10 mA/cm^2 by around 50 mV.[102] This method has also been successfully applied in other LDHs, like NiCo LDH.[103]

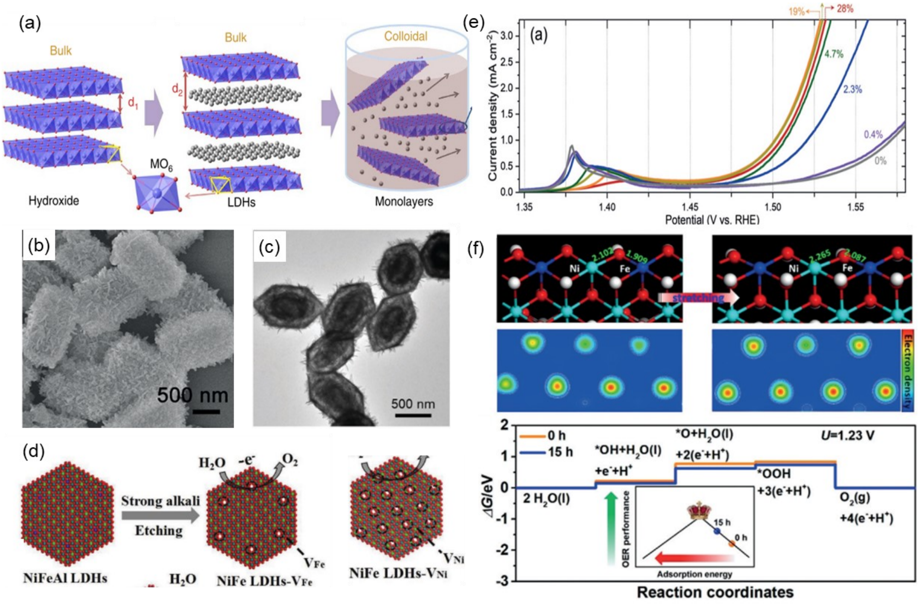

Figure 1.11 Summary of reported approaches to improve the OER activities of NiFe LDHs. (a) Illustration of exfoliation process to peel off bulk LDHs into monolayers.[102] (b,c) morphology design of NiFe LDH (b) hollow prisms[104] and (c) double-shelled nanocages.[105] (d) introduction of cation vacancies in NiFe LDHs.[106] (e) LSV curves of NiFe LDHs with various Ni/Fe ratio.[107] (f) The strain effect on OER performance of NiFe LDH.[108]

(3) Morphology design

Rational nanostructure engineering for NiFe LDH could increase the number of active sites and facilitate the mass/electrons transfer process, thus boost the OER activity. Xiong Wen (David) Lou's group has reported several kinds of NiFe LDH hollow structures (**Figure 1.11**b and c). For instance, NiFe LDH nanocages with tunable shells could enlarge its surface area and optimize elemental composition, so favorable for OER activity.[105] And the novel hierarchical hollow NiFe LDH nanoprisms consisting of ultrathin nanosheets only manifests large surface areas, thus leading to high performance towards OER.[104] The OER activity of NiFe LDH could be also optimized by reducing their large lateral platelets and increasing the availability of highly reactive edge and corner sites.[103] Monolayer NiFe LDH nanosheets with a size of 2.3 nm and a thickness of 0.6 nm formed by pulsed ultrasonication treatment of the metal precursors and yielded improved OER activity compared to monolayer LDH with a larger lateral size (around 30 nm).[109]

(4) Defect and vacancy

The introduced defects usually bring more exposed active site with unsaturated coordination number, such kind of local structure affects the absorption and desorption of OER intermediates, therefore presents distinct performance. The defects and vacancies common exist for monolayer LDH or ultrasmall LDH nanosheets. As reported, the porous monolayer NiFe LDH nanosheets with high density of oxygen and metal ion vacancies results in increased electropositivity and enhanced bonding strength of the OH*species.[110] While the ultrafine NiFe LDH nanosheets with abundant vacancies present semi-metallic character, and thus faster charge transfer and water electrolysis properties.[109]

Another strategy, leaching, is also applied to obtain Ni^{2+} or Fe^{3+} vacancies by leaching Al or Zn in two NiFe LDHs-V_{Fe} and NiFe LDHs-V_{Ni}, as shown in **Figure 1.11**c. These enriched iron or nickel vacancies could efficiently modulate the surface electronic structure and optimize the adsorption of reaction intermediates for OER.[106]

(5) Composition control

The control of Ni/Fe in NiFe LDHs is common to get the most active catalyst with optimized composition, however, the inside mechanism is hardly understood. Recently, a series of NiFe LDHs with different Fe contents proves the incorporation of Fe ions into NiOOH leads to structural disorder, which exhibits a volcano-type correlation with the activity of Fe sites (**Figure 1.11**e). This clarifies the origin of the Fe-dependent activity of NiFe LDH, and suggests structural ordering as a strategy to improve OER catalysts.[107]

(6) Elemental doping

Besides to modify the ratio of Ni/Fe, doping a third metal could also modulate the electronic structure of metal sites. The doped elements could be transition metals, for example, vanadium ions incorporated into the NiFe LDHs forming ternary NiFeV LDHs can narrow the bandgap reaching in enhanced electronic conductivity, facile charger transfer, and rich active sites.[111] The tuning of the local atomic structure of NiFe LDHs is also achieved by partially substituting Ni^{2+} with Fe^{2+} to form Fe-O-Fe motif, which will stabilize the high-valence metal sites for efficient OER process.[112]

In addition, doping noble metal could also optimize the electronic structure of NiFe LDHs. Single-atom Au decoration on NiFe LDH results in the charge redistribution of active Fe sites, as well as the NiFe oxyhydroxide close to the ideal catalyst with a 6-fold OER activity enhancement compared with initial NiFe LDH.[113] While for the noble metal which is OER active itself, as found in Rh/NiFeRh LDH catalysts, the role change from Fe to Rh ions as the major active sites accounting for OER catalysis.[114]

(7) Strain effect

The strain effect, caused by lattice mismatch, usually leads to a shifted d-band center, and alters binding energies toward adsorbate, which is widely used in precious metal catalysts.[115] Recently, tensile strain of NiFe LDH was generated by ball-milling process, leading to the electron-rich structure of Ni and Fe, and the enhanced binding strength of surface structure to active intermediates. Therefore, the ball-milled NiFe LDH exhibits reduced overpotential and higher intrinsic OER activity.[116]

1.4 Research motivation and goals

Although research over the last decades about NiFe LDHs has proved several advantages of such kind of catalyst: (1) abundant surface area due to the spatial lamellar structure and corresponding high surface to bulk ratio. (2) flexible structure with tunable ion doping and coupling. (3) controllable chemical composition of Ni/Fe. (4) excellent activity and comparable structure stability. (5) low cost due to the non-precious Ni/Fe and facile synthesis process.

However, there are still a few remaining challenges and unsolved questions to further boost the catalytical performance, understand the detailed structure, to find out the OER mechanism of NiFe LDH catalysts.

(1) Evaluation of catalytical performance. As the testing setup and protocols in different research groups are various, the reported catalytical performance of NiFe LDHs is not objective to be compared with other catalysts. The effects of each component of the experimental setup, process, and electrode preparation should be investigated and found out to allow a fair evaluation of the OER catalysts.

(2) Active site or species. Previous electrochemical measurements, in operando X-ray scattering, absorption spectroscopy, and density functional theory (DFT) calculations elucidate the catalytically active phase, reaction center and the OER mechanism of NiFe and CoFe LDH. Ni(/Co)Fe LDHs oxidize from as-prepared α-phases to activated γ-phases. The OER-active γ-phases are characterized by about 8% contraction of the lattice spacing and switching of the intercalated ions.[117] But a direct observation of morphology, atomic structural and the in-situ evolution process is not fully studied. More advanced in situ Raman, in situ XAS and environmental transmission electron microscopy (TEM) could help to observe and make clear this issue.

(3) Stability mechanism. As another important parameter for actual application, the stability of catalysts does not receive enough attention.

Although the evaluation of stability is also reported by potentiostatic curves or polarization curves during cycling process, there is a lack of deep investigation of the degradation mechanism. Recent work found the layered structure of bulk NiFe LDH is detrimental to OER stability. The interlayer basal plane in NiFe LDH is also OER active, while the narrow LDH interlayer spacing slows down the diffusion process into the interlayers, leading to a local acid condition and therefore metal dissolution of NiFe LDH catalyst. [118] However, whether this process occurs for all NiFe LDHs is not clear, and moreover, it could explain the degradation of monolayer LDH.

(4) Performance in water electrolyzer. Although numerous NiFe LDH-based materials have been synthesized, evaluated and reported as excellent OER catalysts in RDE, their actual single cell performance in water electrolyzers is still rarely addressed. Moreover, the development of AEM electrolyzers is limited by their efficiency and durability, especially for the cell using non-precious metal catalysts.[119–121] Several latest works reported improved AEM electrolyzer performance breakthroughs with non-noble-metal catalysts: the cell with NiFeCo as cathode and $NiFeO_x$ as anode reached 1 A/cm^2 at 1.90 V at 60 °C,[122] while an Fe-NiMo-NH_3/H_2||NiMo-NH_3/H_2 cell needed a voltage only at 1.57 V for 1 A/cm^2 at 80 °C.[123] The record efficient electrolyzer with nanometer-sized NiFe-LDH anode and Pt/C cathode, delivers 1 A/cm^2 low at 1.59 V at 80 °C.[124] However, these non-noble metal catalysts are obtained in a relatively complex synthesis process, either at high temperature (550 °C)[123], or long term (a few days) with the usage of several organic solvents.[124] These will limit its practical applicability considering the scaling production and economic costs of the catalysts. Therefore, a NiFe LDH, synthesized by facial method with large scale yield, and exhibiting comparable single cell performance, is crucial for the commercial application of AEM electrolyzers. Regarding the issue above, we plan to work on these aspects:

(1) Objective evaluation of the catalytical performance of NiFe LDH catalysts.

The difference of each component of the setup, the catalyst loading and substrate effect in the half cell measurements will be compared to determine a universal testing protocol for OER catalysts. Then the performance of synthesized Ni-based catalysts will be evaluated to benchmark as an excellent catalyst for water electrolyzer.

(2) Synthesis and electrochemical evaluation of NiFe LDH catalyst powders. The synthesis of large scale NiFe LDH powders are illustrated: it is conducted at room temperature, with a simple process, within a short time, and with no organic additive. Such kind of the production of the catalyst powders is low cost and repeatable, only then can it be extended to further large-scale applications. And the catalytical performance of NiFe LDH catalysts in both RDE and water electrolyzer will be evaluated.

(3) Investigation of the structure, including morphology, spatial size, crystallinity, chemical state, and local atom environment, of these NiFe LDHs and the corresponding correlation between the structure and catalytical performance. Surely some advanced in situ techniques will be adapted to investigate the active species or dynamic structure evolution during catalytic process. This will help to understand the optimal structure for OER and guide the improvement and design other catalysts.

(4) Further optimization of the structure and OER performance of the NiFe LDHs. Based on the understanding of NiFe LDH catalysts, several strategies will be adopted to modulate their structure and improve activity and stability towards OER process. Herein, we first discuss the experimental setup and protocols for half cell in Chapter 3, to provide some guidelines for OER measurements. Second, we introduce the synthesis, structure and catalytical performance of NiFe LDH in Chapter 4, as well as the discussion of its active intermediate and degradation mechanism. Then we adopted several methods to modulate the structure and catalytical performance of NiFe LDH in Chapter 5. And lastly, we

had a general discussion and summary of our work in Chapter 6 and 7.

Chapter 2 Experimental methods

2.1 Chemicals and material synthesis

Materials: All chemical reagents including $Ni(NO_3)_2$ (nickel (II) nitrate hexahydrate, ACS reagent, ≥98.5%, Sigma Aldrich), $Fe(NO_3)_3$ (ferric nitrate hexahydrate, ACS reagent, ≥98%, Sigma Aldrich) NaOH (sodium hydroxide, gradient grade, ≥99.9%, Honeywell) and KOH (potassium hydroxide, ACS reagent, ≥85.0%, Sigma Aldrich) have been used without further purification. Deionized water was used in all experiments.

Synthesis of NiFe LDHs: A co-precipitate method based on the low solubility product (K_{sp}) of metal ions (Ni^{2+} and Fe^{3+}) was used in an alkaline solution. 3 mmol of $Ni(NO_3)_2$ and 0.75 mmol of $Fe(NO_3)_3$ were mixed and poured into 50 mL of NaOH aqueous solution (0.15 M) under vigorous stirring (1000 rpm, 10 minutes at room temperature around 25 °C). After being thoroughly washed with DI water, the precipitates were re-dispersed in 25 mL DI water. The exfoliation was achieved by strong sonication on a Sonics Vibra-Cell (VCX 500) with a power of 400 W for 30 min. Finally, the sample was centrifuged at 4500 rpm for 5 minutes, cleaned with DI water and ethanol, and dried in a vacuum oven overnight at 25 °C. The resulting Ni_3Fe LDH was collected for further characterizations. To produce the remaining catalysts, the ratio of $Ni(NO_3)_2$:$Fe(NO_3)_3$ was changed to 2.5:1.25 to obtain the Ni_3Fe_2 LDH and to 1.875:1.875 to obtain the $NiFe_3$ LDH (the amounts in the ratios are given in mmol). For the bulk LDH samples, the exfolication process is removed without sonication treatment.

2.2 Electrochemical tests

2.2.1 Half cell measurements

Preparation of electrolyte. 1M KOH electrolyte was prepared by weighing 56 g KOH plates into 1 L distilled water, then calibrate the KOH concentration by the pH meter.

Purification of electrolyte. The purification treatment was conducted as reported to remove the impurity Fe ions inside the electrolyte:[23,24] Firstly, 2 g $Ni(NO_3)_2$ was dissolved in 4 mL DI water in a 50 mL polypropylene centrifuge tube (VWR), then 20 mL 1 M KOH was added to get green $Ni(OH)_2$ precipitate. Later the precipitate was centrifuged and washed three times using 20 mL DI water and 2 mL 1 M KOH. After the third washing step, the $Ni(OH)_2$ precipitate was used to purify KOH solutions. For purification, ~50 mL targeted electrolyte (here 1 M KOH) was added into the centrifuge tube with $Ni(OH)_2$ precipitate, and sonicated to make all precipitates fully dispersed. After resting at least three hours, the tube was centrifuged at 4500 rpm for 5 minutes and finally the upper purified 1M KOH was obtained and used for specific electrochemical tests.

Testing setup. As illustrated in **Figure 2.1**a, the electrocatalytic experiments were measured with electrochemical workstation (BioLogic Science Instruments, SP-150) and RDE setup (Pine Research Instrument) using a standard three-electrode cell designed to hold the glassy carbon (GC) electrode (Φ = 5 mm), a Pt mesh counter electrode, and a Hg/HgO reference electrode. Other alternative components are compared and discussed in the next chapter 3. Catalyst powders were prepared as inks by mixing 8 mg of catalyst in 1.5 ml isopropanol, 0.5 ml DI water, and 20 μL Nafion (5 wt %, Sigma Aldrich), and sonicated for 40 min. Then 10 μl catalyst ink was dropped cast on GC electrode and dried in air for 30 mins to get a flat catalyst film for testing. Catalyst loading on the GC surface was kept at 0.2 mg/cm^2. All the electrochemical measurements were conducted in Arsaturated 1 M KOH, 1M NaOH or purified 1M KOH electrolytes then purged with O_2 for 20 min before the OER experiments, with a rotation speed of 1600 rpm at room temperature (20±2 ˚C). The uncompensated series resistance (iR-drop) was determined by electrochemical impedance spectroscopy (EIS) in the frequency range between 0.1 Hz to 100 kHz at open circuit voltage.

Testing protocols. The different alternative options of testing protocols are compared and discussed in Chapter 3 later, and based on these results, a determined standard protocol to evaluate OER catalysts is used in chapter 4&5 of this thesis: an activation treatment was conducted before the LSV measurements by cycling the working electrode between 1.0 V and 1.7 V vs RHE (iR corrected) at a scan rate of 100 mV/s for 10 cycles based on our preliminary experimental conclusions. And the short-term reductive potential at -0.05 V was applied to remove the bubble at the electrode surface then the LSV polarization curves were recorded in a potential range of 1.0 to 1.7 V vs. RHE at a sweep rate of 5 mV/s without iR correction. The potential applied to the ohmic resistance was extracted later manually. In this work, the ohmic resistance (iR) drop at each electrolyte was compensated at 85% of the high-frequency resistance. The cycling stability was measured by LSV curves before and after 1000 cycles between 1.0 and 1.7 V with a scan rate of 100 mV/s in 1 M KOH. Long time chronoamperometry responses were measured at a fixed potential (1.6 V vs. RHE) for 20 hours or extended long term for instance 500 hours in 1 M KOH.

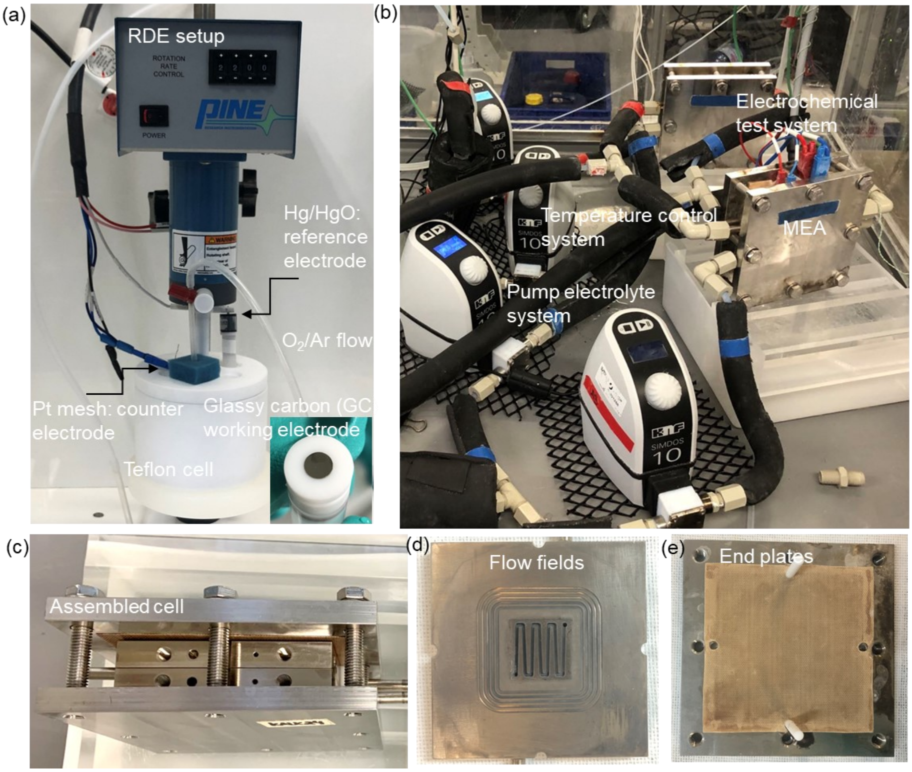

Figure 2.1 Experimental testing setup of (a) half cell RDE system and (b) single cell water electrolyzer system. (c) cross-sectional view of the assembled cell, (d) flow fields and (f) end plates.

2.2.2 Single cell measurements

Electrode fabrication of MEA. The MEA fabrication and single cell testing were conducted by my project partner Irina Galkina. For the MEA cell, the CCS electrode fabrication method was chosen. First, the ink formulation for both catalysts, Ni_3Fe LDH and Pt/C, was found to be optimal as follows: the catalyst powder and ionomer were dispersed for 5 minutes in a mixture of ethanol and water (1:1) with a rotating ultraturrax followed by 30 minutes of ultrasonic finger treatment. The catalyst ink was directly deposited on the clean porous transport layer (PTL)s: Toray carbon paper and Ni fiber PTL for cathode and anode side, respectively. The electrodes were prepared using an automatic spray coater (Exactacoat by SONO TEK), aiming for a catalyst loading of 1 or 2 mg/cm^2 and 20 wt-% ionomer content for the anode side, and a loading of 0.6 mg$_{Pt}$/cm^2 and 25 wt-% ionomer content for the cathode side. Before testing the cell, both anode and cathode were soaked in the 1 M KOH electrolyte as a pretreatment.

Electrochemical test of single cell. For the single cell tests, a potentiostatic/galvanostatic workstation (Biologic Science Instruments, BT-815, 15 A max., 10 kHz max.) was used for electrochemical measurements. A separate heating and temperature calibration system was attached to control the cell temperature. Four individual pumps were used to control the electrolyte flow in the system, as shown in **Figure 2.1**b. The measurements were performed in a 5 cm^2 cell hardware, with full nickel serpentine flow-fields on both sides. PTFE gasket were used to make the cell leak-tight: on the cathode, a 250 nm thick foil was used and a 400 nm thick foil was used on the anode side (photos of the main parts are shown in **Figure 2.1** c-e). The anode and cathode sides were fed separately with a 1 M KOH solution at flow rate of 50 mL/min. The cell temperature was adjusted to 55 °C according to common-used range 60-80 °C in reported works and the protocols in our institute. The cell was assembled in a cold state, using electrodes and membrane which were soaked for 3 h prior to assembly. Then the benchmarking of the single cell measurement protocol started with a cell conditioning step containing 2 h of electrolyte heating at open-circuit voltage (OCV) until a steady-state was reached. The break-in step was performed as a galvanostatic sweep with a scan rate of 10 mV/s between 1.4 – 2.1 V. The cell was further conditioned for 4 h at a constant current of 1 A/cm^2. The polarization curves were recorded four times by setting a constant current value for 1 min from 0.016 A/cm^2 and up to 2 A/cm^2, with a voltage limit set at 2.1 V. The last potential-current density curve was chosen as the one for evaluation, thus ensuring that, the cell was fully conditioned.

2.3 Physical characterizations

To fully understand our synthesized NiFe LDH and other samples, numerous characterization techniques were applied to determine the morphology and atomic and electronic structure of these catalysts. As summarized in **Figure 2.2**, besides of the ex-situ X-ray diffraction (XRD), scanning electron microscopy (SEM), infrared (IR) spectroscopy, Mössbauer spectroscopy and X-ray photoelectron spectroscopy (XPS), we also conducted in-situ Raman spectroscopy, XAS, and environmental TEM to track the dynamic structural evolution of NiFe LDH under OER process with the assistance from our collaborators

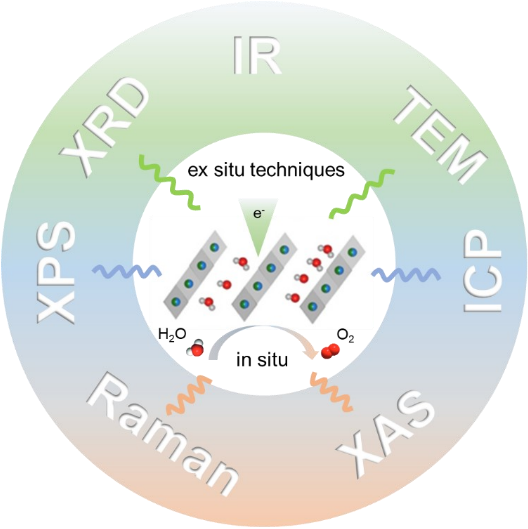

Figure 2.2 Summary of the characterization techniques for NiFe LDH electrocatalysts.

2.3.1 X-ray diffraction

XRD is a technique, which measures the intensities and angles of the X-rays scattered by the crystal atoms in the material. Therefore, XRD can help to identify the crystalline phase and crystallinity, determine the lattice parameter, orientation, grain size of the material. The crystal structure of our NiFe LDH materials was confirmed first by the XRD (D8 Discovery X-ray Diffractometer using Cu-Kα radiation (0.154 nm) in Bragg–Brentano geometry with a 2θ range from 5° to 70°. Measurement conditions are continuous scan mode during targeted range with step size 0.02°, step time 5 s at room temperature. X-ray generator is 40 kV and 40 mA, detector slit 9.5 mm.

2.3.2 Electron microscopy

The SEM collect the secondary electron and backscattered electrons converted by the lost energy from the electron beam interaction with specimen (**Figure 2.3**a). The corresponding images carry the information of surface topography and composition. For our samples, the SEM images and attached energy dispersive X-ray (EDX) element ratio were examined by Zeiss Gemini Ultra Plus instrument. The operation voltage is 200 kV.

TEM usually produces a high voltage electron beam to transmit through the specimen and creates a magnified electron image. Due to the flexible modes, TEM could provide multi structural information. High resolution TEM (HRTEM) images could observe the morphology and lattice fringes, while electron diffraction pattern in diffraction mode could work as the Fourier transfer object images, similar as local XRD pattern to some extent. The scanning transmission electron microscopy (STEM) use a focused spot to scan over the sample, and the alternative high angle annular dark field (HAADF) image reflects Z-contrast to distinguish the elements, more information like the composition distribution and chemical states could be obtained by the attached EDX and electron energy loss spectroscopy (EELS). TEM images of our samples were obtained using a FEI Titan, 80-300 TEM with a C_s corrector for the objective lens (CEOS GmbH).[125] The microscope was operated at 300 kV.

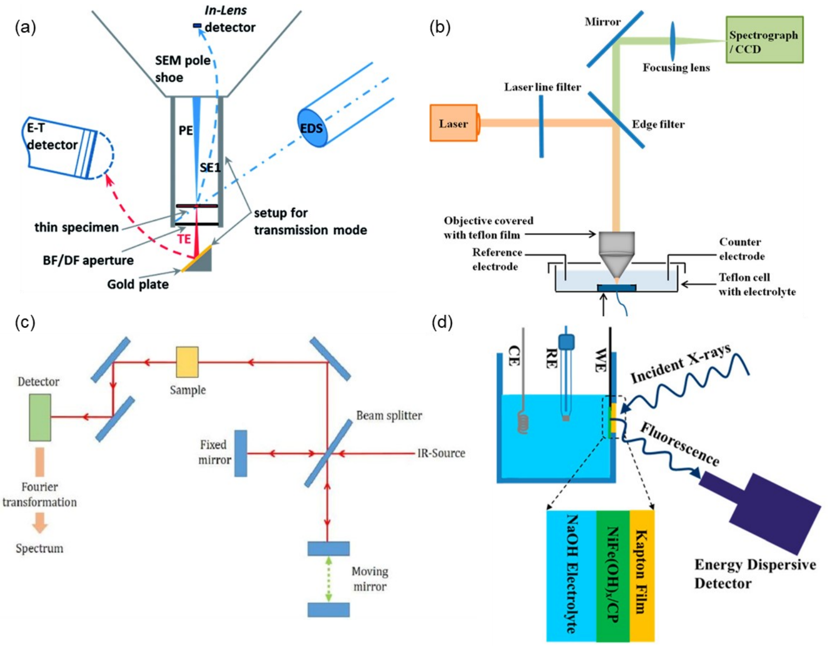

Figure 2.3 Illustration of various characterization techniques. (a) SEM and EDX system.[126] (b) Raman spectroscopy.[127] (c) FTIR spectrometer.[128] (d) In situ XAS setup scheme.[129]

2.3.3 Raman spectroscopy

Raman spectroscopy is based on the inelastic scattering of photons, known as Raman scattering, which provide the structural fingerprint to determine molecules. The Raman spectrum of powder samples (**Figure 2.3**b) was obtained at the laser wavelength of 532 nm, with power of 0.2 mW. The aperture is fixed at 50×1000 μm, and resolution is ~9-19 cm^{-1}, single spectrum is accumulated at an integration time of 2 seconds.

In-situ Raman Spectro-electrochemistry of NiFe LDH catalysts was carried out by our partner Dr. Alaa Faid and Prof. Svein Sunde in NTNU using WITec alpha300 R Confocal device equipped with a 532 nm laser (10 mW power). More details about the setup can be found in previous work.[130,131] The in-situ Raman measurements were performed in a Teflon cell with a quartz glass window. The

NiFe LDH catalyst ink was deposited on the GC electrode. The GC electrode (pine research), a Pt foil, and Hg/HgO (pine research) were used as a working, counter, and reference electrode, respectively. The Hg/HgO reference electrode was calibrated versus RHE in a three-electrode cell using two platinum electrodes (working and counter).[132] The Potential-dependent Raman spectra are acquired after holding at each potential in 1M KOH (semiconductor grade) for 5 min: initial sample, 1.3 V, 1.4 V, 1.5 V, 1,6 V, 1.7 V, 1.6 V, 1.5 V, 1.4 V, 1.3 V. The initial sample is the sample at an OCV The Raman spectrum acquisition was collected after 10 sweeps of 10 seconds from 100 to 1200 cm^{-1} and was calibrated using a 520.7 cm^{-1} silicon Raman peak.

2.3.4 Infrared spectroscopy

Infrared (IR) spectroscopy is to measure the interaction of infrared radiation with specimen by absorption, emission, or reflection (as shown in **Figure 2.3**c). The mid-infrared region, approximately 4,000–400 cm^{-1} is generally used to study the fundamental vibrations and rotational–vibrational structure. For NiFe LDH samples, attenuated total reflectance IR spectra of dry nanoparticulate powders were collected over the frequency range from 4000 to 400 cm^{-1} by averaging 32 scans with a resolution of 4 cm^{-1}.

2.3.5 Mössbauer spectroscopy

Mössbauer spectroscopy is a technique based on Mössbauer effect, from which minor variation in the nuclear environment of the atoms could be monitored. In our cases, it is conducted by Dr. Moulay Sougrati and Dr. Lorenzo Stievano from University of Montpellier, France. The absorbers were prepared using 50-60 mg/cm² of material. The ^{57}Fe Mössbauer spectra were measured at room temperature (293 K) with a $^{57}Co/Rh$ source and a Kr gas proportional counter. The spectrometer was operated with a triangular velocity waveform, and the spectra were fitted with superpositions of appropriate sets of the Lorentzian. The resulting parameters such as the electric quadrupole splitting Δ, the isomer shift δ (given relative to α-Fe), the linewidth Γ and the resonance area in percent of the total iron could be analyzed.

2.3.6 X-ray photoelectron spectroscopy

XPS, relying on the photoelectric effect, a surface-sensitive technique, can identify and quantify the elements on the surface of a sample, as well as their chemical states. When the sample surface is excited by a high-energy X-ray photon, the excited species will eject electrons and the emitted kinetic energy of the photoelectrons could be measured. XPS spectra were collected with a Phi5000 VersaProbe II from ULVAC-Phi Inc. with Al Kα as the monochromatic source (1.486 keV). The powder samples were pressed into an indium foil fixed with clamps on a sample holder. The survey spectra (**Figure 2.3**g) were obtained at 187.5 eV pass energy, 0.8 eV/step, 100 ms per step while the detailed core-level spectra were recorded with a pass energy of 23.5 eV, 0.1 eV per step. Charge-correction is conducted by setting the peak of C-C 1s to 285 eV.

2.3.7 Inductively coupled plasma

Inductively coupled plasma contains the inductively coupled plasma mass spectrometry (ICP-MS) and optical emission spectroscopy (ICP-OES) for element analysis. When plasma energy is supplied to the analytical sample from the outside, the sample atoms are excited. Then the excited atoms return to lower-energy positions, the emission rays are released and measured. The element type and content are determined based on the position and intensity of the photon ray. The iCAP 7600 was used for ICP-OES for powder samples, 2 aliquots of approximately 30 mg per sample were dissolved in 3 mL HCl + 1 mL HNO_3 at ambient temperature 25 °C for 0.5 h. Each digestion solution was made up to 50 mL, and 2 replicate dilutions of each digestion solution (100-fold dilution) were prepared and analyzed. ICP−MS: Agilent 7900 was used to measure the electrolytes. For the electrolytes (1M KOH) under different conditions, 20 mL were picked from the 200 mL total electrolytes after the stability test (1000 cycles between 1.0 – 1.7 V). Three replicate dilutions of each sample (100-fold dilution) were prepared and analyzed, then the averaged data with deviation were obtained.

2.3.8 X-ray absorption spectroscopy

XAS is a widespread technique used to characterize the local geometry and/or electronic structure of substances (as shown in **Figure 2.3**d). When the X-ray strikes an atom of the sample, the core electrons would either be excited to the unoccupied higher energy state (known as X-ray absorption near-edge structure, XANES) or the continuum state as extended X-ray absorption fine structure (EXAFS). The experiment testing detail was published in our previous work. All XAS experiments were conducted at the Fe K-edge (7112 eV) and the Ni K-edge (8333 eV) on the P65 beamline of the Deutsches Elektronen-Synchrotron (HASYLAB/DESY PETRA III, Hamburg, Germany) with the help from Dr. Bruna Ferreira Gomes Lobo and Prof. Christina Roth from University of Bayreuth [133]. Incoming photon flux energy was modulated with a Si(111) double crystal monochromator and the effective suppression of higher harmonics was achieved using Si-plane mirrors. The data were collected from -150 eV to +1000 eV (measured against the edge energy) with a scan energy increment of 0.55 eV in continuous mode. Spectra were collected in transmission mode, concomitantly with the spectrum of an Fe or Ni foil for energy calibration and alignment.

Three NiFe LDH samples, prepared in pellets to ensure an edge absorption of 1 unit, were analyzed using XAS. A total of 4 scans were measured and averaged per sample. Fe K-edge and Ni K-edge were measured for all samples and references ($Fe(NO_3)_3$ and $Ni(NO_3)_2$). Oxidation state information was obtained through XANES region analysis and structure geometry information (coordination number and bond distance) were determined through the fit of the

EXAFS. The measured spectra were processed (calibrated, averaged and normalized) using the Athena software and the EXAFS fits were made using the Artemis software.[134]

The XANES region from -20 to 100 eV relative to Fe-K and Ni-K edges was analyzed. The samples were compared with the spectra of the precursors: $Fe(NO_3)_3$ and $Ni(NO_3)_2$, respectively. The EXAFS spectra were normalized in the range of 150 to 850 eV in relation to the edge, using the Athena program.[134] The normalized spectra were then transferred to the Artemis program,[134] where the fitting was made. The appropriate scattering paths were generated with the atoms code (already present in the Artemis program).[135] The appropriate scattering paths were generated and extracted with the atoms code already embedded in the Artemis program. Only one single-scattering path was used for each edge, Fe-O and Ni-O first shell for Fe K-edge and Ni K-edge, respectively. The fitting was done in R-space (1 to 2 Å). For all fits, the Debye-Waller factor, σ^2, and E_0, which is a parameter used to align data energy with reference material energy, were calculated. The coordination number, CN, was determined using the “Amp” parameter in the Artemis program, according to the following equation:[136]

$$N = (\text{amp} \times N_{\text{theory}})/S_0^2$$

Where $S_0^2 = 1$ for Fe and Ni K-edges, N_{theory} (Fe-O and Ni-O) = 6.

A reasonable EXAFS fit takes into account many parameters and their accuracy (as well as correlations): the R-factor should be smaller than 0.02, ΔE_0 should not be too large (typical range ± 0 – 15 eV), S_0^2 was fixed at 1, as was previously done (typical range 0.7 – 1.05) and σ^2 (typical range 0.002 – 0.03 Å^2) cannot be negative,[134] with the number of independent points not larger than 2/3 of the total number of independent point as evaluated by the Nyquist criterion.[137]

Chapter 3 Electrochemical protocols and benchmark for OER catalysts

3.1 Background and motivation

The RDE method is the most common experimental technique for evaluating the electrochemical half-cell performance of electrocatalysts in a liquid electrolyte. This method evaluates the catalysts under simplified conditions to reveal the intrinsic properties and basic catalytic mechanism. So far, there is no perfect metric to represent the intrinsic activity of catalysts. The literature suggests a comparison of the polarization curve, Tafel slope, turnover frequency (TOF), and more, but some are unavailable or inaccurate. For example, it is almost impossible to obtain the exact number of active sites involved in the reaction to calculate the TOF. For nickel-based catalysts, it is economically permissible to increase the amount of catalyst loading to improve their activity but it does not seem fair enough to conclude that 2 mg/cm^2 catalyst A is more active than the 0.2 mg/cm^2 catalyst B. Besides, for the actual application of catalysts in alkaline water electrolyzers, increasing loading is not unlimited so it is not an essentially efficient method.

Moreover, each non-universal part of experimental testing could bring in extra electrochemical interference, inaccurate evaluation, and possible misinterpretation on catalyst performance. On account of this, some testing protocols for OER activity measurements based on theoretical analysis and empirical guidance have been recommended,[138] and designed experiments have also studied the influence of certain specific testing aspects, like electrolyte effect, cell material, etc.[139–141]

It is important that a systematic experimental investigation on the possible impacts of electrochemical testing setup and protocols on catalytic performance is still essential and worthwhile. Several issues related to the testing protocol should be addressed and solved, including the different test strategies, the alternative components of set up, for example, the effect of the counter electrode, the electrolyte, the selection of a cell material (e.g., glass cell instead of a Teflon cell), the impact of iron impurity as well as the catalyst loading and substrates while evaluating nickel-based catalysts to evaluate the activity, and stability of catalysts.

3.2 Test strategy for OER activity

A focus on each component of the half-cell setup was placed to evaluate and validate their effect on the performance and stability of the catalysts for OER. To ensure the uniformity and reliability of the experimental conclusion on catalysts with different structures, we chose a polycrystalline nickel electrode (Ni electrode), commercial nickel nanoparticles (Ni/NiO, 20 nm diameter with 2-5 nm oxide layer at the surface), and commercial nickel nanoparticles with 20% XC-72 carbon catalysts (Ni/NiO/C) to represent three basic catalyst systems. For Ni/NiO/C system, 20% carbon is enough to increase the conductivity **(Figure 3.1)** and minimize the possible impact from carbon on general performance, like carbon oxidation/corrosion under OER high potential conditions. To reduce the experimental contingency error, we carried out at least three repeated measurements for one experiment, the average curves presented with an error bar in the figures. All the possible effects from each electrochemical testing component are checked and compared by the changes of linear sweep voltammetry (LSV) curves using at least two alternatives. The possible effect of iR correction directly by potentiostatic adjustment or manual calculation was checked and shown in **Figure 3.2**, no difference between the two could be observed.

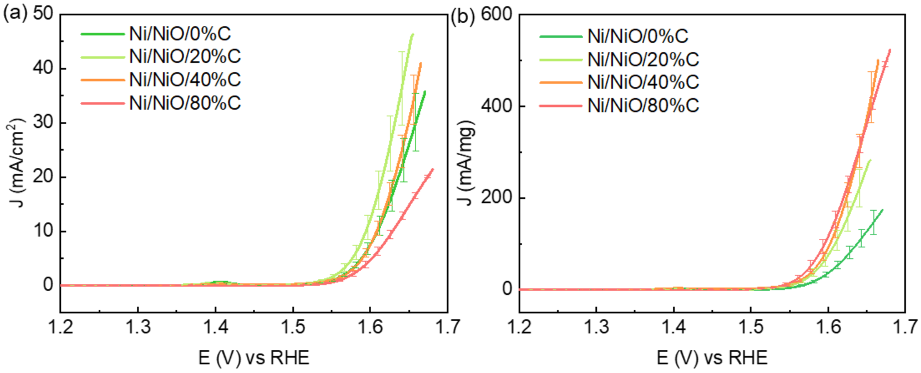

Figure 3.1 Comparison of Ni/NiO with various ratio carbon electrodes. Nominal activity normalized by geometry area (a) and mass activity normalized by rough mass of nickel (b) in Ni/NiO nanoparticles with 0, 20%, 40% and 80% mass ratio XC-72 carbon.

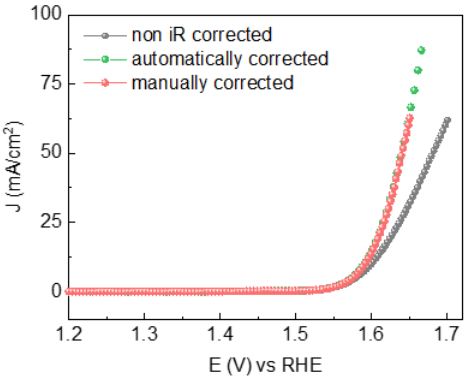

Figure 3.2 LSV curves of a Ni-based electrode in 1 M KOH without and with 85% iR drop compensation manually corrected or automatically corrected using the potentialstat.

As we know, there is a similar activation process for nearly all Ni-based catalysts to transform from the initial structure into active NiOOH intermediates under high potential.[27,117,142] This means a real activity of nickel-based catalyst will not achieve while performing only a LSV test directly. Therefore, several cycles before LSV were checked to activate the nickel electrode to generate a steady curve and a reliable evaluation of the activity. As shown in **Figure 3.3**a, the LSV curves after cyclic voltammetry (CV) treatment present improved activity compared with the direct LSV test of the nickel electrode, the inserted corresponding enlarged nickel redox peak confirmed its activation process. At the same time, ten cycles are enough to trigger the activation, and even more cycles (20 CV+LSV) will not increase the current further.

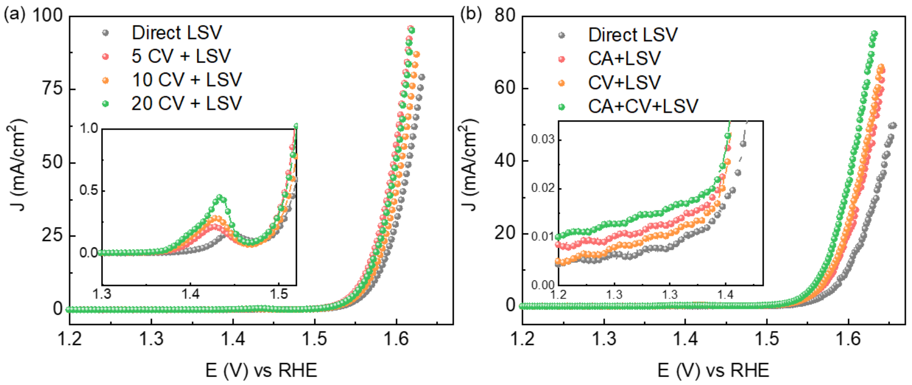

Figure 3.3 CV activation and reductive potential treatment of Ni electrode. (a) LSV curves after several cycles 0 (direct LSV), 5, 10 and 20 CV activation treatment (5, 10, 20 CV + LSV). (b) Comparison of direct LSV, LSV curves after reductive potential treatment at -0.05 V vs for 30 seconds (CA+LSV), LSV curve after 10 cycles CV activation (CV+LSV) and LSV curve after combining 10 cycles activation and reductive potential treatment at -0.05 V vs for 30 seconds (CA+CV+LSV).

Another fundamental concern toward RDE testing is the wettability of the electrode in the electrolyte. If the wettability is poor, most active sites of the catalysts will not contact the electrolyte and participate in the catalytic reaction, leading to a deceptive performance. Here, we adopted a constant reductive potential treatment before LSV tests by keeping the working electrode at -0.05 V for 30 s.[143] The LSV curves with the chronoamperometry (CA) process exhibit an increase in the capacitance and OER current compared with direct LSV curves, as presented in **Figure 3.3**b. This improved activity results from the reductive potential, the oxygen bubbles covering the surface could be consumed, leading to an improvement in wettability at the catalyst-electrolyte interface. The effect of CA treatment is also experimentally confirmed by the bubble disappearing, the reductive current at the CA process, and the more repeatable LSV curves (**Figure 3.4**). In summary, the testing protocol of OER activity suggested from our work is to start with a constant reductive potential treatment (-0.05 V for 30 seconds), followed by ten cycles of activation (10 CV), and then the LSV polarization curves.

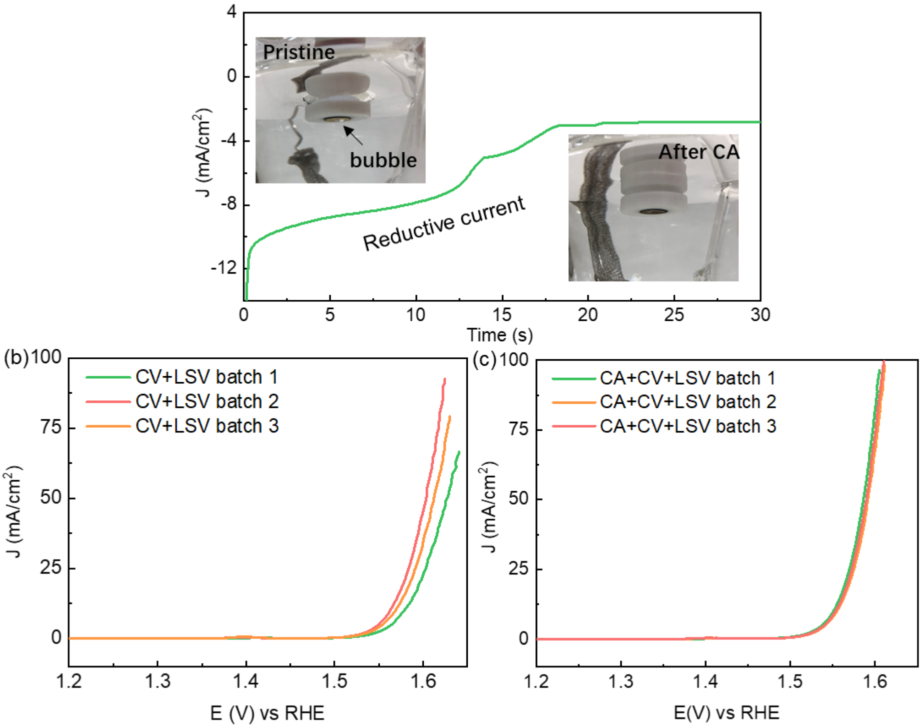

Figure 3.4 (a) the CA curve of Ni electrode at constant reductive potential -0.05 V for 30 seconds. Inserted pictures show the working electrode covered with bubbles at the beginning, and later the bubbles were consumed after the CA process. (b,c) LSV curves of independent three batches of Ni electrode without (b) and with (c) the CA process. Due to the different wettability, the three curves in (b) present some deviation, and the repeatability was improved after CA treatment in (c).

3.3 Test strategy for OER stability

Two model strategies, galvanostatic or potentiostatic measurements, are being used to evaluate the OER stability over time.[144] The cycling process (1000, 2000, 5000 cycles or more) is a typical protocol to compare the changes in CV curves.[11,72,76,78,91,93] While some reports prefer to record current curves at the constant potential for tens of hours (10, 20, 50 h, and so on), then the trend can be observed intuitively.[36,66,73,94,96]

However, one crucial factor, the continuously evolved oxygen at OER potential, will interfere with the exhibited CV or CA curves for stability evaluation. The dynamic process could be simplified and is illustrated in **Figure 3.5**a: When the test starts, the electrode observed as ideal wetted after reductive potential treatment (stage 1). Then the OER reaction is triggered, oxygen gas produces, aggregate, and gradually form bubbles at the surface of catalysts film even with high-speed rotation (stage 2). Later the bubbles grow in size when more oxygen gas assemble and converge (stage 3). As the pressure from electrolytes and centrifugal force due to the rotating increase, the electrode will remove the bubbles finally, bringing the electrode back to initial wetted status (stage 1). This cycle repeats itself in an irregular period.

Figure 3.5b shows the CA curve of the Ni electrode at 1.6 V over time, zigzag periodic variation confirms the dynamic cycle of bubble formation, accumulation, and elimination on the electrode for the stability tests. As the dynamic process is uncontrollable, the period is random and unpredictable, it is hard to select the right point to compare the performance before and after stability tests. For example, the current at the endpoint on CA curves may be obtained with unremoved bubbles at stage 3 compared with the current at stage 1, the value change of currents will underestimate the stability of the catalysts.

The effect of oxygen bubbles can also be observed on the continuous cycling process. As shown in **Figure 3.5**c, the overpotentials at 10 mA/cm^2 from different cycles present a periodic vibration, which will affect the accurate assessment of the stability. The CV curves at a fast scan rate for stability tests could not reflect the real performance directly due to the increased capacitance current and limited mass transfer.

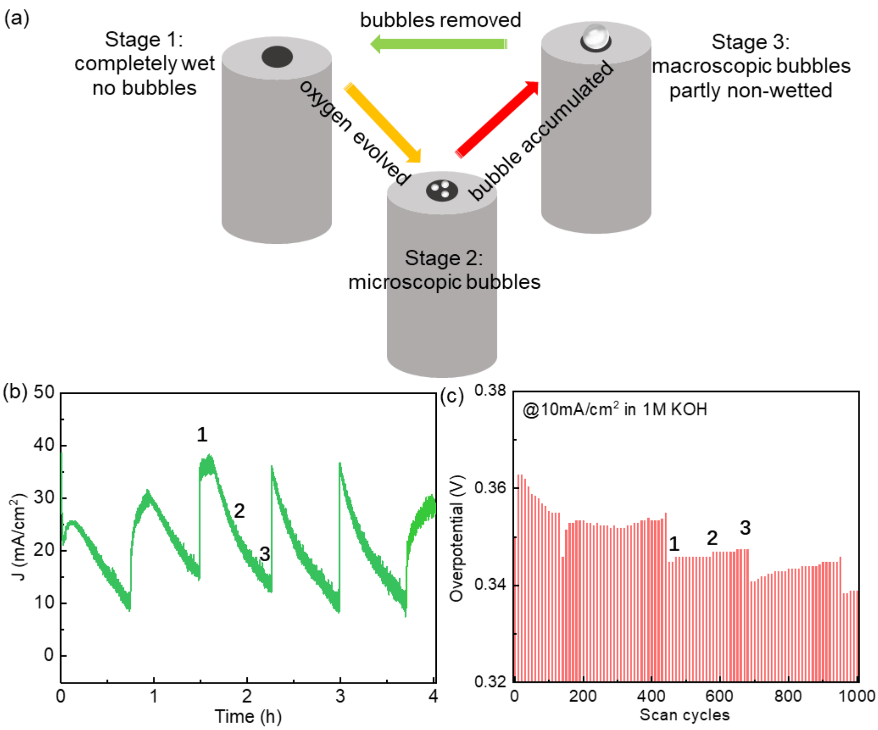

Figure 3.5 (a) illustration of dynamic cycling of bubble formation, accumulation, and elimination during stability tests, (b) CA curves of Ni electrode at 1.6 V over time, (c) overpotentials of CV curves from 1st to 1000th cycles.

Therefore, our protocol to evaluate OER stability is by two LSV curves before and after the long-time tests. The three stages of the electrode during the dynamic cycling or potentiostatic/galvanostatic periods are just an intermediate process with no effect on the final LSV tests when we applied constant reductive potential to remove all possible bubbles. As shown in **Figures 3.6**, although the direct CA/CV curves of Ni electrode from different batches show a significant difference, which may lead to an inaccurate evaluation of stability, the corresponding LSV curves before and after stability tests are still consistent. That confirms our protocol by comparing LSV curves, not direct CA or CV curves, could get a fair and reliable evaluation of OER stability.

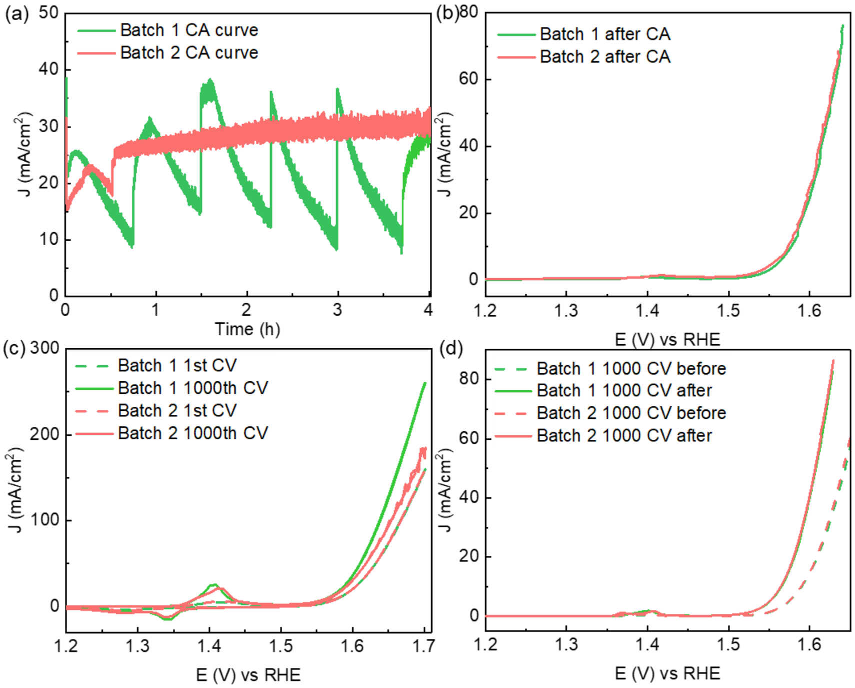

Figure 3.6 (a) CA curves of Ni electrode of two batches at 1.6 V for 4 hours and (b) the corresponding LSV curves after CA process. Although the CA curves show big difference, which may lead to inaccurate evaluation of stability, LSV curve present consistent trend, so these verify the advantage of taking LSV to compare stability, not direct CA curves. (c) 1st and 1000th CV curves of Ni electrode of two batches during the cycling between 1.0-1.7 V and (d) the corresponding LSV curves after these 1000 cycling process.

3.4 Test setup components

3.4.1 Counter electrode

In the literatures, Pt materials such as Pt wires, foils, or meshes are commonly used as the counter electrode, while few works would prefer carbon material, like graphite rod. But it is not clear which one is more proper for OER measurements. In this section, LSV measurements of Ni electrode, Ni/NiO and, Ni/NiO/C performed comparing the two counter electrodes Pt mesh and graphite rod, before and after 1000 cycles in 1 M KOH and presented in **Figure 3.7**a-d. The initial LSV curves of the Ni electrode tested with Pt mesh and graphite rod counter electrodes show no effect on the OER activity (**Figure 3.7**a). This result was consistent with the LSV curves of Ni/NiO and Ni/NiO/C.

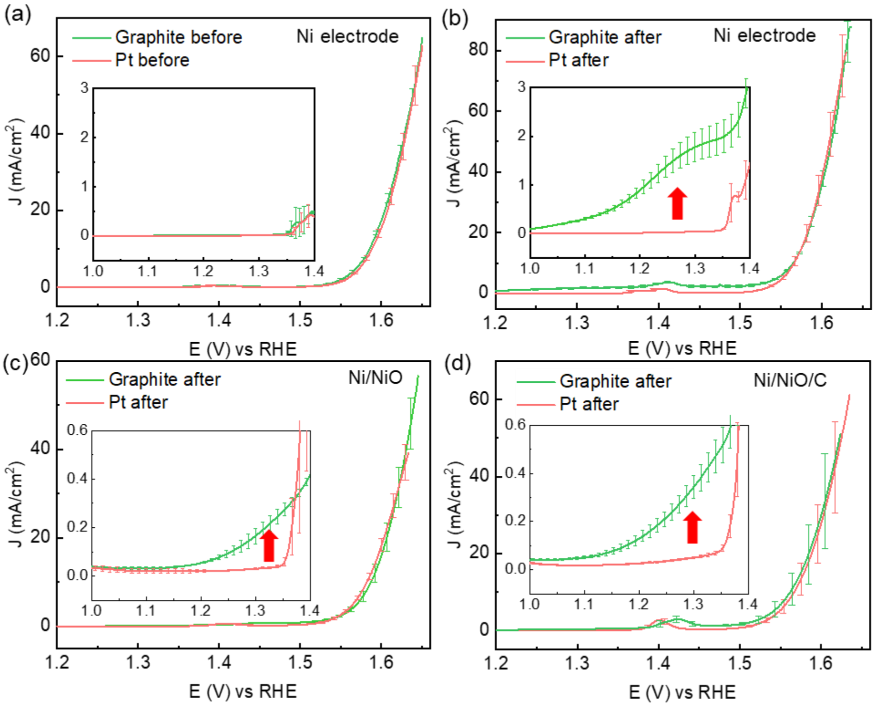

Figure 3.7 Polarization curves of (a,b) Ni electrode, (c) Ni/NiO and (d) Ni/NiO/C samples by two different counter electrodes before (a) and after (b-d)1000 cycling process, including: graphite rod (green) and Pt (red); inserted figures are the corresponding magnification area before nickel redox peak, the added red arrow is the indication of increased current at 1.0-1.4 V after cycling when using graphite as counter electrode.

However, for the stability test, the two LSV curves after 1000 cycles exhibit differences at the capacitance area from 1.1 V to 1.35 V before the nickel oxidation peak. The LSV curves are flat for Pt mesh, while an increase in the current exists for graphite rod (red arrow in **Figure 3.7**b). This effect attributed to the graphite rod, and more precisely, the oxidation of carbon. This increasing current of carbon corrosion also appeared in Ni/NiO and Ni/NiO/C, as shown in **Figures 3.7**c and d. Previous studies have shown carbons would steadily be oxidized and corroded under high potentials, and the extra oxidation would bring negative influences such as the accurate evaluation of catalyst stability.[145–147] Although the overall LSV curve and corresponding OER activity did not change significantly after 1000 cycles, the influence from the counter electrode could be accumulated at an extended time or enlarged at more severely oxidative conditions. Besides, the extra current will overlap with the capacitance current and nickel oxidation peak, then hinder the accurate analysis of capacitance for ECSA determination and charge transfer number during the nickel oxidation process. In contrast, Pt mesh is stable. The possible negligible Pt dissolution-redisposition will lead to a minor effect on the OER catalysts. Therefore, we recommend using Pt material as a counter electrode for the evaluation of alkaline OER catalysts, especially for long-time stability tests.

3.4.2 Electrochemical cell

Glass cell and Teflon cell are the two options of performing electrochemical tests. For alkaline electrolysis, the choice of cells is critical because the corrosion process of the glass material creates impurities that can influence the evaluation of the catalysts. The influence has been studied in other systems, for example, the negative effect of silicates leaching from glass components into the electrolyte on the process of the oxygen reduction reaction.[140] But in alkaline OER conditions, it is not yet clear whether it plays a role. Therefore, we compared the possible effect of Teflon and glass cell on OER activity and stability of Ni electrode, Ni/NiO, and Ni/NiO/C systems. As shown in **Figure 3.8**, the initial activity tested in these two cells shows no difference because the rate of glass corrosion is not fast. During the extension of the test time for 1000 cycles, two consistent LSV curves within the error range were observed for all three systems. This means that the cell material has no obvious influence on the OER performance during the 1000 cycles. One possible reason could be that the duration of 1000 cycles (~4 hours) is not yet long enough for a significant increase of impurities in the electrolyte, and another reason is that the leaching components, including silicates, boron, aluminum, or lead, are not active and do not participate in and influence this OER process. Nevertheless, to eliminate all possible effects from impurities, we recommend the use of Teflon cells for alkaline electrochemical measurements and to avoid the use of other glassy materials in the preparation and storage of alkaline electrolytes, such as the commonly used glass volumetric flasks and gas inlets.

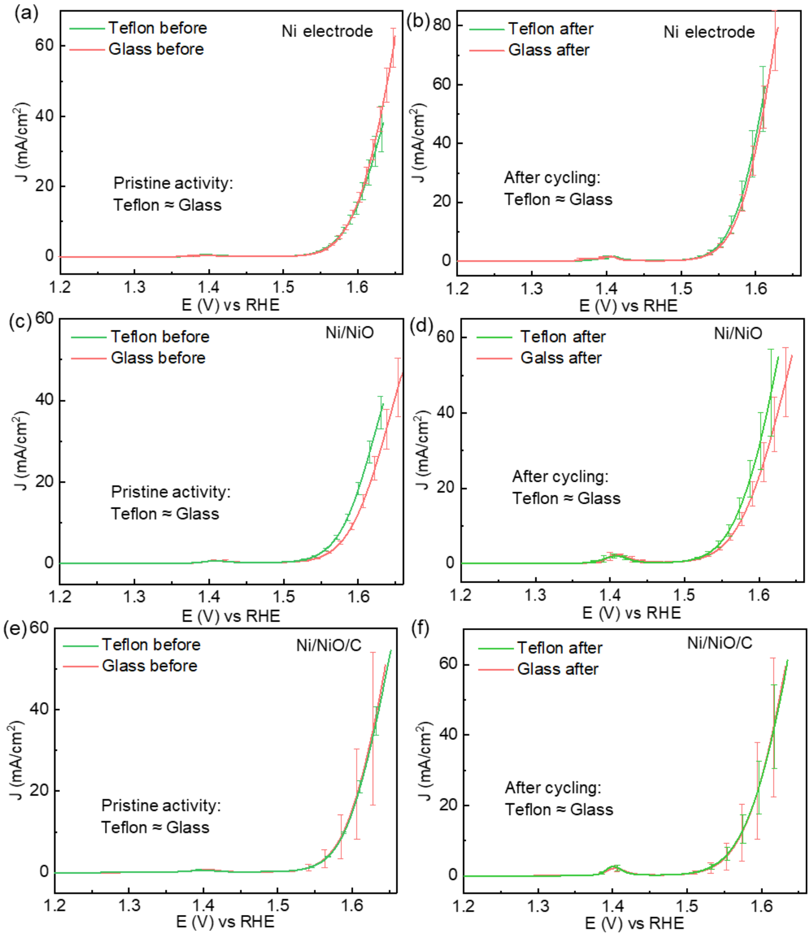

Figure 3.8 Polarization curves of (a,b) Ni electrode, (c,d) Ni/NiO and (e,f) Ni/NiO/C samples by two different cells before (a,c,e) and after (b,d,f) 1000 cycling process, including: Teflon cell b (green) and glass cell (red).

3.4.3 Electrolyte

A critical decision for OER measurements in alkaline conditions is the electrolyte. KOH and NaOH are the two commonly used electrolytes, but even with the same OH^- concentration a remarkable influence on the OER activity can be observed. **Figure 3.9**a-c presents the polarization curves of the Ni electrode, Ni/NiO, and Ni/NiO/C catalysts in two electrolytes. As can be observed the activities before and after 1000 cycles tested in KOH are superior to those tested in NaOH. The different metal cations K^+ and Na^+ in these two electrolytes could be the reason for the different activities of the same catalysts: Jin et al. found various ORR behavior in NaOH and KOH due to the size difference between potassium and sodium cations, resulting in different physicochemical properties such as solution viscosity, oxygen solubility, and oxygen diffusion coefficient.[141] By in situ surface-enhanced Raman spectroscopy, Suntivich et al. concluded that the cationic species modify the formation energy of ORR/OER intermediates, such as superoxo-$NiOO^-$, and then affect their catalytic performance.[148] Recently, it was pointed out that the inherently small variations of pH in different electrolytes, even at the same prepared molar concentration, were responsible for the OER activity, rather than the specific alkali metal cation or related hydroxides.[149]

In addition to the different cation species, the impurity in electrolytes, varying from various sources, also affects catalytical performance. For example, Alia et al. revealed that the electrolyte manufacturer and purity would impact the HER-HOR performances.[150] To avoid the influence of impurity from the electrolyte, especially Fe ions, considering its absorption and enhancement effect on nickel based OER catalysts, purified KOH was used and compared. **Figure 3.9**b-f present the polarization curves of the Ni electrode, Ni/NiO, and Ni/NiO/C samples in purified KOH and KOH before and after the 1000 cycles. The initial activity of the three catalysts in KOH is much higher than in purified KOH. This phenomenon has been reported and proved for Ni-based OER catalysts, the incorporation of

Fe could significantly increase the activity by charge transfer effect or increased active sites.[22–24,32,148] The Fe impurity will interact with the pristine Ni-based catalysts, resulting in the overestimated OER performance.[151] Therefore, the purification of KOH is necessary to reflect the intrinsic activity of Ni-based catalysts.

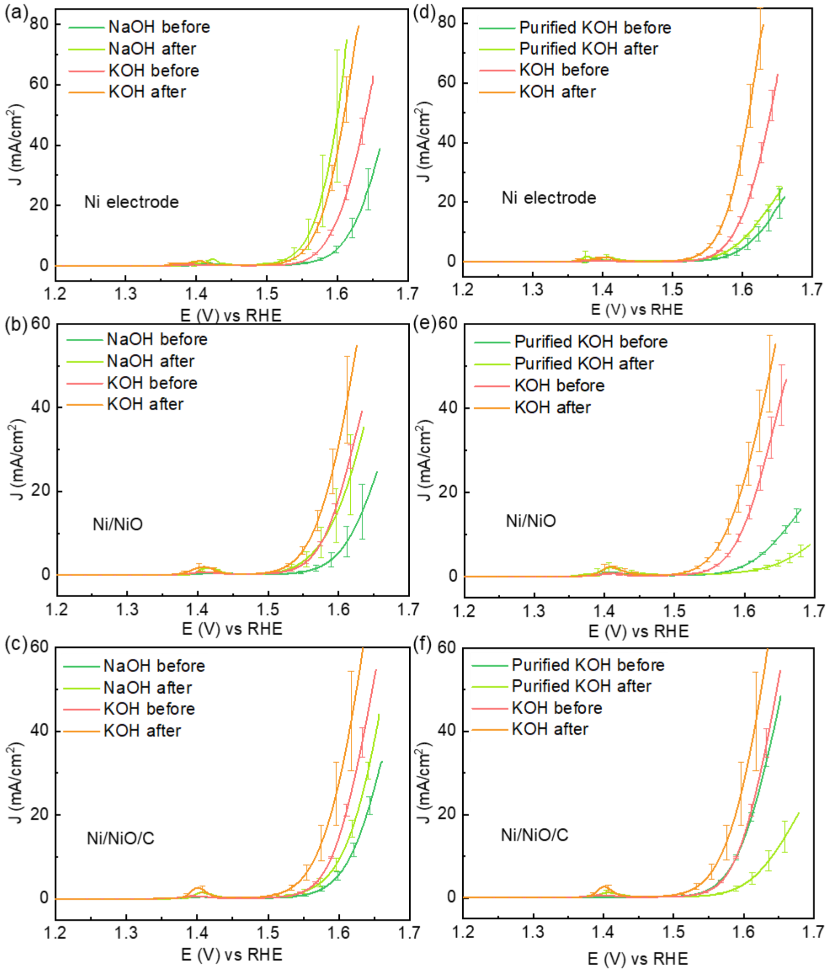

Figure 3.9 (a-c) polarization curves of (a) Ni electrode, (b) Ni/NiO and (c) Ni/NiO/C samples in two different electrolytes before and after 1000 cycling process, including: NaOH before (green) and after (red) 1000 cycles, KOH (light green) and after (orange). (d-f) polarization curves of (d) Ni electrode, (e) Ni/NiO and (f) Ni/NiO/C samples in two different electrolytes before and after 1000 cycling process, including: purified KOH before (green) and after (red) 1000 cycles, KOH (light green) and after (orange).

As shown in **Figure 3.9**b-f, the currents of LSV curves for Ni/NiO and Ni/NiO/C catalysts after 1000 cycles in purified KOH exhibit severe degradation compared with the initial curves. Ni electrode still presents increased activity during this process and maintains the same trends as in KOH. One possible reason for the difference in stability is the relationship between the catalyst and the GC electrode. The Ni electrode is stable enough as a whole, while Ni/NiO and Ni/NiO/C nanoparticles might fall off the electrode due to weak mutual connections. Although, no visible drop of the catalyst was observed in the electrolyte during the cycling process. To strengthen the connection of nanoparticles, we doubled the ratio of Nafion to ensure that the binder was sufficient in the preparation of the inks (the mass ratio of ionomer to catalysts is I/C = 12.5% and 25% when the Nafion fraction is increased from 5% to 10%).[152] However, this strategy did not improve the stability of Ni/NiO in purified KOH, and the degradation is still quite strong (**Figure 3.10**). The activity of Ni/NiO with 10% Nafion is lower than Ni/NiO with 5% Nafion because the active site is covered by more ionomer, which is consistent with the previous report.[152] This experiment demonstrates that catalyst dropping is not the reason for the degradation of Ni/NiO and Ni/NiO during the cycling process.

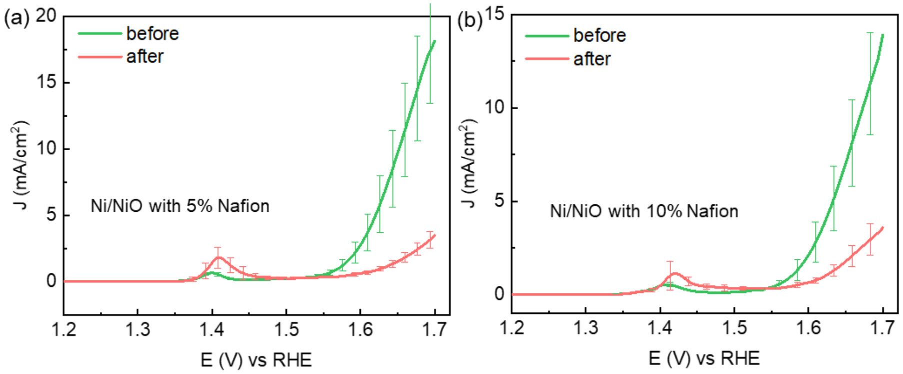

Figure 3.10 LSV curves of Ni/NiO catalysts with different ratio (a) 5%, (b) 10% Nafion before and after 1000 cycles between 1.0-1.7 V.

Considering their opposite trends, robust stability of Ni/NiO and Ni/NiO/C in KOH, a reasonable conjecture accounting for the degradation is the electrolyte, more specifically the Fe impurity. As we know, the Fe ions in KOH could be absorbed on nickel-species intermediates during the cycling process, then increase the OER activity of pristine catalysts to some extent, which could compensate for the intrinsic current loss of Ni/NiO and Ni/NiO/C in purified KOH, and distract the accurate evaluation of the real OER stability of Ni-based catalysts.

It is worth mentioning that there are generally two representative options for stability test strategies, including cycling the electrode in galvanostatic or potentiostatic tests over time. All former stability tests were performed during the cycling process, as this is a commonly-used protocol for evaluating OER catalysts.[11,72,76,78,91,93] Therefore, we also tracked the changes in the LSV curves of the three nickel catalysts after potentiostatic measurements at a fixed potential of 1.6 V for 4 hours, a similar duration to the 1000 cycling process. As shown in **Figure 3.11**a and b, the Ni/NiO and Ni/NiO/C catalysts show a slight increase in currents after 4 hours in KOH, similar to their trend during the 1000 cycle process. In contrast, the Ni/NiO and Ni/NiO/C catalysts show small or no degradation during potentiostatic testing in purified KOH (**Figure 3.11**c and d), which is significantly different from the sharp decrease during the 1000 cycles (**Figure 3.10**b and c)**.** The two strategies for stability test exhibit consistent trend in KOH but different results in purified KOH: unstable during the cycling process but quite robust at a constant potential.

This inconsistent behavior of stability in purified KOH seems unusual. In general, Ni-based catalysts may show degradation due to corrosion/etching at high oxidative potential during the potentiostatic process. In contrast, during the cycling process, catalysts will undergo oxidation and reduction from low potential to high potential back and forth, therefore situated at the high potential for less time overall and should exhibit more robust stability. One possible reason is that the degradation mechanism is closely related to the cycling process. A similar phenomenon reported for gold, a decay of the electrochemical activity occurs only in the reduction range from the cycling process. Avoiding the reduction process while using the potentiostatic measurements, dissolution and degradation will not happen.[153,154] Here, for the stability of Ni/NiO and Ni/NiO/C catalysts measured by potentiostatic tests, the oxidative potential is always present and no reduction reaction of nickel species, nickel dissolution, and general degradation could occur.

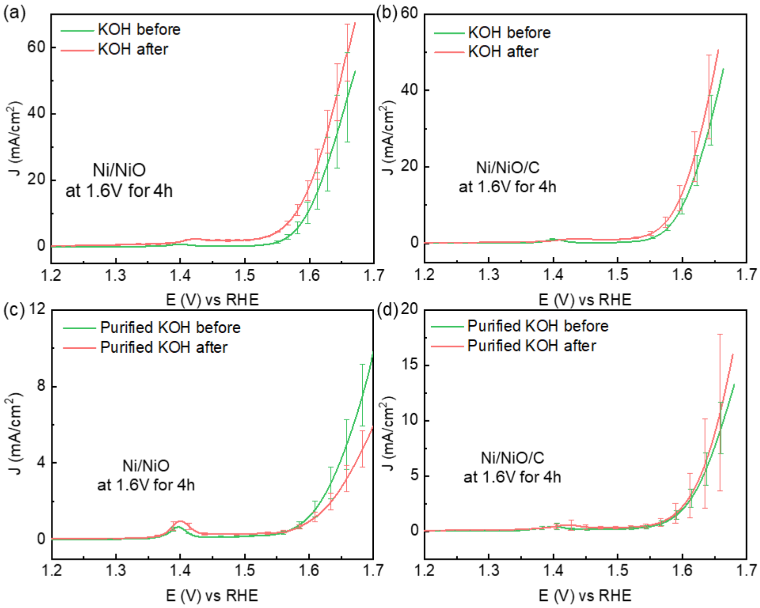

Figure 3.11 Potentiostatic stability of Ni/NiO and Ni/NiO/C catalysts. (a-d) polarization curves of (a,c) Ni/NiO and (b,d) Ni/NiO/C samples in KOH (a,b) and purified KOH (c,d) before and after potentiostatic test at 1.6 V vs RHE for 4 hours, LSV before (green) and LSV after (red). Different scales are chosen to present the OER performance of the catalysts in electrolytes.

Based on the above results, the cycling stability and potentiostatic stability of Ni-based catalysts are different in purified electrolytes. Recent work on the degradation mechanism of electrodeposited $Ni(OH)_2$ catalysts showed that irreversible phase transitions from β-$Ni(OH)_2$/β-NiOOH to γ-$Ni(OH)_2$/γ-NiOOH are responsible for the redox stability.[155] While we found the catalysts are pretty stable at constant potential, therefore, we suggest selecting the proper strategy to evaluate the stability of catalysts based on their actual application. Cycling stability of catalysts under fluctuating potentials on RDE simulates their working condition in fuel cells or an electrolyzer while potentiostatic stability simulates their utilization in an electrolyzer working with constant DC supplies.[144] Moreover, sufficient attention should be placed on the effect of the electrolytes to conclude the real degradation mechanism. the adsorption of iron impurity into Ni-based species should be considered as it will possibly mask the real loss of stability. Electrolyte purification is a non-ignorable procedure for a reliable evaluation of the intrinsic stability of Ni-based OER catalysts.

3.5 Catalyst loading

In general, to determine an optimal loading for OER, representative polarization curves of certain catalyst with different loadings were selected and presented in the work as the reported nominal activity.[73,156] However, objective comparisons between OER catalysts are blurred by the use of different loadings. Here, we selected two typical OER catalysts, commercial nickel oxide nanoparticles (denoted as Ni/NiO) and our own highly active NiFe Moreover LDH as different systems, designed a standardized protocol to compare the catalysts with various loading in terms of activity and stability.

3.5.1 Loading effect on OER activities

Therefore, the influence of added catalyst loading on their activities were investigated at different substrates, and firstly common GC used for RDE tests. Due to the relatively small geometric area of the GC electrode (~0.2 cm^2), the catalyst loading on GC is usually low, ranging from 0.1 to 0.5 mg/cm^2, with the loading of 0.2 mg/cm^2 the most typical.[11,77,83,91] Hence, we dropped cast NiFe LDH catalysts on GC with three different loading varying from 0.2 to 0.8 mg/cm^2

and compared the corresponding OER performance. When the loading increases from 0.2 to 0.4 mg/cm^2, the NiFe LDH electrode show higher current density and lower overpotential at 50 mA/cm^2 (**Figure 3.12**a and b), indicating better OER activity; Then more catalysts were further added to reach 0.8 mg/cm^2, the polarization curve and overpotential both show a decline in activity. In other words, a moderate loading of catalysts on GC present best OER activity while too less or too much loading will lead to degraded performance. This trend is also consistent with the findings of other catalysts in previous works.[73,156]

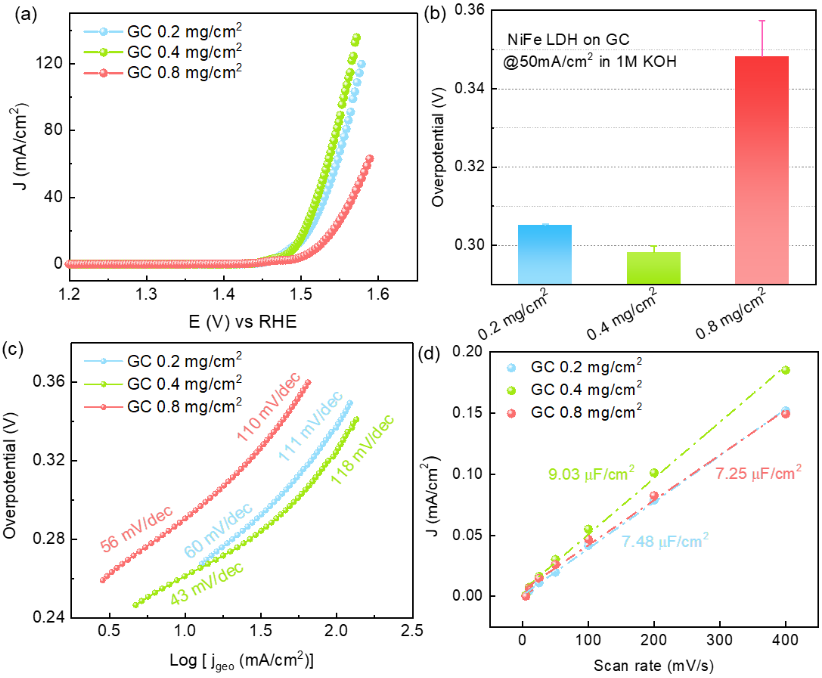

Figure 3.12 OER polarization curves of the NiFe LDH catalysts in 1 M KOH solution with different loadings on GC: 0.2, 0.4 and 0.8 mg/cm^2. The corresponding (b) overpotentials@50 mA/cm^2, (c) Tafel slopes and (d) ECSA tests.

To make clear the underlaying reason, we compared their Tafel slope and electrochemical surface area (ECSA, details in Experiment part) (**Figure 3.12**c and d). From 0.2 to 0.4 mg/cm^2, the NiFe LDH electrode show reduced Tafel slope from 60 to 43 mV/dec^1 and enlarged ECSA from 7.48 to 9.03 μF/cm^2, indicating more active site and faster kinetics, favoring the transport and separation of evolved charge and mass carriers. While a further increase of catalysts at 0.8 mg/cm^2 results in higher Tafel slope and reduced ECSA, probably due to the mutual coverage of powders and the increase resistance of charge transfer between catalysts and substrates.[2]

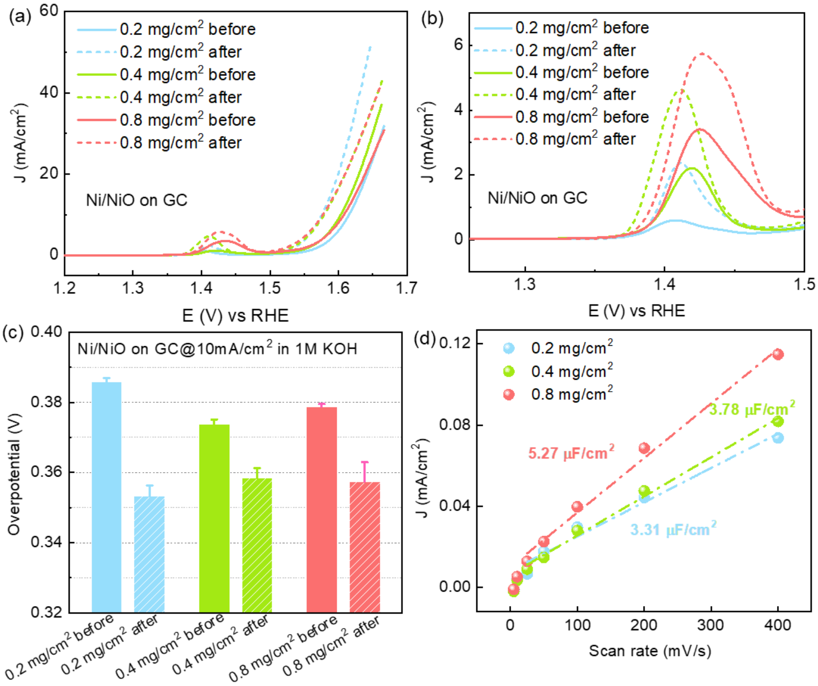

Figure 3.13 OER polarization curves of the Ni/NiO catalyst in 1 m KOH solution with different loadings on GC: 0.2, 0.4 and 0.8 mg/cm^2. The corresponding (b) amplifying of Ni oxidation region, (c) overpotentials@10 mA/cm^2 and (d) ECSA tests.

Besides of the homemade NiFe LDH catalysts, we also confirm the loading effect on GC electrode for commercial Ni/NiO powders (**Figure 3.13**). Similarly, as the loading increase gradually from 0.2 to 0.8 mg/cm^2, the corresponding Ni oxidation peak and ECSA enlarged simultaneously, indicating more Ni/NiO catalysts participate in the reaction. However, the highest activity plateau was obtained at 0.4 mg/cm^2, and the lower current density for 0.8 mg/cm^2 Ni/NiO at high potential was limited by mass transfer process.

To reduce the number of catalysts and increase their catalytic activity, nanostructure electrode in combination with large surface area substrates are often used, for example, catalysts coated on nickel foam (NF) or carbon paper (CP) supports. So we also investigated the effect of catalyst loadings on CP and NF. **Figure 3.14**a-c show the structure of NiFe LDH catalysts coated on CP with various loading 0.2, 0.4 and 0.8 mg/cm^2. The three-dimensional composite electrode structure supported by carbon fiber provide plenty of space for catalysts, hence, as the loading of NiFe LDH increase, the distributed catalysts on the fiber surface also gradually raise without serious inter-covering. This phenomenon is confirmed by their catalytical performance in **Figure 3.14**d and e, that their OER activities improve when the loading of NiFe LDH increase from 0.2 to 0.8 mg/cm^2 and reach a plateau at 1.2 mg/cm^2. At the same time, the gradually increasing nickel oxidation peak and the consequent weakening carbon oxidation peak in **Figure 3.14**f also verify the dominating role of catalyst itself and less involvement and influence from the CP substrate as more catalysts load.

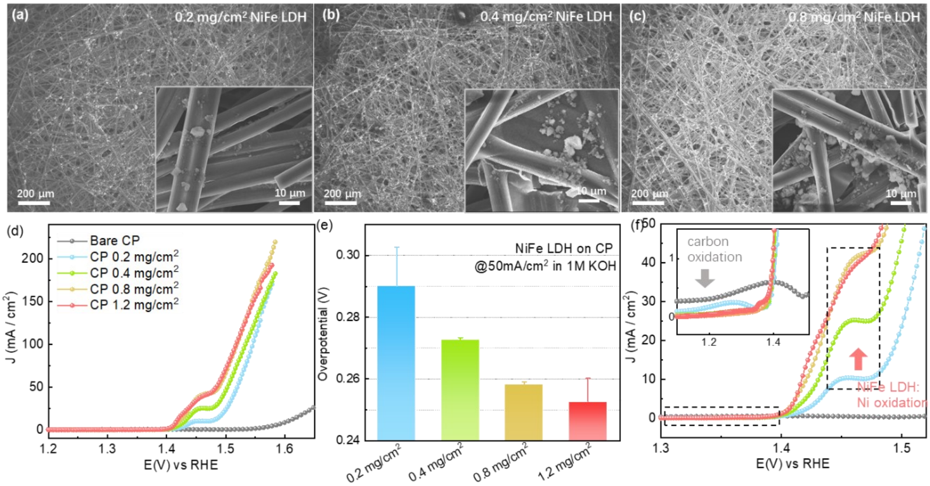

Figure 3.14 (a-c) SEM images of the NiFe LDH catalysts with different loadings on CP: 0.2, 0.4 and 0.8 mg/cm^2. The corresponding (d) OER polarization curves, (e) amplifying of carbon and nickel oxidation region and (f) overpotentials@50 mA/cm^2.

In addition, the effect of catalyst loading on NF show similar trends: SEM images in **Figure 3.15a-c** indicate more NiFe LDH catalysts are gradually coated on the NF surface with increasing load. The electrochemical behavior in **Figure 3.15d-f** demonstrates NF are partly covered by catalysts when firstly 0.2 mg/cm^2 NiFe LDH are coated, with increased OER current, reduced overpotential and weakened nickel oxidation from NF. Then the catalyst loading start to increase from 0.2 to 0.4 mg/cm^2, more catalysts cover the substrate and participate in OER process with more notable activity. While a further increased loading reaches to 0.8 mg/cm^2, there is no greater activity together with the almost unchanged nickel oxidation peaks from NF substrate and NiFe LDH catalysts. This conclusion is also in agreement with the trend reported in the literature.[157]

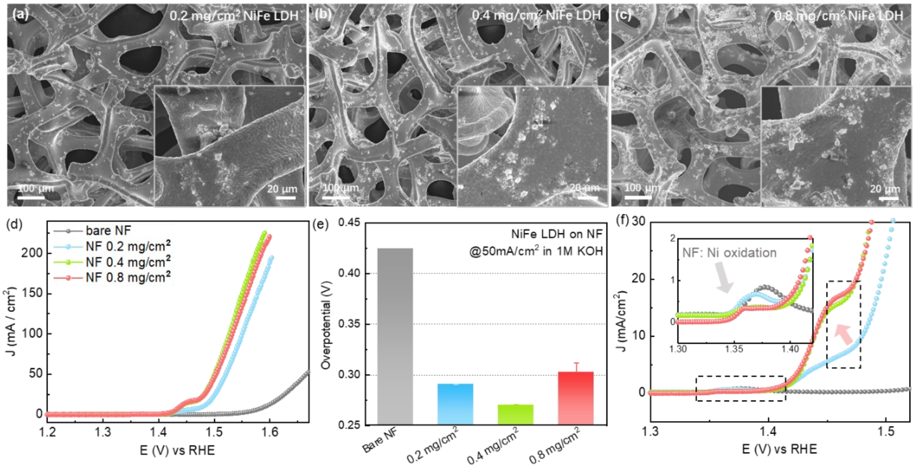

Figure 3.15. (a-c) SEM images of the NiFe LDH catalysts with different loadings on NF: 0.2, 0.4 and 0.8 mg/cm^2. The corresponding (d) OER polarization curves, (e) amplifying of the nickel oxidation region and (f) overpotentials@50 mA/cm^2.

In addition to the homemade NiFe LDH catalysts, we also compared the OER activities of commercial Ni/NiO powders on NF and CP with different loadings (**Figure 3.16**). Consistently, the area of the associated nickel oxidation peak increases with larger loadings, but the corresponding OER activity does not raise indefinitely. Based on the above results, catalyst loading exhibits an unignorable effect on the activity: in a certain range, an increased loading will lead to a higher current density due to the involvement of more active sites in the reaction, but a further increase in loading does not bring a sustained enhancement in activity, due to the catalyst inter-coverage and mass transfer at large current densities. Also, this effect is more pronounced for the highly active NiFe LDH catalysts while the difference in activity for different loadings is relatively slight for common Ni/NiO catalysts. Therefore, the effect of catalyst loading on OER activity should be emphasized and it is necessary to use same loading to compare different catalysts.

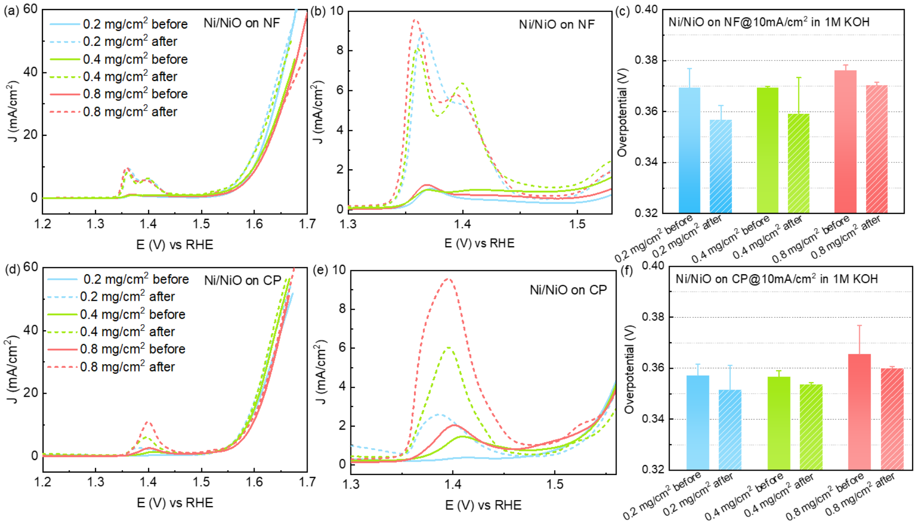

Figure 3.16 (a-c) OER polarization curves, (b) amplifying of nickel oxidation region and (c) overpotentials@10 mA/cm^2 of the Ni/NiO catalysts with different loadings on NF: 0.2, 0.4 and 0.8 mg/cm^2 before and after cycling between 1.0-1.7 V for 1000 cycles. (d) OER polarization curves, (e) amplifying of nickel oxidation region and (f) overpotentials@10 mA/cm^2 of the Ni/NiO catalysts with different loadings on CP: 0.2, 0.4 and 0.8 mg/cm^2 before and after cycling between 1.0-1.7 V for 1000 cycles.

3.5.2 Loading effect on cycling stability

Stability is another critical merit when designing OER catalysts for applications as practical water electrolyzers have to operate consistently and efficiently over a long time (over thousands of hours or cycles). Therefore, it is also essential to consider the effect of loadings on catalyst stability performance. There are two common strategies used for stability measurements: cycling the electrode and keeping the electrode at galvanostatic or potentiostatic conditions, simulating their respective situations for practical applications.[144]

Here, we firstly investigate the cycling stability of NiFe LDH catalysts with different loadings 0.2, 0.4 and 0.8 mg/cm^2 by comparing their polarization curves before and after cycling between 1.0-1.7 V for 1000 times in 1 M KOH. As shown in **Figure 3.17**a and d, all the NiFe LDHs on GC electrode show reduced current densities and increased overpotentials, indicating degraded performance during the cycling process. More severe degradation for 0.8 mg/cm^2 may come from the low conductivity and mass transfer limitations at high loadings.

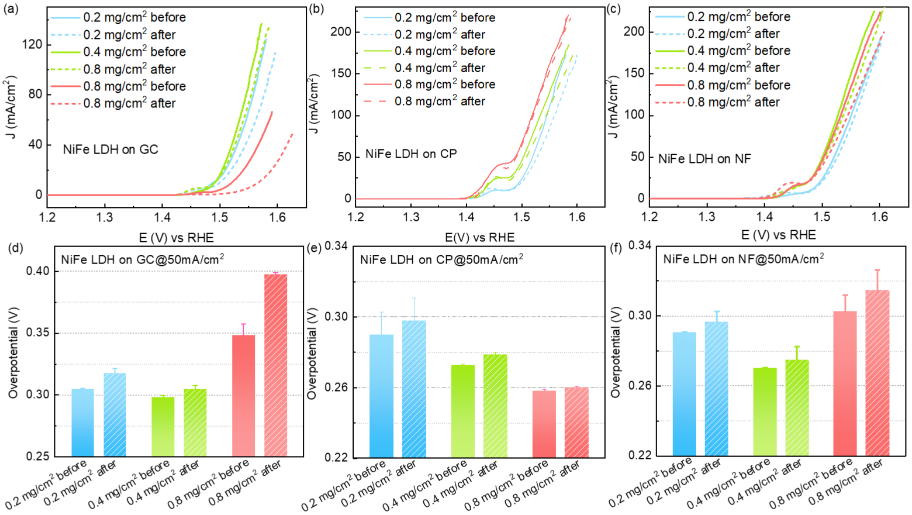

Figure 3.17 (a-c) OER polarization curves and (d-f) corresponding overpotentials@50 mA/cm^2 of the NiFe LDH catalysts with different loadings 0.2, 0.4 and 0.8 mg/cm^2 on various substrates before and after cycling between 1.0-1.7 V for 1000 cycles in 1M KOH. NiFe LDH on (a,d) GC, (b,e) NF and (c,f) CP. Different scales are chosen in a and d to present the OER performance of the various electrodes clearly.

Similarly, NiFe LDH catalysts with different loadings on NF and GC (**Figure 3.17**b-f) exhibit comparable stability trend, a certain degree of decline. Equivalent experiments were also conducted in the Ni/NiO catalysts with different loadings

(**Figure 3.16**), which exhibited certain degree of activity improvement for all the three kinds of substrates regardless of the load. Namely, the catalyst loading does not affect its performance in terms of cycling stability trend, although the degree of changes may vary slightly.

3.5.3 Loading effect on potentiostatic stability

The possible correlation between the catalyst loading and their potentiostatic stabilities were also checked. As shown in **Figure 3.18**, the polarization curves and corresponding overpotentials of NiFe LDH catalysts with two loading on a certain substrate before and after keeping at 1.6 V for 20 h were recorded, the catalysts on each substrate GC, CP or NF show a certain degree of decrease in current density and increase in overpotential, indicating the same stability trend for different loadings at 0.2 and 0.8 mg/cm^2. Such conclusion can also be confirmed from the identical experiments in the Ni/NiO system with different loading but similar activity enhancement after constant potential aging process (**Figure 3.19**). The different stability trend of NiFe LDH and Ni/NiO catalysts indicate their distinct intrinsic electrochemical properties, an improvement due to the formation of active nickel hydroxides for Ni/NiO while metal dissolution leading to the degradation for NiFe LDH (details discussed in Chapter 4). Above all, the loading does not change the potentiostatic stability of the Ni/NiO catalysts as well.

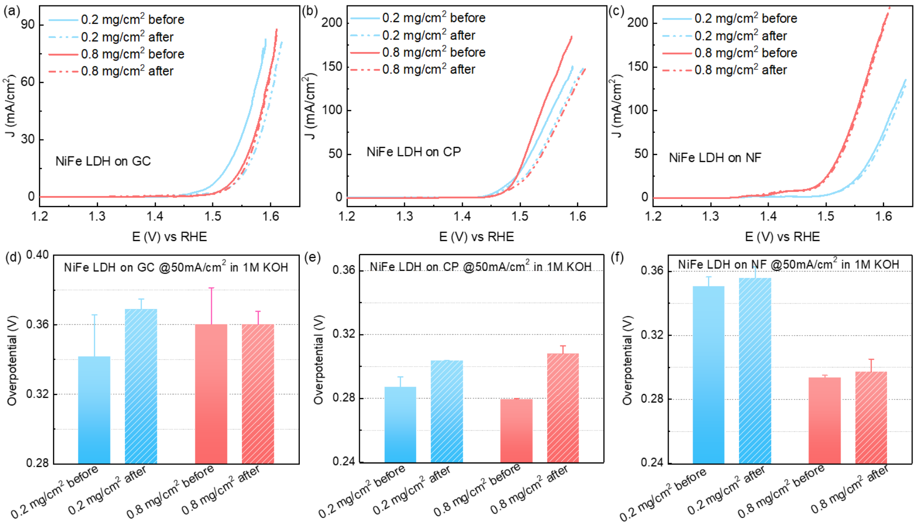

Figure 3.18 Loading effect on the potentiostatic stability of NiFe LDH catalysts. (a-c) OER polarization curves and (d-f) corresponding overpotentials@50 mA/cm^2 of the NiFe LDH catalysts on various substrates before and after keeping at 1.6 V for 20 h in 1 M KOH solution. NiFe LDH on (a,d) GC, (b,e) NF and (c,f) CP. Different scales are chosen in a and d to present the OER performance of the various electrodes clearly.

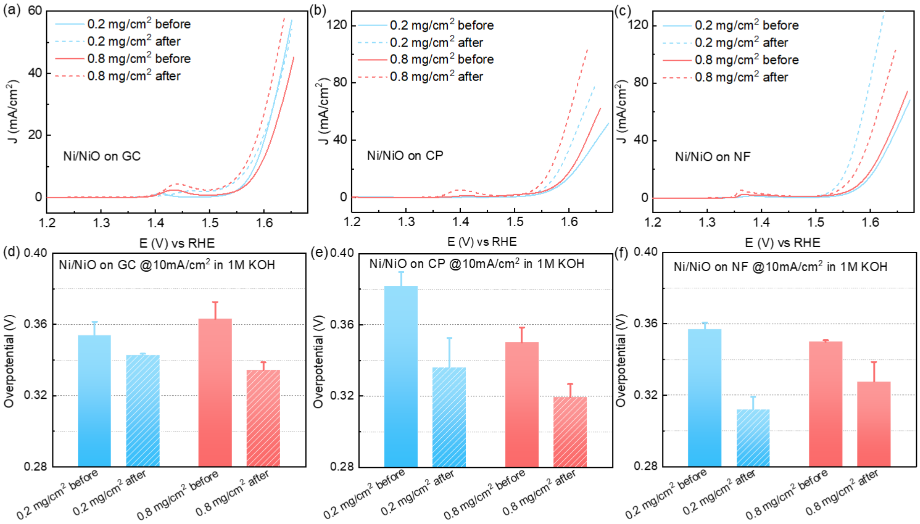

Figure 3.19 OER polarization curves of the Ni/NiO catalysts on various substrates before and after keeping at 1.6 V for 20 h in 1 M KOH solution. NiFe LDH on (a) GC, (b) NF and (c) CP. (d-f) The corresponding overpotentials@10 mA/cm^2, respectively.

3.6. Substrate effect

The effect of loading on catalyst performance has been demonstrated in the previous section, but at the same, the substrates, served as current collectors and mass supports, also exhibits obvious influence on the OER performance of NiFe LDH and Ni/NiO catalysts from the last section. Catalyst substrates are very sensitive to OER process, but not always the same in the reported testing protocols. Among them, CP and NF are suitable candidates for catalyst support besides GC due to their low cost, excellent conductivity, mechanical strength, and chemical stability under alkaline conditions.[66,75,85,89] Thus, an objective evaluation of OER catalysts will be blurred by the different substrates. Therefore, in this section, the performance of NiFe LDH catalysts on GC, CP, and NF is compared and the possible effects of the substrates on OER activity and stability are investigated.

3.6.1 Substrate effect on OER activity

The structures of NiFe LDH catalysts on various substrates were observed by SEM images, as shown in **Figures 3.20**a-c, the NiFe LDH nanosheets covered with each other and stacked on top of each other for the powders, while they are more dispersed on the surface of the NF and CP supports. Consequently, such electrodes will have a larger active area, which was confirmed by the higher nickel oxidation peaks when NiFe LDHs were coated on NF and CP compared with their counterparts on GC (**Figure 3.20**d and f). Their corresponding current densities and overpotentials also state the substrate effect on the OER activities: NiFe LDH/CP > NiFe LDH/NF > NiFe LDH/GC. This trend is more obvious when we added 0.8 mg/cm^2 NiFe LDH (**Figure 3.20**d-g), owing to the more crucial role of catalyst distribution at high loadings.

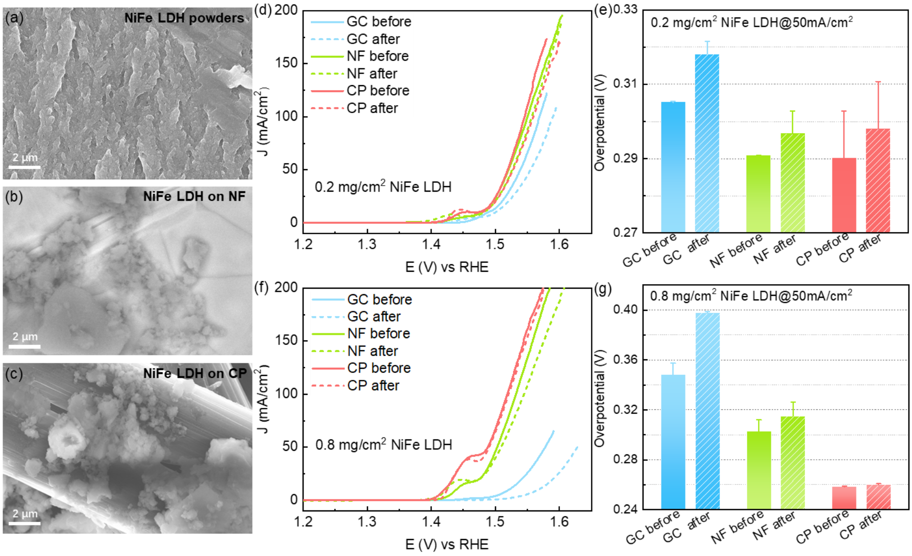

Figure 3.20 (a-c) SEM images of the NiFe LDH catalysts on various substrates. (a) initial NiFe LDH powders, NiFe LDH on (b) NF and(c) CP. The corresponding (d,f) OER polarization curves and (e,g) overpotentials@50 mA/cm^2 before and after cycling between 1.0-1.7 V for 1000 cycles in 1M KOH. Among them, (d,e) the loading of NiFe LDH is 0.2 mg/cm^2 while (f,g) the loading of NiFe LDH is 0.8 mg/cm^2.

This type of effect has also been studied for Ni/NiO catalysts. As shown in **Figure 3.21**, Ni/NiO on porous 3D NF and CP supports show higher current density and lower overpotential compared to Ni/NiO on GC for two loadings at 0.2 and 0.8 mg/cm^2. Although the substrate effect is weaker due to the low intrinsic activity of Ni/NiO catalysts compared to NiFe LDH, it can be assumed that the influence of the substrate is crucial for most of the reported highly active catalysts. However, previous literatures often selected coated catalysts with high loadings on substrates other than GC to evaluate the performance of OER, for example, over 1 to 4 mg/cm^2 catalysts on NF or CP.[74,76,81,87,94] Our results show that the substrates contribute significantly to the nominal activities of the catalysts, especially at high loadings, therefore these conditions need to be carefully considered to give a fair evaluation of the activity of different catalysts.

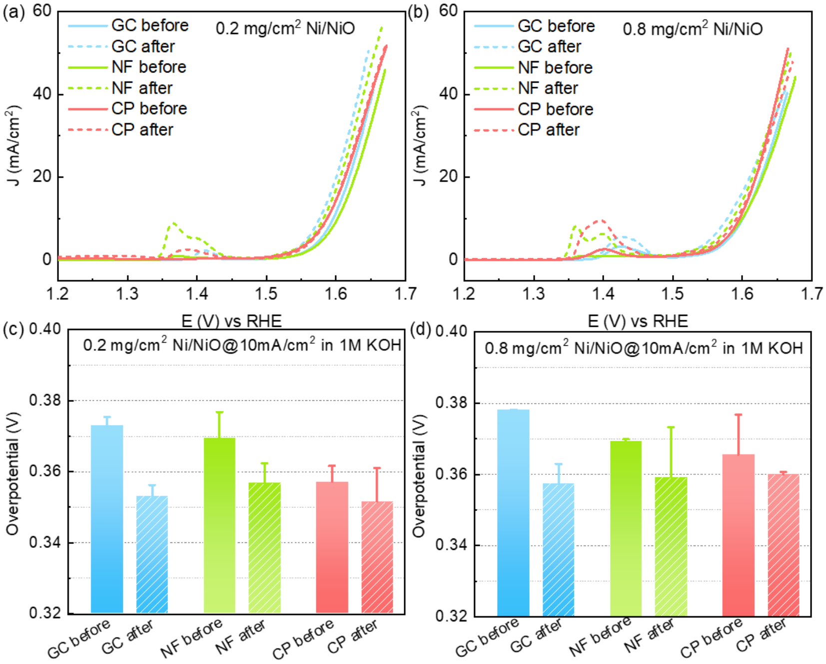

Figure 3.21 (a-b) OER polarization curves, and (c,d) overpotentials@10 mA/cm^2 of Ni/NiO catalysts before and after cycling between 1.0-1.7 V for 1000 cycles in 1M KOH. Among them, (a,c) the loading of Ni/NiO is 0.2 mg/cm^2 while (b,d) 0.8 mg/cm^2.

3.6.2 Substrate effect on cycling stability

Besides the activity, the OER stability of catalysts is often evaluated on other substrates, for instance, NF or CP, not conventional GC, therefore, it is necessary to figure out whether these different substrates will affect the stability performance of catalysts. As shown in **Figure 3.20**d-g, 0.2 and 0.8 mg/cm^2 NiFe LDH catalysts on GC, NF, and CP all exhibit reduced current density and increased overpotential after 1000 cycles, while a slight difference of their degradation degree might come from the distinct involved active site numbers owing to the substrates. At the same time, the counterparts of Ni/NiO catalysts in **Figure 3.21** show the same stability trend on different supports. In general, the supports do not change the OER stability trend of the loaded catalysts.

3.6.3 Substrate effect on potentiostatic stability

Compared with cycling stability, where the electrode's cycle in an oxidation/reduction process between high and low potentials, potentiostatic stability of OER catalysts implies continuous oxygen evolution process at constant high potential. Therefore, it can be inferred that the mass transfer and gas diffusion during potentiostatic conditions therein may be influenced more by the substrate of the electrode. **Figure 3.22** illustrates a comparison of the stability of the NiFe LDH catalysts in different supports for both 0.2 and 0.8 mg/cm^2 loadings, the polarization curves and overpotentials indicating a consistent trend of stability, the degradation before and after holding at 1.6 V for 20 hours. Such similar results, roughly comparable activation was also observed for all the Ni/NiO catalysts coated on GC, NF, and CP after the same treatment process (**Figure 3.23**). Therefore, the present results indicate that different substrates (at least NF and CP) can be used for stability testing of catalysts.

However, it is worth noting that the potentiostatic stability of catalysts on GC is not always easy to achieve, as the electrode sometimes exhibits a significant current drop and an obvious catalyst drop after maintaining the potential for a certain period. This may be because the oxygen bubble, which is continuously produced from the catalytic layer at high potential, loosens the catalyst film and reduces the bonding within or with the substrate, eventually causing some of the catalysts to fall off the GC electrode. In contrast, the porous 3D structures of NF and CP are more conductive to gas diffusion and transport, so there is almost no obvious catalyst drop-off. This may be the reason why most of the previous literature has chosen NF or CP instead of GC for potentiostatic stability tests.

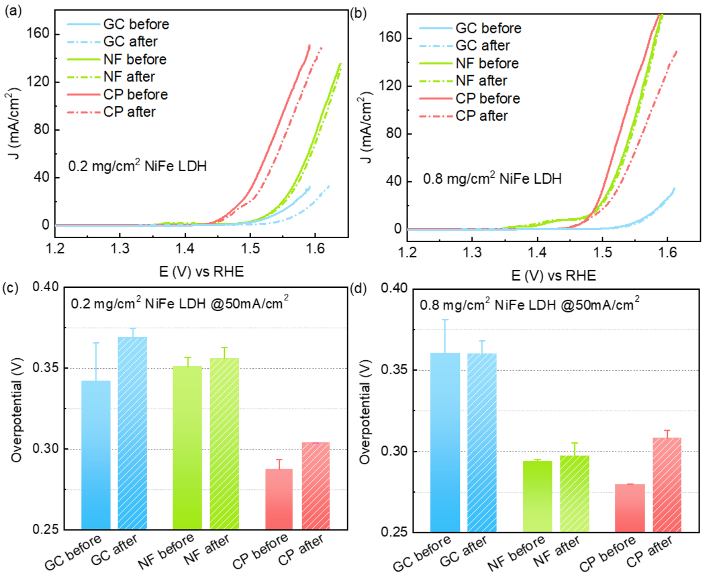

Figure 3.22 (a-b) OER polarization curves, and (c,d) overpotentials@50 mA/cm^2 of the NiFe LDH catalysts on various substrates before and after keeping at 1.6 V for 20 h in 1 M KOH solution. Among them, (a,c) the loading is 0.2 mg/cm^2 while (b,d) 0.8 mg/cm^2.

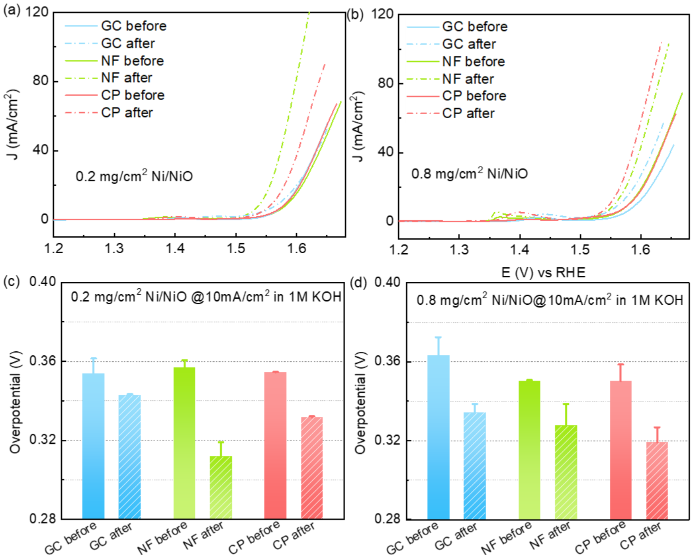

Figure 3.23 (a-b) OER polarization curves, and (c,d) overpotentials@10 mA/cm^2 of the Ni/NiO catalysts on various substrates before and after keeping at 1.6 V for 20 h in 1 M KOH solution. Among them, (a,c) the loading is 0.2 mg/cm^2 while (b,d) 0.8 mg/cm^2.

3.7 Benchmark Ni-based OER catalysts

As we summarized in Chapter 1, numerous Ni-based catalysts have presented predominant OER activity, combined with various methods to improve their performance by increasing their active surface area and optimizing the intrinsic electronic structure. However, it is still not straightforward to make a reliable and fair comparison of the intrinsic OER activities of different Ni-based catalysts. As summarized in **Table 1.1**, the detailed test conditions for each catalyst among different groups show multiple and obvious differences. The most noticeable parameter is the loading of the catalysts, ranging from 0.02 mg/cm^2 for NiO nanoparticles to 4 mg/cm^2 for NiFeP nanoplates. Although not all supported catalysts are fully involved in the reaction, the surface area and active sites will increase, which undoubtedly contribute to the superior activity. In addition, the testing protocols of these catalysts also differ between each other. As we discussed above, the possible effect of each component in the test setup on OER performance is crucial and several protocols were recommended in last sections. Therefore, we selected three typical Ni-based catalysts with the excellent performance, repeated their synthesis process, and then evaluated their OER activity by our proposed protocol.

1) Bimetallic phosphide NiFeP nanoplate arrays on a Ni foam substrate. According to the literature, the incorporation of Fe and the supported 3D architecture enhanced the catalytic activity;[76]

2) Amorphous NiFeMo oxides

According to Duan et al., faster surface self-reconstruction during OER would form a metal core with oxy(hydroxide) shell structure, leading to superior OER activity;[142]

3) NiFeCu oxyhydroxides.

It was demonstrated that effective hydroxides with multi-metal sites supported on Ni foam, enhance the water oxidation performance.[158]

The samples were synthesized according to the described method, details can be found in the experimental part. To confirm the designed materials, XRD was used to check the crystal phase, as presented in **Figure 3.24**, all the main peaks are well consistent. The OER activity was checked by the reported protocol and our suggested protocol.

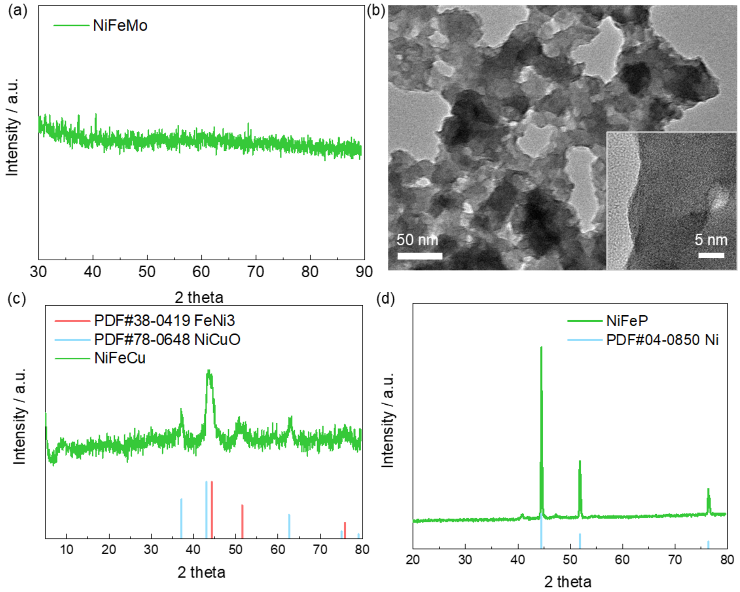

Figure 3.24 Characterization of synthesized Ni-based materials. (a) XRD pattern and (b) TEM images of amorphous NiFeMo. XRD pattern of (c) NiFeCu and (d) NiFeP.

As presented in **Figure 3.25**a, the OER activity of the NiFeP nanoplate arrays tested with our protocol shows a higher current than the reported results. This improvement may be due to the added activation process in our proposed test protocol (10 cycles before the LSV test), the improved activity is also consistent with the trend in the Ni electrode system. For NiFeMo oxides, a similar improved activity by our proposed protocol as shown in **Figure 3.25**b, the main reason is the electrolyte concentration. In the reported work, 0.1 M KOH was used for the tests, while 1 M KOH was used to ensure the same test conditions for a fair comparison with the other catalysts.

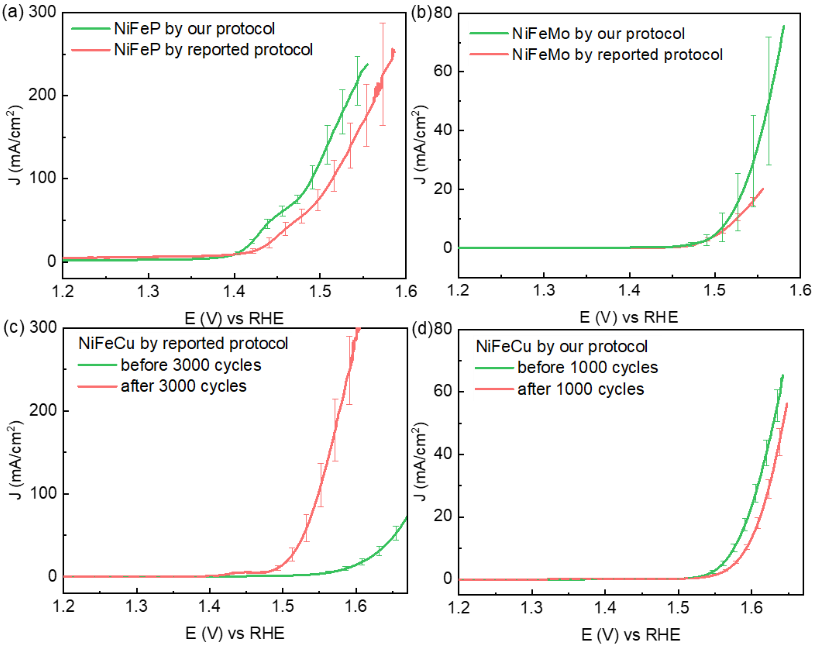

Figure 3.25 OER activity of three typical Ni-based catalysts. (a) NiFeP nanoplate arrays, (b) amorphous NiFeMo oxides and multi-metal-site NiFeCu oxyhydroxide by (c) reported protocols and (d) our testing protocols. Different scales of these figures are used due to the distinct performance of these catalysts.

In contrast to these two catalysts, a more dramatic difference between the two protocols was observed for NiFeCu catalysts. NiFeCu oxyhydroxides formed after 3000 cycles show significantly increased activity compared to an untreated sample, as reported and shown in **Figure 3.25**c. However, the LSV curves tested with our protocol show the opposite trend: there are a slight deterioration and no improvement of NiFeCu after the cycling process presented in **Figure 3.25**d. The main difference is the substrate used in the original test, Ni foam was chosen as the working electrode with a mass loading of 0.8 mg/cm^2, while we applied the catalyst ink to the GC electrode with 0.2 mg/cm^2 as commonly used for GC electrode. The initial loading of the reported catalysts is four times larger but with lower activity compared to our protocol, which might be due to the activation treatment. The LSV changes during the cycling process may indicate the influence of the substrate on stability. The Ni foam with a large surface area supports the whole NiFeCu catalyst to undergo a continuous activation process and form oxyhydroxides, while the surface area of the catalyst on the GC electrode is limited and only a part is converted into active species. Another effect from the Ni foam itself should also not be ignored: the similar electrochemical activation from a nickel to active hydroxides at high potential could also participate in the OER process and contribute to the overall nominal currents of the integrated electrode.

3.8 Chapter summary

Driven by the commercial application of electrolyzers to store and transfer clean energy, nonprecious Ni-based OER, used under alkaline conditions, has become one of the most active areas and has attracted intense efforts. In this chapter, we evaluated and compared different criteria for OER measurements. By experimentally comparing different test components, we discussed their underlying effects on the evaluation of catalysts. For example, the oxidation current for carbon material as a counter electrode will overlap with the nickel redox peak and the overall activity, and also the dynamic changes of bubbles on the electrode during the long-term tests will lead to unreliable evaluation of OER stability. Therefore, we recommend to use Pt materials as counter electrode, Teflon cell as electrolysis cell for alkaline OER measurements, and conduct CV activation and reductive potential treatment before activity test as well as LSV comparison before and after, not direct CV cycles or potentiostatic curves for stability evaluation.

A series of loadings, three types of substrates GC, NF, and CP, and two types of catalysts, NiFe LDH and Ni/NiO were tested for the OER to understand the effects of loading and support on activity, cycling stability, and potentiostatic stability. The ECSA of the catalysts increased with increasing loading, but the activity reached a plateau at optimum loading and then decreased due to mass transfer resistance, ohmic resistance, etc. Meanwhile, the catalyst substrates showed a dramatic influence on the OER activities, especially at high loading or high-efficiency catalysts. More catalysts on porous NF and CP substrates will expose additional active sites, while high-efficiency catalysts will enhance this effect. Thus, when reporting the activity of a novel catalyst or making comparisons with previously known catalysts, we need to pay attention to the two factors of loading and substrate and have to keep them consistent during the experiments. In contrast, neither catalyst showed any change in the catalyst stability trend, including cycling stability and potentiostatic stability. This proves the reliability of the stability tests with supports other than GC in the literature.

This chapter contributes to understanding the influence of loading and substrate on the performance of OER catalyst, guides the experimental measurement of catalyst performance, and then provides objective and reasonable comparisons for mechanism research from different research groups based on these studies and recommended protocols.

Chapter 4 Composition dependent structure and OER property of NiFe LDH catalysts

4.1 Background and motivation

As we summarized in chapter 1, designing and developing highly effective transition-metal catalysts to boost the OER process for alkaline water electrolyzer is essential.[3,4,159,160] NiFe-based LDH is an electrocatalytically active and promising candidate due to more exposed active sites from its unique lamellar structure and leading intrinsic activity with flexible chemical modulation of Ni and Fe. [100,102,107,110,161–164] However, it is not clear whether the tuning of elemental ratio of Ni/Fe will affect the spatial size, morphology, and crystallinity of NiFe LDHs. Meanwhile, despite the reported exciting promotion on OER activity of LDHs, their corresponding influence on temporal stability of catalysts, also important for actual application, is still hardly addressed.[107,118] Moreover, for the development of AEM electrolyzer, though several latest works have reported performance breakthroughs by using novel non-noble-metal catalysts,[122–124] these catalysts are synthesized by a relatively complex process with the assistant of high temperature, or long time and organic solvents. These will enlarge the cost for catalyst production and limit the practical application from economic perspectives.

Therefore, a kind of active and durable NiFe LDH, synthesized by facial method, is desirable. It could meet the requirements of both high efficiency and low cost, validating its potential commercial application in AEM electrolyzers. We will use a simple precipitation method to tune the composition and structure of NiFe LDHs. The atomic and electronic structure of NiFe LDHs with different Ni/Fe ratios will be investigated by different techniques, like XRD, TEM, XPS and XAS to understand the correlation of composition and structure. Their catalytical performance in RDE and water electrolyzer will be compared with other reported catalysts and the corresponding dynamic phase transition of NiFe LDH will also be verified by in situ Raman spectra. Part of the results of this chapter have already been published.[165]

4.2 Synthesis and characterization of NiFe LDHs

As claimed in chapter 2, the NiFe LDHs were synthesized by a precipitation method and the different ratio of Ni and Fe was controlled by the added Ni and Fe precursors. As illustrated in **Figure 4.1**, Ni^{2+} and Fe^{3+} ions were evenly dispersed then poured into 0.15 M NaOH aqueous solution under vigorous stirring. Then the precipitates appear immediately because of the low solubility of Ni/Fe in alkaline conditions. Therefore, although there is a theoretical sequential precipitation of Ni/Fe, the precipitation process is completed in a very short time at the environment of excessive OH^-, so the former already uniformly dispersed Ni/Fe ions in the solution come into homogenously distributed solids accompanied by high-speed stirring.

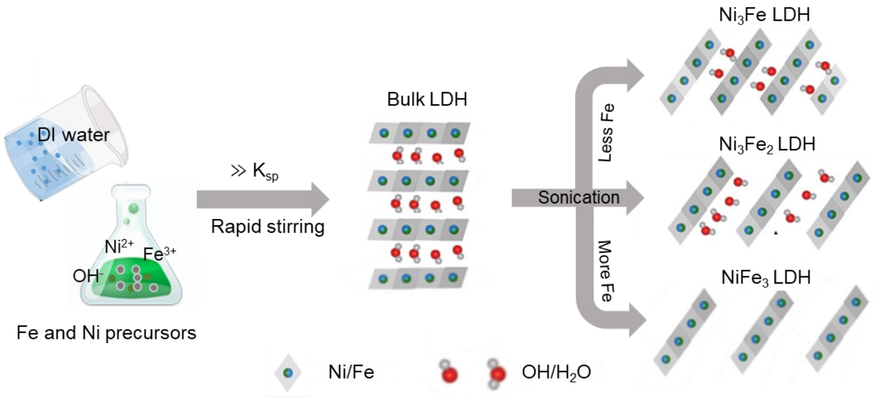

Figure 4.1 Schematic illustration of the preparation process of NiFe LDHs.

The compositions of different NiFe LDHs were verified by EDX in SEM and ICP-OES analysis, named as Ni_3Fe LDH, Ni_3Fe_2 LDH, and $NiFe_3$ LDH (**Table 4.1** and **Figure 4.2**). The consistent values with slight error bar from ICP and EDS data indicate the even distribution of metal sites. SEM images confirm the morphologies of these samples, which are nanoplates especially obvious for Ni_3Fe LDH. Although the details could not be observed from SEM due to the resolution limitation, the gradual structural changes of these NiFe LDHs are clear: Ni_3Fe LDH is undulating multilayer nanosheets and gradually smooth for the others.

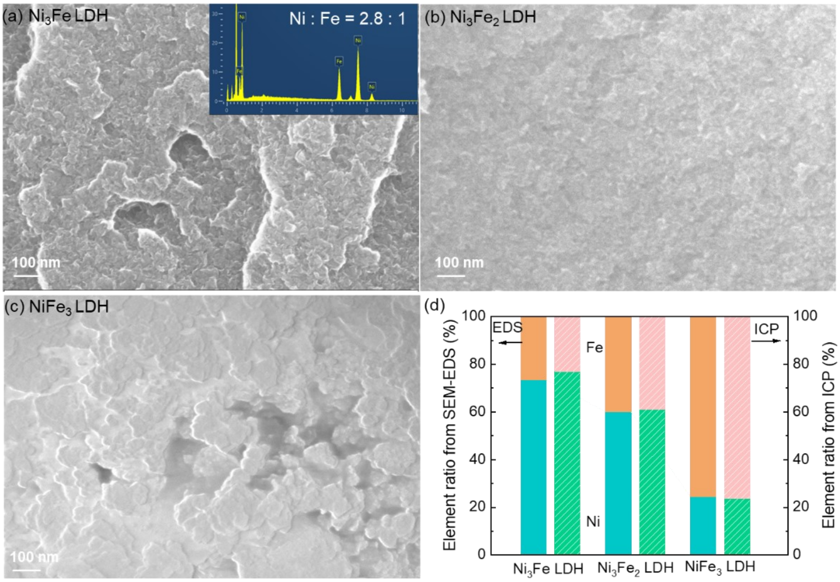

Figure 4.2 (a-c) SEM images of Ni_3Fe LDH, Ni_3Fe_2 LDH and $NiFe_3$ LDH. (d) Element ratio of Ni/Fe in NiFe LDHs by EDX (solid filled bars) and ICP (pattern filled bars).

Table 4.1 Element ratio of Ni/Fe in NiFe LDHs by EDX and ICP.

Sample	Input ratio (Ni:Fe, at%)	Actual ratio (Ni:Fe, at%) by EDX (ε ≤ 1%)	Actual ratio (Ni:Fe, at%) by ICP (ε ≤ 1%)
Ni_3Fe LDH	4:1	73.5: 26.5	77.0: 23.0
Ni_3Fe_2 LDH	2:1	60.0: 40.0	61.0: 39.0
$NiFe_3$ LDH	1:1	24.4: 75.6	23.6: 76.4

Their crystal structures were verified by XRD patterns in **Figure 4.3**a. The Ni_3Fe LDH (green curve) exhibits the same Bragg reflections as typical NiFe LDH

(JCPDS#40-0215 NiFe LDH). The two obvious clear peaks at 11° and 22° are attributed to the characteristic (003) and (006) planes of the layered structure in the c axis,[102,166] and as the ratio of Fe/Ni increases, the relative peak intensity of (003) and (006) planes compared with other peaks decrease in Ni_3Fe_2 LDH (**Figure 4.3**a, orange curve) and almost disappear for $NiFe_3$ LDH (**Figure 4.3**a, red curve). This trend indicates the changes of spatial structure, agreeing well with the literatures that the absence of (00n) peaks in the XRD patterns evidences the successful exfoliation of multilayers into monolayers.[102,103,109,110] Surely the absence of crystal peaks might also result from the reduced crystallinity of amorphous structure, which we need to confirm by other techniques.

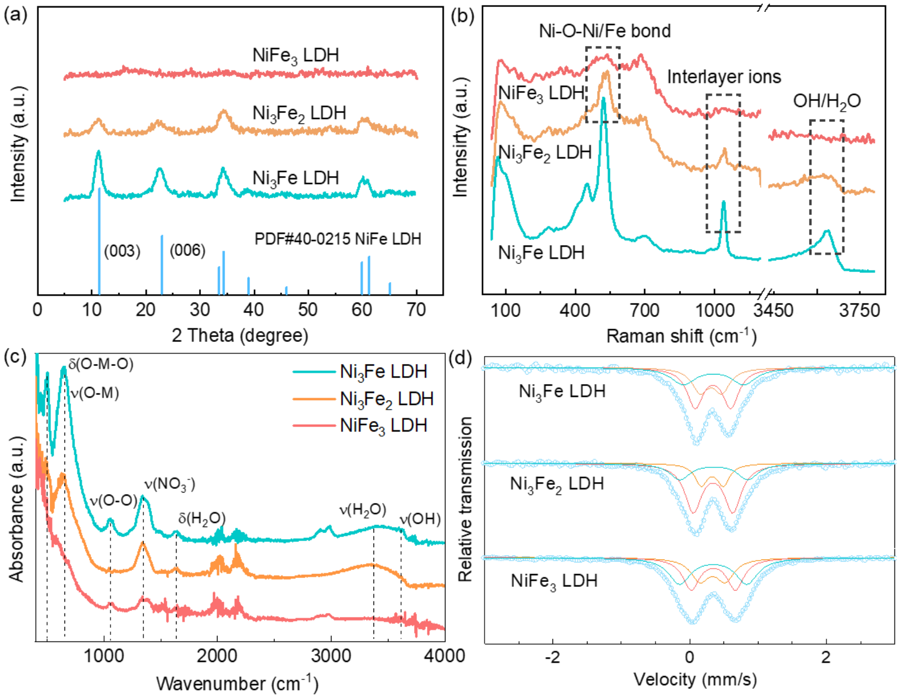

Figure 4.3 Structural characterizations of the NiFe LDH catalysts. (a) XRD patterns, (b) Raman spectra, (c) IR spectra and (d) Mossbauer spectra.

Subsequently, such kind of composition-dependent structures of these NiFe LDHs were further demonstrated by Raman spectra (**Figure 4.3**b). The Raman signal of the Ni_3Fe LDH exhibits representative bands at 447, 520 and 699 cm^{-1}, consistent with the lattice vibrations of the brucite-like LDH structure.[24,101] At higher Raman shift region, there is a sharp peak at around 1065 cm^{-1}, corresponding to the vibration of the interlayered anions of LDH structure.[167,168] The wide bands at ca. 3650 cm^{-1} are coming from the hydroxyl stretching vibrations.[169] While for the other two NiFe LDHs, decreased Raman signals in these two regions imply their distinct layered structures: multilayer Ni_3Fe LDH nanosheet could provide space for the anions, hydroxyl and/or water molecules to intercalate, while these species hardly retained for the monolayer $NiFe_3$ LDH after careful washing during the synthesis process.

For the IR spectra in **Figure 4.3**c, the bands centered at ~500 and 650 cm^{-1} are attributed to the scissoring and stretching vibrations of M-O. While the bands at 1620, 3365 and 3630 cm^{-1} are characteristic for scissoring, and stretching vibration of water and O-H groups, respectively. These gradually reduced intensities of interlayer ions, hydrogen bond and water indicate the change of layer structure of NiFe LDHs as the ratio of Fe increases. The sharp and intensive band at 1400 cm^{-1} is related to interlayer ions in LDH structures,[118,170] which we could deduce the interlayer ions: carbonate with one narrow peak at 1400 cm^{-1} while nitrate with two broader bands centered around 1400 cm^{-1}. Our data agree well with the infrared spectra of NiFe-(NO^{3-})-LDH nanosheets.[170] This is also reasonable owing to the applied precursors of nitrate salts. This data could be served as another supporting evidence of the structural changes of NiFe LDHs as composition changes. In short, the results of XRD, Raman and IR measurements are in good agreement and confirm the interaction between the composition and structure of NiFe LDHs.

We also conducted the Mössbauer spectroscopy to check the chemical environment of metal sites (**Figure 4.3**d). Traditional opinion holds that only Ni-O-Fe couples are present in NiFe LD while former work has confirmed the that the cations (Ni and Fe) are not randomly distributed across the LDH layers and display increasing Fe clustering for higher iron contents from 0.2-0.33 by Mössbauer spectroscopy.[171] Here we found the similar more than one sextet, which associates with local differences in the Fe surroundings due to the nonequivalent Fe−OH−Fe and Fe−OH−Ni interactions for all our three NiFe LDHs. Therefore, from the essence of the structure, the difference between these three NiFe LDHs is only the ratio of Fe-O-Fe to Fe-O-Ni.

As we know, the morphologies and structures of these NiFe LDH nanosheets could be directly observed by TEM images as shown in **Figure 4.4**a-c. The Ni_3Fe LDH shows stacked layers (indicated by the yellow arrows) as well as in-plane growth, while Ni_3Fe_2 and $NiFe_3$ LDHs are mostly monolayer nanosheet, despite of the same synthesis process. Moreover, the HRTEM image of Ni_3Fe LDH (**Figure 4.4**d) show the thickness of as-prepared nanosheets at 2–4 nm, corresponding to 3–6 LDH layers (0.7 nm for one layer in theory). Its magnifying HRTEM image (**Figure 4.4**e) exhibits clear lattice fringes of plane distance 1.5 Å and 2.5 Å, and the corresponding Fourier-transformed diffraction pattern (inset in **Figure 4.4**e) agrees well with the (110) and (100) planes of NiFe LDH rhombohedral structure in the <001> zone axis. These indicate the good crystallinity of the Ni_3Fe LDH sample, in contrast, the HRTEM image of $NiFe_3$ LDH show no obvious lattice fringes. Combined with the barely recognizable diffraction spots but an amorphous ring (inset in **Figure 4.4**f), these TEM results demonstrate the more disordered amorphous structure for $NiFe_3$ LDH. Such kind of structure could account for its XRD pattern, both the low crystallinity and monolayer spatial distribution lead to the disappearance of Bragg reflections. At the same time, the correlation between the composition and morphology could be summarized: as the ratio of Fe increase, well crystalline multilayer Ni_3Fe LDH will gradually tend to become monolayer amorphous $NiFe_3$ LDH.

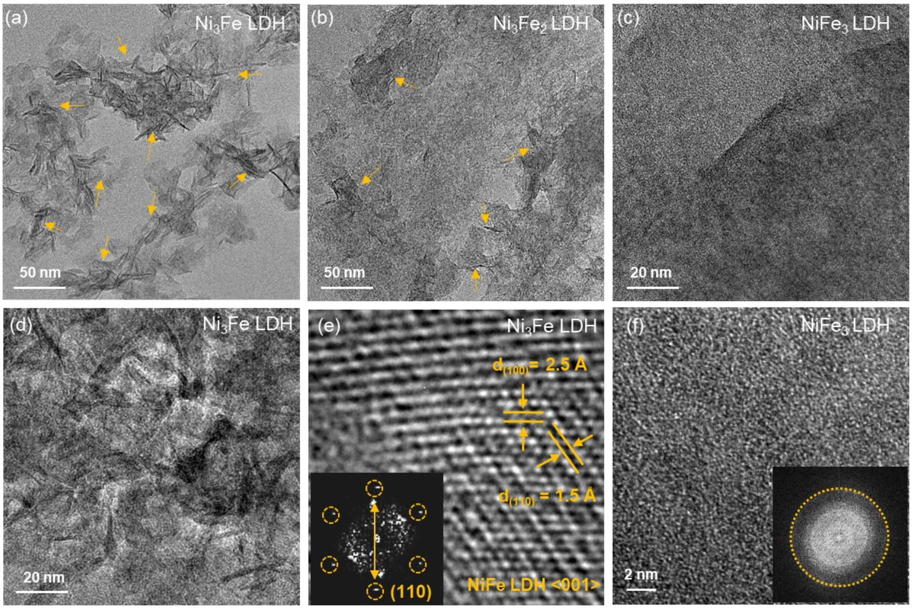

Figure 4.4 Microscopy investigation of the NiFe LDH catalysts. (a-c) TEM images of the Ni_3Fe, Ni_3Fe_2 and $NiFe_3$ LDHs (stacked LDH layers are marked by yellow arrows). (d-f) high-resolution TEM images of Ni_3Fe LDH (d-e) and $NiFe_3$ LDH (f). The insets in (e-f) show the Fourier transform of the region.

Besides of TEM images, the elemental distribution of Ni and Fe in NiFe LDH were also verified by HADDF-STEM images and corresponding EDX elemental mapping. The Ni_3Fe LDH (**Figure 4.5**a-d) confirm its stacked multilayered structure and a homogeneous distribution of Ni and Fe in the nanosheets. Meanwhile, the Ni and Fe in Ni_3Fe_2 LDH and $NiFe_3$ LDH ((**Figure 4.5**e-h and i-l) are also evenly distributed as revealed by elemental mapping. Although they are not precise to the atomic level due to the limitation of resolution, it has been proved at least that they are uniformly distributed in the nm level. Therefore, although there is a theoretical sequential precipitation of Ni/Fe, the precipitation completed in a very short time at the environment of excessive OH^- will also lead to a uniformly dispersed Ni/Fe ions in solids. This means that the composition-dependent layered structure and crystallinity changes of these NiFe LDHs are not due to the element segregation or phase separation, but other factors, such as the modulated metal sites at local chemical environments.

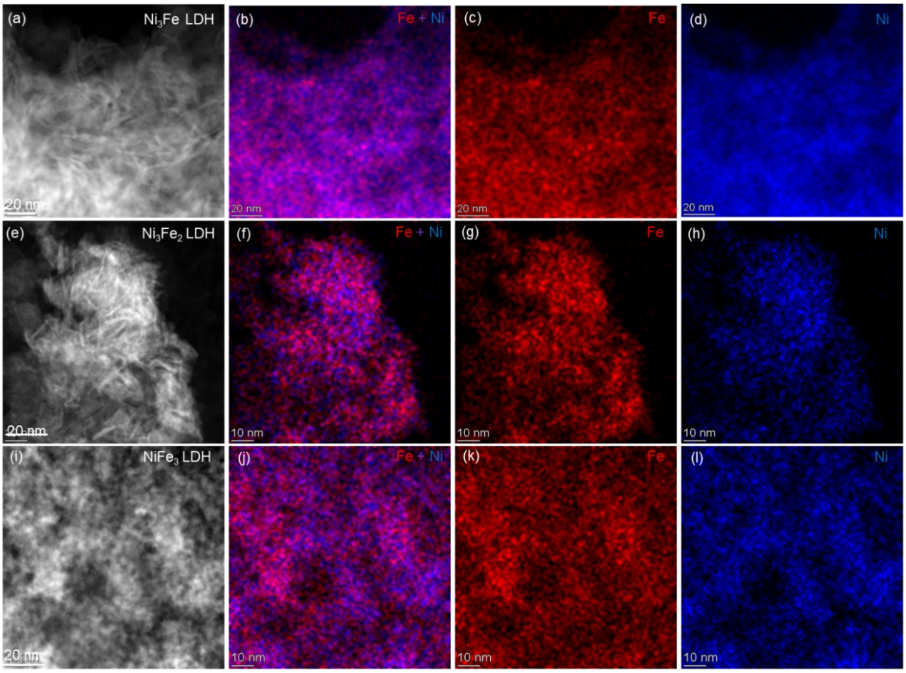

Figure 4.5 HAADF-STEM images and elemental mapping of Ni and Fe distribution in NiFe LDH nanocrystals, (a-d) Ni_3Fe_2 LDH, (e-h) Ni_3Fe_2 LDH and (i-l) $NiFe_3$ LDH.

Moreover, the corresponding surface electronic structure changes of NiFe LDHs composition were investigated by XPS spectra. The survey spectrum in **Figure 4.6**a confirms the presence of C, N, O, Ni, and Fe, with the atomic ratio (**Table 4.2**) showing a similar oxygen content, and a consistent Fe/Ni ratio trend as revealed by EDX and ICP. The core level Ni 2p spectrum (**Figure 4.6**b) of these NiFe LDHs are similar without any peak shift, and all the deconvoluted peaks are consistent with the species of Ni^{2+}.[172]

Table 4.2 Elemental ratio of NiFe LDHs from XPS profile.

Name/at%	Ni_3Fe LDH	Ni_3Fe_2 LDH	$NiFe_3$ LDH
Ni 2p3	22.7	19.3	9.3
Fe 3p	3.3	5.3	13.5

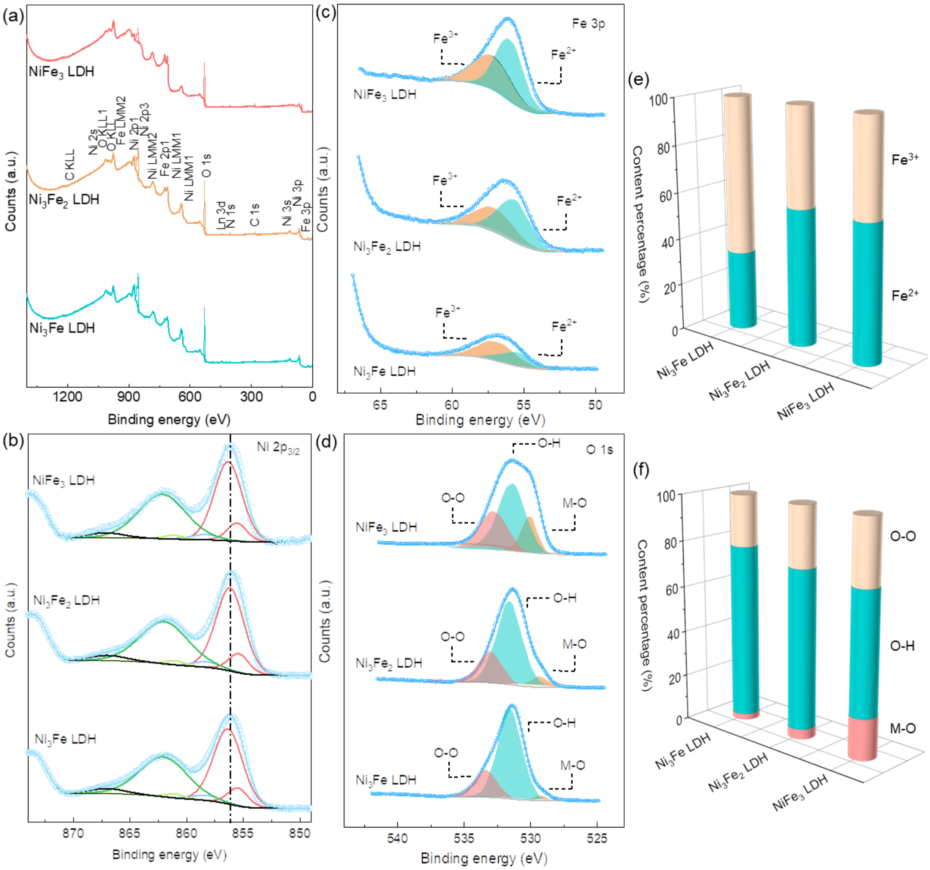

Figure 4.6 XPS spectra of NiFe LDHs. (a) survey profile, Core-level (b) Ni 2p region, (c) Fe 3p region and (d) O 1s region. (e-f) Corresponding Fe and O content from (c) and (d).

In contrast, the Fe 3p region (**Figure 4.6**c) was deconvoluted into two peaks with binding energies at 55.8 and 57.2 eV attributed to Fe^{2+} and Fe^{3+}, respectively. In our case, the Fe 3p region was investigated because it is too complicated to analyze the Fe 2p region from the high-spin configuration of Fe and Ni species.[172,173] The Fe 3p spectra for Ni_3Fe LDH exhibits a shift to higher energy by ca. 0.5 eV, compared to the peak of $NiFe_3$ LDH. This shift indicates the altered electronic structure of Fe cations, also confirmed by the fitted quantitative content of Fe^{2+} and Fe^{3+} (**Figure 4.6**e and **Table 4.3**). Compared to Ni_3Fe LDH, more Fe ions in the low valence Fe^{2+} exist for Ni_3Fe_2 LDH and $NiFe_3$ LDH. Considering the similar chemical states of Ni, there is no obvious charge transfer effect from Fe to Ni as reported in other system.[174,175] The gradually reduced oxidation state of Fe is probably due to the oxygen vacancies from coordination sites,[176,177] and the existence of Fe^{2+} in NiFe LDH from the precipitation of Fe^{3+} has also been reported in previous works.[178]

Table 4.3 Valence ratio of Fe in NiFe LDHs from XPS spectra.

Name/at%	Position (eV)	Ni_3Fe LDH	Ni_3Fe_2 LDH	$NiFe_3$ LDH
Fe^{2+}	55.8	33.7	58.1	58.6
Fe^{3+}	57.2	66.3	41.9	41.4

For the O 1s region, the different shape indicates the various content of O species. According to previous work,[116] the deconvoluted peaks at 529.0 eV, 531.2 eV, and 533.2 eV are assigned to the M-O, O-H hydroxide, and adsorbed O-O bonds in LDH, respectively. The ratio of each species (**Figure 4.6**f and **Table 4.4**) show an increased content of M-O and O-O, as well as decreased O-H bonds, as more Fe has been incorporated into NiFe LDHs. These different oxygen species imply a weakened binding strength towards the active intermediates for NiFe LDHs, which might affect the kinetic absorption/desorption process and catalytical performance under OER condition. This results also match well with the signals of interlayer OH/H_2O with different intensities for Ni_3Fe LDH and $NiFe_3$ LDH from the Raman and IR spectra in **Figure 4.3**. In summary, XPS spectra indicate that the similar Ni but distinct Fe chemical states for these NiFe LDHs.

Table 4.4 Oxygen species in NiFe LDHs from XPS spectra.

Name/at%	Position (eV)	Ni_3Fe LDH	Ni_3Fe_2 LDH	$NiFe_3$ LDH
Oxides M-O	529	2.5	4.3	17.8
Hydroxides O-H	531.3	75.2	69.3	53.5
Organic O-O	533.2	22.3	26.4	28.7

Therefore, the detailed local chemical states of Fe in the NiFe LDH samples were further confirmed by XAS. Firstly, the X-ray absorption near edge structure (XANES) spectra of Ni and Fe K-edge are compared. The Fe edge of Ni_3Fe LDH shifts to higher energy position compared to the Ni_3Fe_2 and $NiFe_3$ LDH (inset in **Figure 4.7**a), which indicate the increased chemical state from Fe^{2+} to Fe^{3+}. Similarly, the rising intensity of the white line of Fe K edge in Ni_3Fe LDH also associates with more Fe^{3+} species, with the $NiFe_3$ LDH the least intense among the three samples. Such kind of various Fe oxidation states of these NiFe LDHs, as revealed by the white line and edge shift, agrees well with the conclusion from XPS analysis. At the same time, no obvious difference in the energy position and intensity were observed for the Ni K-edge of these NiFe LDHs (**Figure 4.7**b), which means all samples contain similar Ni and also match well with their similar oxidation states from XPS spectra of Ni 2p.

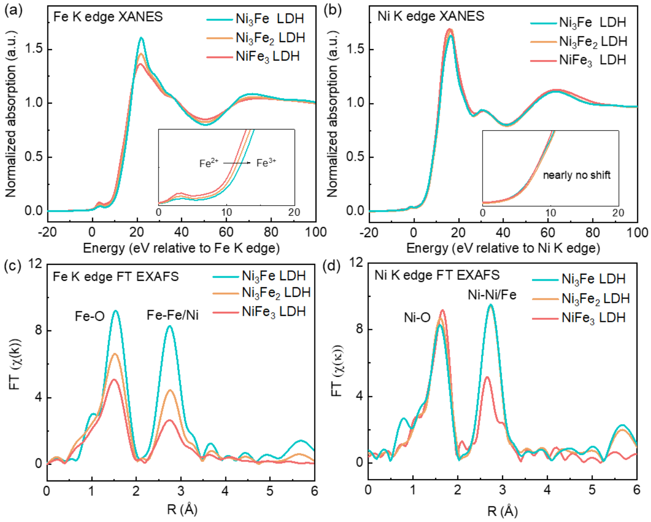

Figure 4.7 XAS spectra of the NiFe LDH catalysts. Normalized XANES spectra of (a) Fe K edge and (b) Ni K edge of NiFe LDHs. EXAFS r-space spectra of the (c) Fe K edge and (d) Ni K edge of NiFe LDHs. The r-space spectra were Fourier-transformed from Ni and Fe K-edge k^3-weighted EXAFS spectra.

The corresponding Fourier transform (FT) χ(k) of Ni and Fe K edge extended X-ray absorption fine structure (EXAFS) spectra are in **Figures 4.7**c-d with the fitted parameters shown in **Figure 4.8** and **Table 4.5**. The local chemical structure derived from the EXAFS did not exhibit significant variations for the first near bond lengths around both Ni and Fe sites (R_{Fe-O} and R_{Ni-O}) with the deviation less than 0.1 Å. While the coordination number (CN) of metal-oxygen varies for these different samples. The Ni_3Fe LDH shows the highest oxygen CN for Fe (5.4), while the CN of Fe in $NiFe_3$ LDH is the lowest (only 4.0). In other words, CN_{Fe-O} reduces with more Fe for these NiFe LDHs. The gradually unsaturated coordination leads to rich oxygen vacancies and decreased chemical states of Fe, as revealed by XPS analysis. For the Ni K-edge, CN_{Ni-O} shows less differences, which agrees with their overlapping XANES and XPS spectra.

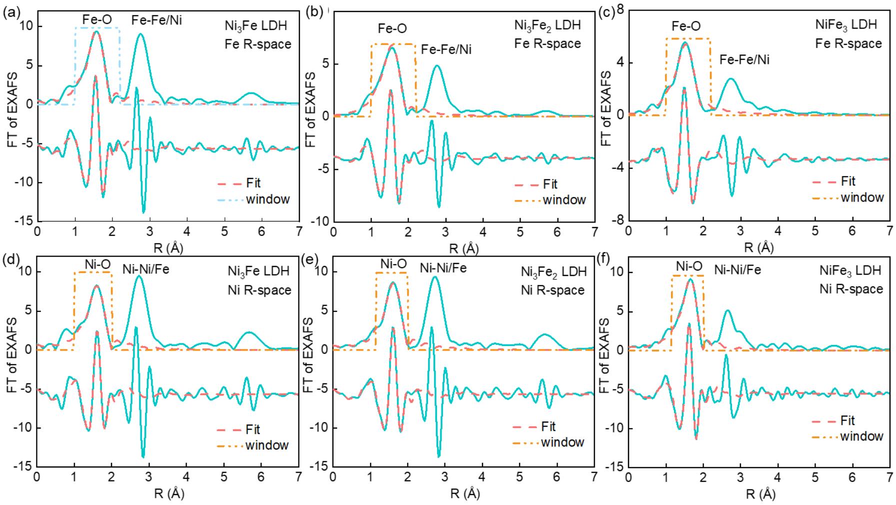

Figure 4.8 Fe K-edge (a-c) and Ni K edge (d-f) Fourier-transformed EXAFS spectra and the fitting results of NiFe LDHs. (a,d) Ni_3Fe LDH, (b,e) Ni_3Fe_2 LDH, (c,f) $NiFe_3$ LDH.

As we know, the unsaturated coordination and oxygen vacancies indicates an increased disorder level of materials. Meanwhile, the analyzed Debye-Waller factor (σ^2) can also prove the different structural disorder in these NiFe LDHs. The σ^2 values of the Fe-O shell for Ni_3Fe_2 LDH (0.0088) and $NiFe_3$ LDH (0.0101) are larger than that for Ni_3Fe LDH (0.0061) (**Table 4.5**), evidencing more distorted octahedral Fe-O structure as the composition changes. According to previous works about the formation mechanism of NiFe LDH, Fe atoms gradually substituted into the Ni host matrix.[176,179,180] The precipitation of NiFe LDH starts with the precipitate FeOOH due to the lower solubility of Fe^{3+} in OH^- rich conditions compared with that of Ni^{2+} ions. Then FeOOH diffuses into subsequently formed $Ni(OH)_2$ and substitute part of the nickel sites, leading to the NiFe LDH phase eventually. Therefore, our NiFe LDH with higher structural disorder at increasing Fe content, is also consistent with previous reports.[24,107,181]

Table 4.5 EXAFS parameters for the NiFe LDH catalysts at the Fe and Ni K edges.

Sample	Shell	CN	R[Å]	σ^2(Å^2)	S_0^2	ΔE (eV)
Ni_3Fe LDH	Fe-O	5.4(± 0.6)	2.00(± 0.01)	0.0061(± 0.001)	1	-3.1(±1.7)
	Ni-O	5.7(± 0.6)	2.05(± 0.01)	0.0070(± 0.001)	1	-0.3(±1.4)
Ni_3Fe_2 LDH	Fe-O	5.0(± 0.5)	1.99(± 0.01)	0.0088(± 0.002)	1	-1.1(±1.3)
	Ni-O	5.6(± 0.6)	2.06(± 0.01)	0.0064(± 0.001)	1	1.3(±1.5)
$NiFe_3$ LDH	Fe-O	4.0(± 0.6)	1.98(± 0.01)	0.0101(± 0.002)	1	-0.3(±1.9)
	Ni-O	5.4(± 0.5)	2.06(± 0.01)	0.0058(± 0.001)	1	1.9(±1.2)

In summary of the characterization data of XRD, Raman, IR, TEM, XPS, and XAS, we find out the compositional dependent layer structure, crystallinity, and local chemical environment of NiFe LDHs. And the inside mechanism of composition-dependent structural changes could be deduced: When more Fe ratio incorporated in NiFe LDHs, the gradually unsaturated oxygen coordination number around Fe leads to a distorted Fe-O structure, resulting in more disordered amorphous $NiFe_3$ LDH. Meanwhile, as the amount of Fe^{3+} is reduced, the interlayer hydrogen bonds weaken, which are the main contribution to connect the multilayers for LDH structure, therefore leads to a monolayer $NiFe_3$ LDH nanosheet.

4.3 Catalytical performance of NiFe LDHs

4.3.1 Half cell performance

The electrocatalytic OER performance of these three NiFe LDHs was investigated by RDE method first with experiment details explained in Chapter 2. The polarization LSV curves in **Figure 4.9**a shows a much lower onset potential and higher OER current of Ni_3Fe LDH compared with the $NiFe_3$ and Ni_3Fe_2 LDH. To avoid the overlap of Ni oxidation current at 10 mA/cm^2, the overpotentials at 50 mA/cm^2 were compared of these NiFe LDHs (inset in **Figure 4.9a**). For the Ni_3Fe LDH, the value is only 287 mV, but increased to around 350 mV for the $NiFe_3$ LDH. The corresponding Tafel slope (**Figure 4.9**b) of the Ni_3Fe LDH catalyst is 24 mV/dec, also smaller than that of Ni_2Fe_3 LDH (39 mV/dec) and $NiFe_3$ LDH (43 mV/dec). The variation of nickel redox peak during cycling process (**Figure 4.9**c) indicates a phase transition process before OER, which was checked later. Considering the possible effects of the nickel oxidation on the Tafel slope, the negative scans of all NiFe LDHs are also conducted and shown in **Figure 4.9**d. The similar values of Tafel slopes in **Figure 4.9**e agree with the results from the positive scans. The lower Tafel slope of the Ni_3Fe LDH means an easier electron transfer process for OER, thus increasing its applicability for water electrolysis.[100,102,103] The favorable kinetic is also confirmed by the lower charge transfer resistance revealed by EIS, which exhibits a smaller semicircle in the Nyquist plot for Ni_3Fe LDH than the other Ni_3Fe_2 LDH or $NiFe_3$ LDH (**Figure 4.9**f).

The stability of OER catalysts, which plays an important role in the actual application of large-scale water electrolysis, was firstly investigated by the cycling process for these NiFe LDHs. **Figure 4.9**g compared the overpotential changes at 50 mA/cm^2 during 1000 cycles between 1.0 -1.7 V. All the NiFe LDHs exhibit slightly increased overpotentials but different extents: 21±10 mV for Ni_3Fe LDH, 15±4 mV for Ni_3Fe_2 LDH, and 6±3 mV for $NiFe_3$ LDH. In other words, the less active NiFe3 LDH is the most stable among these three catalysts. Combining the above electrochemical properties, we also compared the most active Ni3Fe LDH with other NiFe LDH catalysts in the literatures. Although the experiment testing protocols are not same for all these NiFe LDH based catalysts, some are tested at higher loadings or coupled/coated with conductive substrates or 3D supports, which will enlarge their nominal OER activities, our Ni3Fe LDH is still superior than most of the reported NiFe LDH based catalysts with lower overpotential and Tafel slope, confirming its excellent instinct activity. (**Figure 4.9**h and **Table 4.6**).

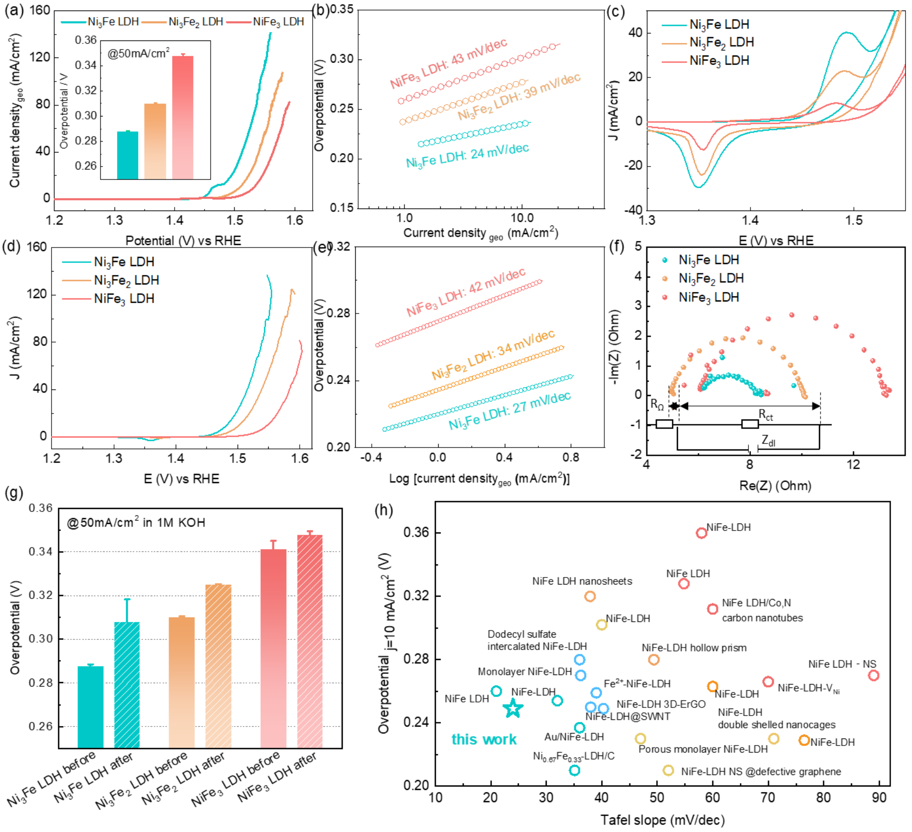

Figure 4.9 (a) Polarization curves of NiFe LDHs. (Inset: the overpotential at 50 mA/cm^2). (b) Tafel slopes. (c) the nickel redox peak. (d) Polarization curves and (e) Tafel slopes at negative scans. (f) impendence spectroscopy at 1.7 V of NiFe LDHs. (g) Overpotential changes after 1000 cycles from 1.0-1.7 Vs. (h) Summary of various NiFe LDH catalysts and corresponding OER activities by the overpotentials at 10 mA/cm^2 and Tafel slope.

Table 4.6 Comparison of the OER activity of reported NiFe LDHs in literatures.

Catalysts	Overpotential @10 mA/cm^2 in 1M KOH	Tafel slope (mV dec^{-1})	References
NiFe LDH nanosheets	~320 (0.1 M)	37.9	107
NiFe LDH	270	36.2	162
NiFe LDH	360	58	99
NiFe LDH@SWNT	250	38	
NiFe LDH /Ti mesh	263	60	113
Au/NiFe LDH /Ti mesh	237	36	
NiFe LDH	302	40	102
ultrafine monolayer NiFe LDH	254	32	109
NiFe LDH double-shelled nanocages	~230	71	163
NiFe LDH Hollow prism	280	49.4	104
porous monolayer NiFe-LDH	230	47	110
NiO/NiFe LDH	180	30	101
Ni-Fe LDH/3D-ErGO	259	39	97
Ni-Fe LDH	~390	121	98
Ni-Fe LDH/Co,N CNT	312 (0.1 M)	60	
NiFe LDH - NS	270	89	17
NiFe LDH - NS @DG10 defective graphene	210	52	
NiFe LDH	328	54.8	112
Fe^{2+} - NiFe LDH	249	40.3	
NiFe-LDH	229	76.5	106
NiFe-LDH-V_{Ni}	266	70	
NiFe LDH/C	~280	36	182
$Ni_{0.67}Fe_{0.33}$-LDH/C	210	35.1	100
Ni_3Fe LDH	**249**	**24**	**Our work**

For the stability of NiFe LDH catalysts, the duration over 1000 cycles is not sufficient to prove its durability. To investigate the further long-term stability for practical application, we also conducted the potentiostatic test of most active Ni_3Fe LDH at 1.6 V for over 400 hours. The current density exhibits slight decline, with increased overpotential at 50 mA/cm^2 and Tafel slope during this process (**Figure 4.10**). This long-time test confirms the robust durability of Ni_3Fe LDH catalyst, a potential candidate to be used in commercial devices.

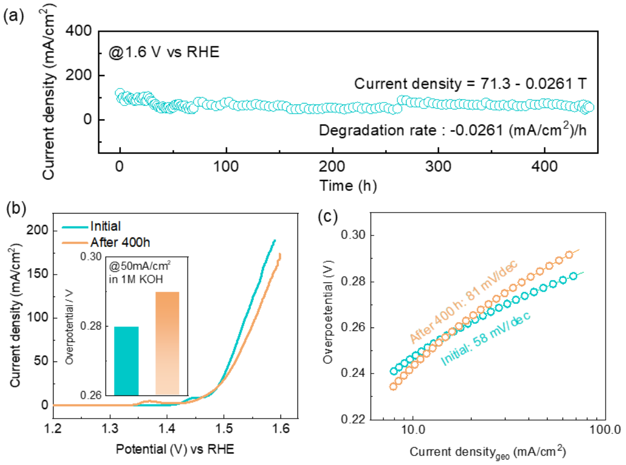

Figure 4.10 (a) Potentiostatic stability of the Ni_3Fe LDH at 1.6 V for over 400 hours. (b) Corresponding LSV curves and overpotentials (inset), (c) Tafel slope during this process.

4.3.2 Single cell performance

Based on the excellent performance of NiFe LDH catalysts on RDE, it is meaningful to verify the corresponding activity and long-term stability in a real single cell system for practical applications. The structure of water electrolyzer cell is illustrated in **Figure 4.11**a for anion exchange membrane (AEM) water electrolysis. Here, we choose the most active Ni_3Fe LDH coated on Ni fiber as anode, commercial Pt/C@ carbon paper as cathode, both manufactured with DURAION® ionomer, and DURAION® anion exchange membrane from Evonik Industries AG to fabricate the MEA. Usually, the loading of non-precious catalysts used in AEM electrolyzers are pretty high, such as 2, 3, or 4.8 mg/cm^2.[121,183,184]

So we also compared the electrolyzer cell made of Ni_3Fe LDH catalyst with the loadings of 1 mg/cm^2 and 2 mg/cm^2. The polarization curves in **Figure 4.11**b show very slightly increment of current density at higher loading, therefore, we kept this loading of Ni_3Fe LDH at 2 mg/cm^2 as default value for other measurements.

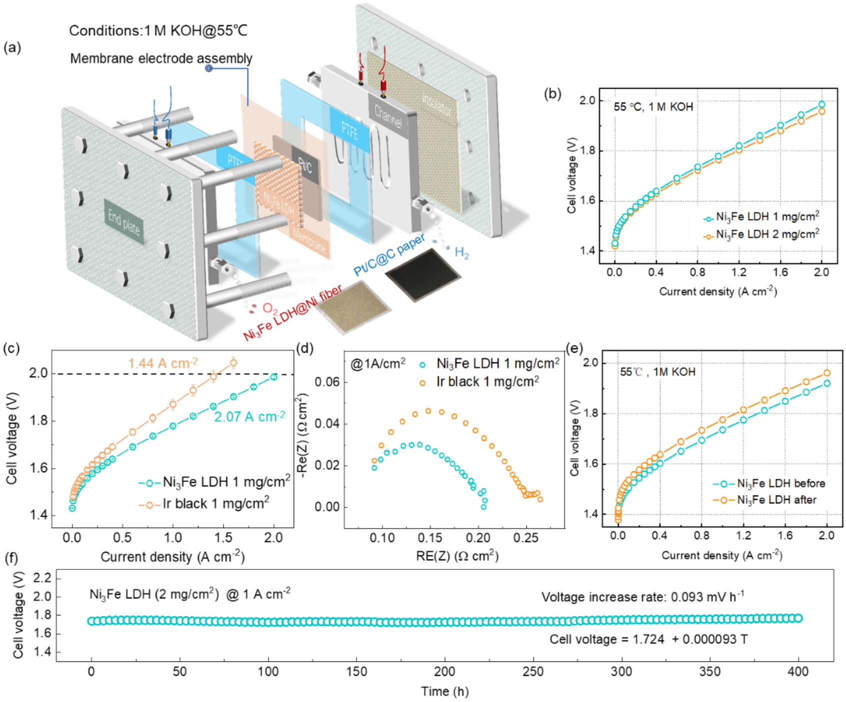

Figure 4.11 Single cell performance of Ni_3Fe LDH catalyst. (a) Schematic illustration of the electrolyzer cell. (b) Polarization curve of the cells using Ni_3Fe LDH catalysts as anode with loadings of 1 and 2 mg/cm^2. (c) Polarization curve of the cell based on Ni_3Fe LDH@Ni fiber electrode with commercial Ir black @ Ni fiber electrode as an anode, respectively. (d) (e) Polarization curve and (f) galvanostatic curve of water electrolysis using 2 mg/cm^2 Ni_3Fe LDH catalysts as anode before and after the 400 h at 1 A/cm^2.

To evaluate the single cell performance of Ni_3Fe LDH, its polarization curve of the cell fabricated by Ni_3Fe LDH catalysts is compared with the benchmark cell based on Ir black (at the same loading of 1 mg/cm^2) as an anode in **Figure 4.11**c. The Ni_3Fe LDH cell exhibits a superior activity: the current density of 2.07 A/cm^2

was reached at 2.0 V, in contrast, the current density of the Ir-based cell at 2.0 V is only 1.44 A/cm^2. This performance is also dominant even compared with other non-precious AEM electrolyzers tested under the similar conditions (**Table 4.7**).[185–191] Several latest works have reported performance breakthroughs of AEM with non-noble-metal catalysts: the electrolyzer with NiFeCo cathode and NiFeO$_x$ anode reached 1 A/cm^2 at 1.90 V in 1 M KOH at 60°C,[122] while an novel Fe-NiMo-NH$_3$/H$_2$||NiMo-NH$_3$/H$_2$ cell had a voltage only at 1.57 V for 1 A/cm^2 at 80 °C.[123] The most efficient electrolyzer, using nanometer-sized NiFe-LDH as anode, Pt/C as cathode, delivers 1 A/cm^2 low at 1.59 V at 80 °C in 1 M KOH.[124] For our Ni$_3$Fe LDH catalyst, the common current density of 1 A/cm^2 was achieved at 1.745 V, a little higher than reported values but at lower temperature 55°C. Moreover, these non-noble metal catalysts are obtained in a relatively complex process, either at high temperature (550 °C)[123], or long time (a few days) with the addition of organic solvents.[124] These will limit its practical applicability considering the scaling and economic costs of catalysts. While our NiFe LDHs, synthesized at room temperature and less than an hour with large scale yield, exhibits comparable single-cell energy efficiency. It meets both the requirements of high performance (efficiency) and low cost (practicality) for the application of catalysts in AEM electrolyzers.

Table 4.7 Comparison of the activity of alkaline water electrolyzers

Catalysts Anodic || cathodic	Ionomer	Membrane (thickness/μm)	Electrolyte	Temperature /℃	Activity @2V mA/cm^2	Reference
IrO_2 || Pt/C	-	FAA-3-50	1 M KOH	60	620	[192]
g-CN CNF-800 || Pt/C	-	FAA-3-50	1 M KOH	60	980	[192]
Pt/C || Pt/C	Polyarylimi-dazoliums	FAA-3-25	1 M KOH	60	20@ 2.2 V	[187]
IrO_2 || Pt/C	FAA3-Br	FAA-3-50	1 M KOH	50	1420	[193]
$NiMn_2O4/C$ || Pt/C	FAA-3	FAA-3-50	1 M KOH	50	380	[121]
Ni_3Fe LDH || Pt/C	**DURAION®**	**DURAION®**	**1M KOH**	**55**	**2067**	**Our work**

The faradaic efficiency and energy conversion efficiency of this water electrolyzer were measured and calculated by reported methods.[123,124,194,195] The testing setup is shown in **Figure 4.12**a, the current density is fixed at 1 A/cm^2 with the temperature 55 °C and flow 1M KOH electrolyte. The produced O_2 and H_2 gas over a certain time from the electrolyzer were quantified by water–gas displacement method then compared with theoretical volume for the faradaic efficiency (**Figure 4.12**b). The experimentally collected O_2 agrees well with the theoretical values, with the faradaic efficiency of 97.8%, indicating the high utilization rate of energy. The corresponding energy conversion efficiency of this cell is 69.7% at 1 A/cm^2, comparable to other reported MEAs even the temperature of our cell was relatively low at 55 °C.[124,194]

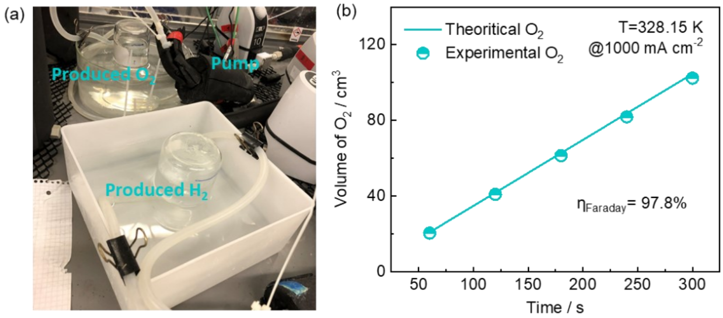

Figure 4.12 (a) Demonstration of the setup to collect the produced O_2 and H_2 calculate the faradaic efficiency (b) The comparison of theoretical and experimental hydrogen volume to calculate the Faradaic efficiency.

The stability of the cell was evaluated under galvanostatic conditions kept at 1 A/cm^2 for 400 h. The recorded cell voltage over this period in **Figure 4.11**f is relatively stable despite some random fluctuations due to the evolved bubbles at the electrode surface. The increment rate of cell voltage is lower than 0.1 mV/h, indicating the robust stability of this MEA prepared by our Ni_3Fe LDH catalyst as anode. It leads the improved trend than most reported NiFe-based single cells which only presents short-term stabilities for several hours to a few days.[123,124,196–198] Therefore, all these single cell tests confirm NiFe LDH is a greatly promising candidate for the next generation non-noble catalysts with high efficiency and durability for practical AEM water electrolyzers.

4.4 Correlation of structure and OER property of NiFe LDHs

4.4.1 Electronic structure and active intermediates for activity

For the distinct OER performance of NiFe LDHs, we would like to figure out the inside reason. According to former characterization, their morphologies, spatial and electronic structures are different, which will affect both the surface area and intrinsic activity. First, the electrochemical surface area (ECSA) of the three NiFe LDHs catalysts was compared by the double-layer capacitance (C_{dl}),[199] which was regarded as positive relationship with ECSA and gained from the linear slope of currents vs scan rates (**Figure 4.13**). The ECSA of most active Ni_3Fe LDH is smaller than the CD other two NiFe LDHs, owing to the different structure/crystallinity, as the amorphous structure exposes more active sites than crystalline samples. It also evidences the superior activity of Ni_3Fe LDH does not result from a larger ECSA, but rather its higher intrinsic catalytical property.

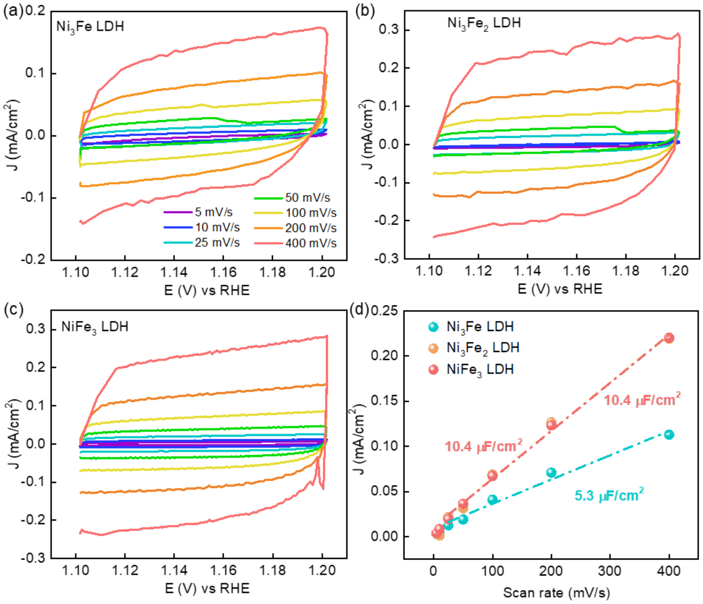

Figure 4.13 Double-layer capacitance measurements for determining electrochemically active surface area for NiFe LDHs from voltammetry in 1 M KOH. (a-c) Cyclic voltammograms of Ni_3Fe LDH, Ni_3Fe_2 LDH and $NiFe_3$ LDH were measured in a non-Faradaic region of the voltammogram at the following scan rates: 5, 10, 25, 50, 100, 200, 400 mV/s. (d)The specific capacitance of NiFe LDHs calculated by the slope of the linear fits from the current densities at various scan rates.

Therefore, the correlation between electronic structure and OER activity of these NiFe LDHs should be considered. As the elemental ratio of Ni/Fe is modified, the metal ions in NiFe LDHs are modulated with each other due to the charge transfer effect. This modulation of the metal sites will affect the adsorption energy of the reactants, the formation energy of the active intermediates, and the overall OER performance.[174,200] Recent researches have proposed that the high-valent metal species in NiFe-based catalysts are the main OER active site.[34–36,201] For our catalysts, we have proved the CD distinct chemical states of Fe compared to similar Ni sites in the three NiFe LDHs by XPS and XAS, indicating the irreplaceable role of Fe for OER process. The higher fraction of Fe^{3+} species in Ni_3Fe LDH are also responsible for its superior activity than the $NiFe_3$ LDH catalyst. Besides of the general valence, the local chemical environment of Fe for these samples are also different. It has been proved that the disorder level of NiFe LDHs would affect the lattice order of NiOOH, the active intermediate of NiFe oxyhydroxides at OER potentials.[29,34,35].The Ni_3Fe LDH presents more ordered structure with better crystallinity and higher oxygen coordination number. It is conceivable that the optimized chemical environment of the Fe sites in NiFe LDH correlate to an optimal disorder level of the active intermediate, which could be verified by advanced in-situ techniques at OER condition.

The real active species and dynamic phase transformation on the surface of NiFe LDH was investigated by in-situ Raman with the applied potential between 1.3 to 1.7 V, similar as the cycling process (**Figure 4.14**). For Ni_3Fe LDH, the invariable Raman band at 520 cm^{-1} in the potential from 1.3 to 1.5 V, indicates its unchanged LDH structure (**Figure 4.14**a), while a sharp band at 1060 cm^{-1} exists owing to the absorption of OH^- intermediate layers of LDHs at elevated potentials.[168,202] When the potential increases to 1.6 V, the two bands at 477 and 557 cm^{-1} match well with the Raman spectral features of γ-NiOOH, which acts as the real active intermediate favorable for excellent OER reactivity.[202–204] Meanwhile, the Raman band at 1060 cm^{-1} disappears at 1.6-1.7 V, indicating the deprotonation of the hydroxyls to form active oxygen species $NiOO^-$ under OER conditions.[117,204]. In contrast, this characteristics changes did not exist for $NiFe_3$ LDH (**Figure 4.14** c), indicating unfavorable bonding energy and intermediates for reaction due to the modulated electronic structure at higher Fe content. The retained intermediate species from the rate-limiting step of OER also confirms the sluggish dynamics of less active NiFe$_3$ LDH catalyst.

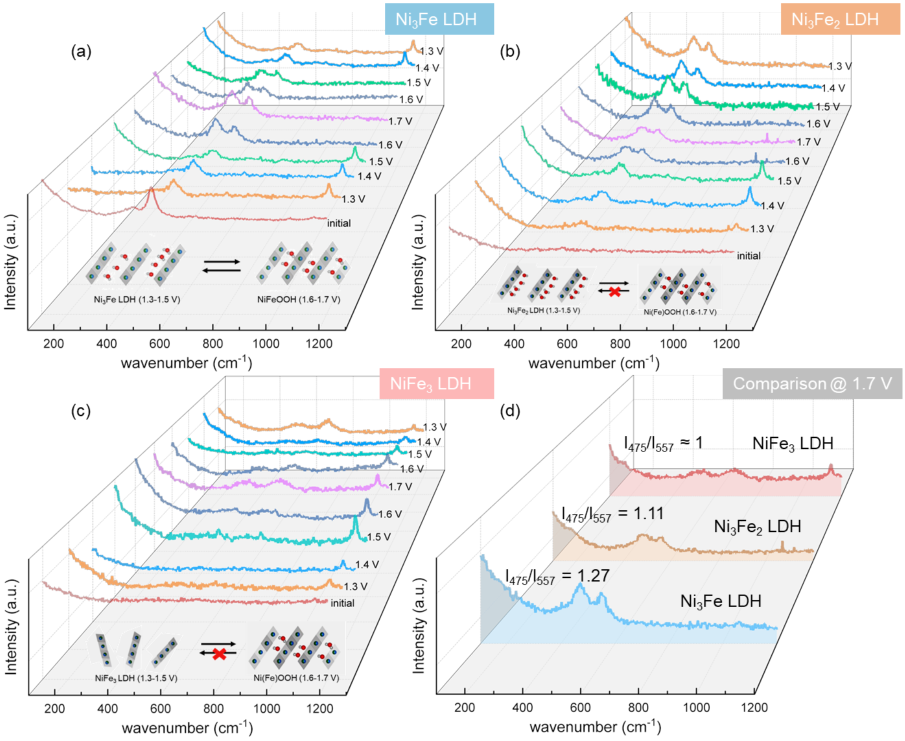

Figure 4.14 In-situ Raman spectra of the NiFe LDH catalysts. Spectra were obtained after keeping initial sample at different potentials in sequence: 1.3 V, 1.4 V, 1.5 V, 1,6 V, 1.7 V, 1.6 V, 1.5 V, 1.4 V, 1.3 V. (a) Ni$_3$Fe LDH, (b) Ni$_3$Fe$_2$ LDH and (c) NiFe$_3$ LDH. (d) Comparison of the Raman band for NiFe LDHs at high potential 1.7 V and the corresponding value of the I_{475}/I_{557} band ratio.

At the same time, we could also compare the active species at OER potential for these NiFe LDHs as the band intensities at 477 and 557 cm^{-1} at highest potential 1.7 V vary (**Figure 4.14**d). For quantitative comparison, the rate of absolute band intensity (I_{475}/I_{557}) is regarded as an objective value, dependent on the disorder level.[205] With increased Fe content of NiFe LDHs, the band intensity at 475 cm^{-1} decreases faster than the one at 557 cm^{-1}, lead to a gradually decreased value of I_{475}/I_{557} band ratio. It comes from the more atomic disorder probably introduced by excess incorporated iron atoms, and this trend agrees well with the initial order-level of NiFe LDHs revealed by TEM and XAS. The band ratio (=1.27) of the intermediate for Ni_3Fe LDH is in the reported optimal interval, while the counterpart (I_{475}/I_{557} = 1) for further increased Fe content in $NiFe_3$ LDH could be unfavorable for OER activity.[181]

In summary, it is the modified electronic structures, rather than ECSA, that account for the distinct OER activity of these NiFe LDHs. And the initial disorder level local chemical environment will affect the structure of real active intermediate under OER condition, which could act as a more accurate descriptor for OER reactivity.

4.4.2 Iron dissolution and degradation mechanism for stability

The cycling stability of these NiFe LDHs, which were verified in **Figure 4.9**g, show a degradation trend of Ni_3Fe LDH, Ni_3Fe_2 LDH and $NiFe_3$ LDH, contrary to the trend of their activities. The Ni_3Fe LDH presents the most obvious degradation, therefore, we conducted SEM observation and ICP analysis of Ni_3Fe LDH after cycling process and long-term tests to figure out the degradation mechanism. The SEM images (**Figure 4.15**) confirmed the more porous morphology of the catalysts remaining on the nickel foam substrate probably due to the phase transition during electrochemical process. The pristine relatively flat surface layer gradually transformed into loose and uneven surface. Such kind of structural changes were verified by XPS in **Figure 4.16**, the increased O/Ni ratio indicates the oxidation of catalysts, and the shifted Ni 2p peak towards higher energy and more OH content in oxygen species also confirm that. These results are consistent with the robust stability of Ni_3Fe LDH catalysts.

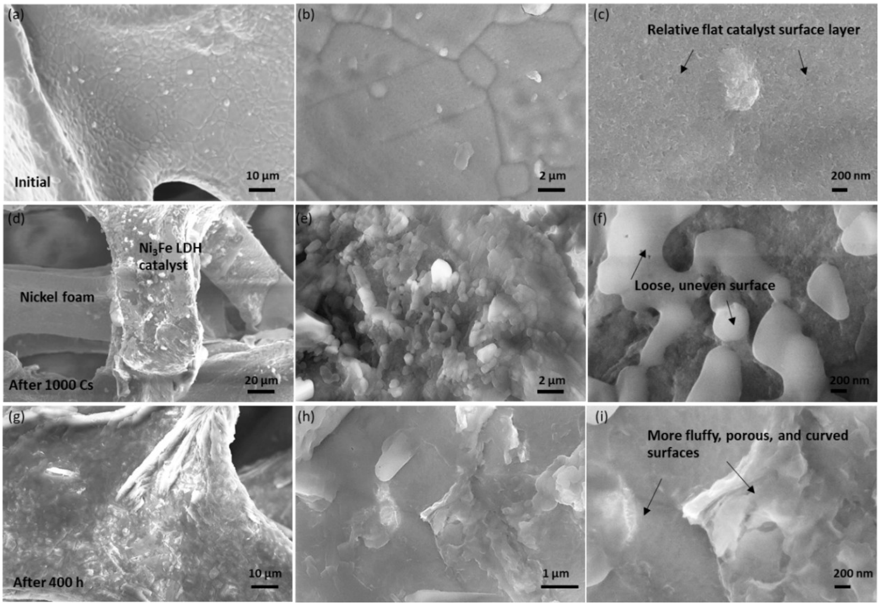

Figure 4.15 SEM image of Ni_3Fe LDH catalysts after stability tests. (a-c) initial sample, (d-f) after 1000 cycles between 1.0-1.7 V and (g-i) keeping at 1.6 V for over 400 hours in 1M KOH. The Ni_3Fe LDH are drop-casted on nickel foam with the loading of 0.2 mg/cm^2.

Therefore, more accurate investigations on the possible dissolution of NiFe LDHs were carried out by ICP-MS test of the electrolytes (1M KOH) during the stability test under different conditions (**Figure 4.16**d and **Table 4.8**). The sample 1M KOH electrolyte after rinsing the NiFe LDH electrode as same time for 1000 cycles shows no metal dissolved during this procedure, enable the reliability of this method. For the Ni_3Fe LDH, the increased Ni and Fe ions in the electrolytes indicates slight metal dissolution of Ni and Fe during the stability test, therefore, a dissolution ratio of 1.5% Ni and 5% Fe compared with pristine sample could be calculated. In contrast, the Ni_3Fe_2 LDH and $NiFe_3$ LDH exhibit lower metal dissolution, 2.8% an 2.3% respectively, which agree and explain their stability trend. At the same time, it is obvious to see that Fe dissolution is more severe than Ni, around 3 times higher, such different kinds of dissolution behaviors could be explained by their nature stable structure as revealed by Pourbiax diagram at various potential and pH conditions.

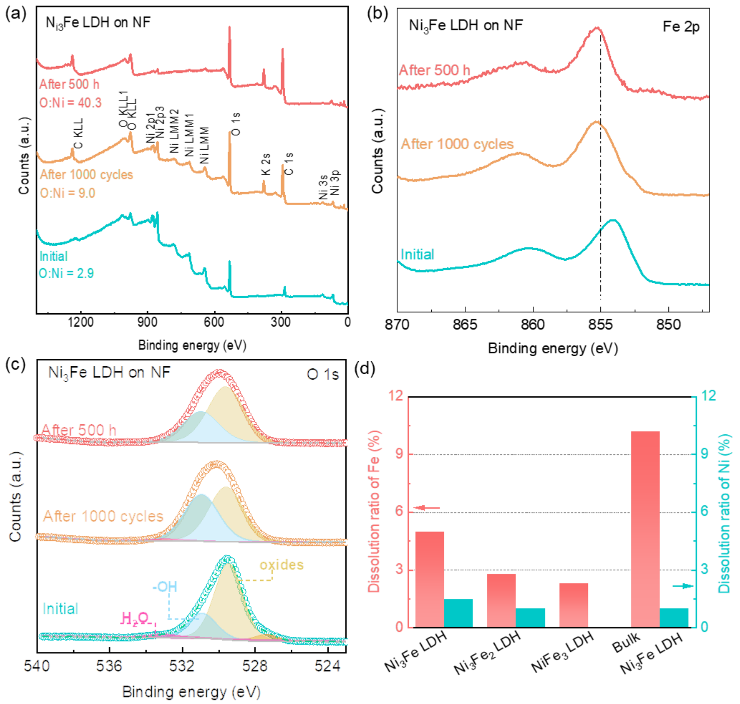

Figure 4.16 XPS data of Ni_3Fe LDH with initial sample, after 1000 cycles of 1.0-1.7 V, and kept at 1.6 V for over 400 hours in 1M KOH. (a) survey spectrum, (b) Ni 2p and (c) O 2p. The Ni_3Fe LDH are drop-casted on nickel foam with the loading of 0.2 mg/cm^2. (d) Metal dissolution of Fe/Ni during the cycling process revealed by ICP-MS.

Table 4.8 ICP-MS of metal ions (Fe/Ni) in electrolytes and the deduced metal dissolution

Sample	Description	Change of Fe		Change of Ni		Dissolved ratio	
		MW (μg/L)	SD (μg/L)	MW (μg/L)	SD (μg/L)	Fe (%)	Ni (%)
1M KOH	Rinsed in KOH	-1	2	-4	4	0	0
1M KOH	After 1000 Cs of Ni_3Fe LDH	+7	3	+6	8	5.0	1.5
1M KOH	After 1000 Cs of Ni_3Fe_2 LDH	+5	3	+2.8	0.7	2.8	1
1M KOH	After 1000 Cs of $NiFe_3$ LDH	+12	2	0	0.7	2.3	0
1M KOH	After 1000 Cs of bulk Ni_3Fe LDH	+13.6	1.7	+4.6	1.3	10.2	1

According to current work about the OER stability of NiFe LDHs, layer structure is found to have obvious negative effect: the stacked layers are harmful to the ion diffusion process then lead to a local acid condition and catalyst dissolution.[118] Therefore, to clarify the possible influence of layer structure and elemental composition, we firstly distinguish these two factors by comparing the OER stability of NiFe LDHs with same composition but different layer structure. Besides of obtained exfoliated Ni_3Fe LDH, an additional bulk Ni_3Fe LDH was controlled by excluding the exfoliation process. Its structure was confirmed by TEM images in **Figure 4.17**a-f, compared with exfoliated samples, bulk LDH shows more obvious nanosheets morphology, increased crystallinity and clearer lattice fringes as well as similar homogeneous distribution of Ni and Fe. The XRD pattern in **Figure 4.17**g presents stronger peak intensity, confirming the increased layer structure and crystallinity while the atomic ratio of Ni/Fe revealed by EDX and ICP is 74.9: 25.1 and 77.9: 22 (%), almost same as exfoliated Ni_3Fe LDH. That is, these two NiFe LDH are same composition but different layer structure. Then their corresponding OER stability has been compared by the overpotentials during the 1000 cycling process in **Figure 4.17**h. The less current degradation and more stable overpotential at 50 mA/cm^2 verifies the negative effect of layer structure on OER stability. The ICP-MS test of electrolyte confirm that the bulk Ni_3Fe LDH occurs more Fe dissolution than exfoliated Ni_3Fe LDH (**Figure 4.16** and **Table 4.8**), which account for the consistent degradation during the cycling process. These experiments prove the influence of the layer structure of LDHs on OER stability as illustrated in **Figure 4.17**i: bulk LDH show more dissolution and degradation than exfoliated LDH.

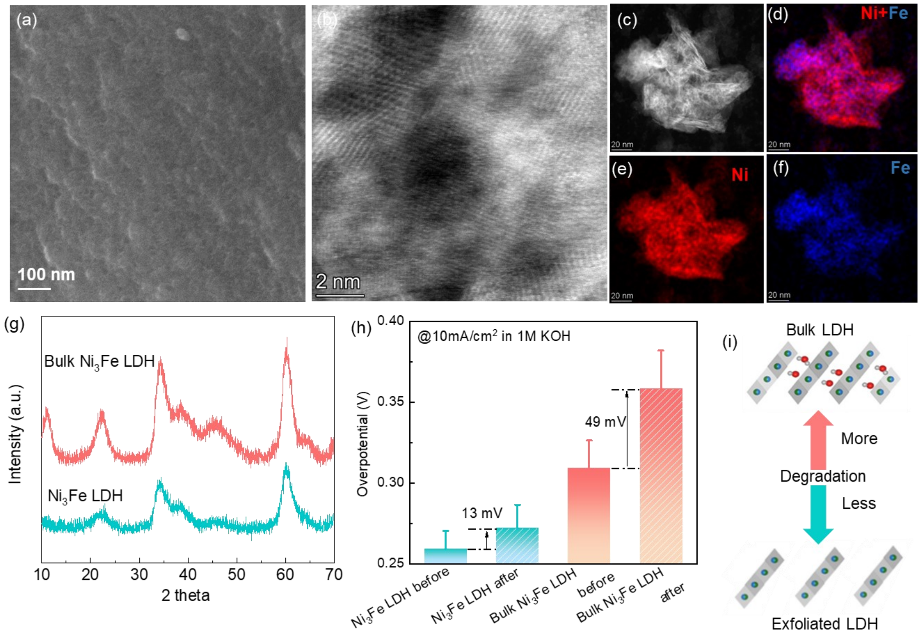

Figure 4.17 (a-f) Electron microscopy of bulk Ni_3Fe LDH. (a) SEM image, (b) STEM image, (c-f) STEM EDX mapping of Ni and Fe distribution. (g) XRD comparison of exfoliated Ni_3Fe LDH and bulk Ni_3Fe LDH. (h) the overpotential at 10 mA/cm^2 of Ni_3Fe LDH and bulk Ni_3Fe LDH during 1000 cycles between 1.0-1.7 V in 1M KOH. (i) the illustration of the correlation from the layer structure of LDH with its degradation degree.

While from in situ Raman spectra in **Figure 4.14**, the cycling process leads to different phase transition process, which will affect the degradation and dissolution behavior. As we discussed before, all the NiFe LDH have been transited into Ni(Fe)OOH at high potential and the disorder levels at 1.7 V are distinct dependent on the Fe content. When the potential returns from 1.7 V to 1.3 V, the signals of NiOOH species gradually disappear and the Raman bands of LDH phase reappear for Ni_3Fe LDH, consistent with the reduction peak of NiOOH to $Ni(OH)_2$ in the CV curves. In other words, this in-situ Raman spectra confirm a reversible structure transformation process between Ni_3Fe LDH and Ni (Fe)OOH during the potential cycling process. In contrast, the Raman signals of Ni_3Fe_2 LDH and $NiFe_3$ LDH after going back to 1.3 V are distinct from the initial signals, demonstrating an irreversible phase transition during the same cycling period. In theory, these different phase transition trends could affect the OER stability, reversible catalysts should be more stable than irreversible ones while their actual cycling stability is converse.

Their different stability performance could be related to the pristine atomic and electronic structure of NiFe LDHs: well-crystalline and ordered Ni_3Fe LDH with more coordinated oxygen atoms are, therefore, stable for the phase transition process, only exhibiting slight degradation during the nickel redox region. However, the $NiFe_3$ LDH with a lower order degree possess probably poor structural stability, and cannot transit back from the intermediate phase formed at high potential anymore, leading to a corresponding irreversible dynamic process and more metal dissolution at this period. This is the main degradation mechanism called transition dissolution from surface reconstruction process, consistent with former report in noble metal OER catalysts.[206]

To investigate the specific dissolution potential and degradation mechanism, the stability of Ni_3Fe LDH and $NiFe_3$ LDH after extended 5000 cycles were compared in three sequential potential ranges as shown in **Figure 4.18**a: capacitance range of 1.0-1.3 V, nickel redox range of 1.3-1.5 V, and OER range of 1.5-1.7 V. The significantly decreased current density and increased overpotential for Ni_3Fe LDH indicates its main degradation range is the OER process, which is similar to the aforementioned steady-state dissolution reported for other OER catalysts.[207,208] In contrast, the $NiFe_3$ LDH shows only some degradation when cycled in the nickel redox region, which is referred to as transient dissolution, possibly due to the surface reconstruction process. These different degradation regions and dissolution behavior agree well with the in-situ Raman spectra.

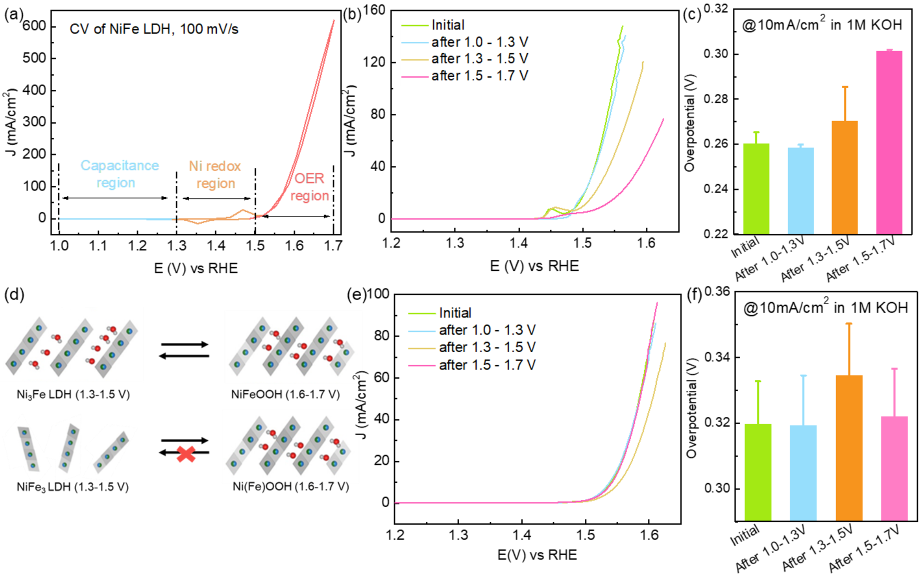

Figure 4.18 (a) CV curve of NiFe LDH between 1.0-1.7 V and the rough range for three separate regions: 1.0-1.3 V, capacitance region; 1.3-1.5 V, nickel redox region;1.5-1.7 V, OER region. (b) LSV curves of Ni_3Fe LDH after cycling over these ranges for 5000 cycles and (c) corresponding overpotentials. (d) illustration of the phase transition process of NiFe LDHs during cycling process. (e) LSV curves of $NiFe_3$ LDH after cycling over these ranges for 5000 cycles and (f) corresponding overpotentials.

4.5 Chapter summary

In summary, a series of NiFe LDHs with compositional-dependent morphology, atomic and electronic structure were prepared by a facile precipitation method. The correlation between the composition and structure of NiFe LDHs was investigated by XPS, TEM, and XAS: the more Fe is incorporated into LDHs, the less stacked layer structure, the lower crystallinity, the lower proportion of Fe^{3+} and number of coordinated oxygen atoms of these NiFe LDHs will be.

Surely these structure changes results in their different OER performance. The multilayer Ni_3Fe LDH exhibit higher OER activity than monolayer $NiFe_3$ LDH on RDE. It also outperforms most reported NiFe LDHs from half cell and single cell measurements. The single cell utilized Ni_3Fe LDH as anode catalysts for alkaline exchange membrane water electrolysis exhibits superior current density compared to its Ir-based counterpart cell, as well as a robust long-term stability at 1 A/cm^2 for at least 400 h.

In-situ Raman shows that the intermediate Ni(Fe)OOH phase is the actual active species of all NiFe LDHs at the OER potential, which also account for their different performance when we compare the disorder level of these species from Raman spectra. These trends are similar as their pristine local chemical environment revealed by TEM and XAS. At the same time, the more disordered Ni_3Fe_2 and $NiFe_3$ LDHs show an irreversible phase transition during the potential cycling process, while the more ordered Ni_3Fe LDHs is able to return to the initial stage with good crystallinity. Combined with ICP-MS and electrochemical tests, we found out their different dissolution behaviors: Ni_3Fe LDH presents steady-state dissolution at OER process, and $NiFe_3$ LDH is associated with transient dissolution due to the surface reconstruction process.

Our work in this chapter characterizes the detailed analysis of the catalyst structures, including morphology, layer structure, element valence, local coordination environment, and catalytical performance of NiFe LDHs. The found excellent activity and stability of Ni_3Fe LDH on RDE and single cell make this catalyst a promising non-precious metal-based candidate for actual application in alkaline water electrolyzers. Moreover, it provides insights into the relationship between the composition, electronic structure of the layer, and electrocatalytic performance, and offers a scalable and efficient strategy for developing more stable catalysts to support the development of the future hydrogen economy.

Chapter 5 Optimization of the structure and OER property of NiFe LDH catalysts

5.1 Introduction part

Based on the results from last chapter, the correlation between structure and OER performance of NiFe LDHs were investigated and found that Ni_3Fe LDH exhibits the best activity while $NiFe_3$ LDH is most stable. Therefore, it is necessary to further optimize the structure of NiFe LDHs, to enhance the catalytical performance and get both active and durable catalyst for alkaline water electrolyzer. As summarized in Chapter 1, various reported strategies have been applied to boost the OER activity of NiFe LDH, but rarely approaches are reported to improve the stability. We have found the layer structure of NiFe LDH really affects the metal dissolution and degradation process; therefore, the emphasis will be modulation of the layer structure while the composition of Ni/Fe, which dominate the activity, are kept constant in this part.

Here, we adopted several different strategies to tune the structure, for instance, introduction of certain content polar solvent formamide into the initial water solvent in the synthesis process to exfoliate the multilayers of LDH to get Ni_3Fe LDH-F samples; heat treatment of initial Ni_3Fe LDH powders; incorporation of MnO_4^- ion into the layers to enlarge the layer spacing of Ni_3Fe LDH and hydrothermal treatment to increase the crystallinity of Ni_3Fe LDH.

5.2 Introduction of polar formamide

According to former works, formamide is kind of polar solvent, which will assist the exfoliation of LDH instantly and spontaneously at room temperature as the delaminating agent.[209] Therefore, exfoliation of LDHs into monolayer structure in formamide is regarded as an excellent idea to enhance the catalytical performance of NiFe LDHs. Here, different contents of formamide were added into the former water solvent to synthesize Ni$_3$Fe LDH, so named as Ni$_3$Fe LDH-F (0, 25, 50, 75, refers the ratio of formamide in the mixed solvent). The synthesis process is illustrated in **Figure 5.1**a.

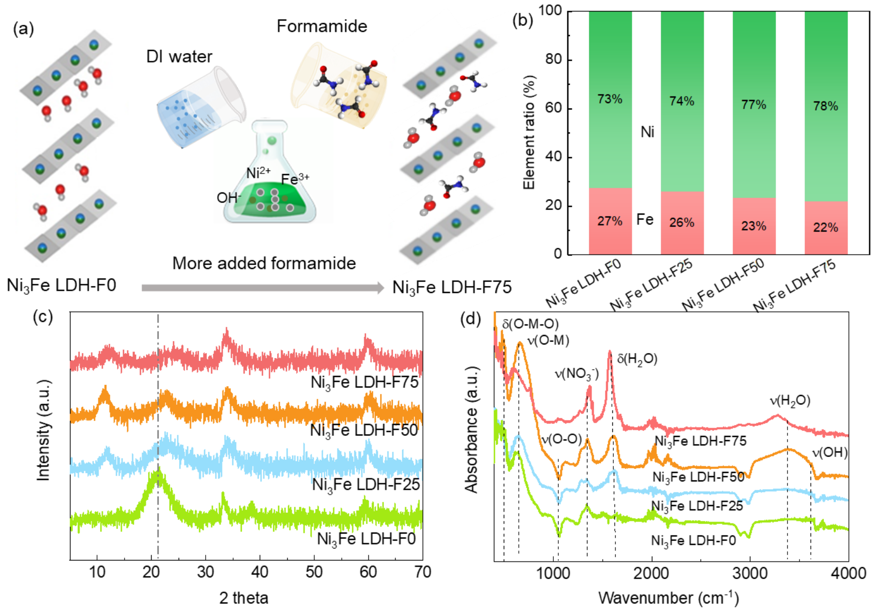

Figure 5.1 (a) Illustration of the synthesis process of NiFe LDH with formamide. (b) elemental ratio of Ni/Fe in the NiFe LDH-F samples. (c) XRD and (d) IR spectra of NiFe LDH-F samples.

First, we checked their elemental composition of these samples by ICP-OES in **Figure 5.1**b and the ratio of Ni/Fe were close to each other, even for the initial and most formamide Ni$_3$Fe LDH-F75 samples. The ignorable slightly gradual increment of Ni might from the modulation effect of formamide. Therefore, it is reasonable to regard all samples as same composition and simply as Ni$_3$Fe LDH. Then their crystal structures were investigated by XRD patterns, as shown in **Figure 5.1**c, all the peaks are consistent well with NiFe LDH structure, indicating the unchanged crystal structure. While the gradually shifted and reduced peak at 24 °, attributed to the (006) planes of LDH structure, implying the changes of layer structures. The reduced peak means the less stacked layer while the shift to higher angle structure indicates the deceased layer spacing as more formamide involves. The IR spectra were also collected to check the structure changes of NiFe LDH with the assisting of formamide. In general, all the spectra show similar peaks as pristine NiFe LDH-F0, indicating similar NiFe LDH structures. While the gradually increasing characteristic peak of NiFe LDH-F75 at the 1690 cm^{-1} of C=O vibration of formamide[210], confirming the incorporation of formamide into layers, this could be the reason why the NiFe LDH show the most obvious structure change in XRD pattern.

Their electronic structures were revealed by XPS in **Figure 5.2**. The Ni 2p region shows a slight shift to higher energy for Ni_3Fe LDH-F compared with initial Ni_3Fe LDH, indicating similar chemical states of Ni. For the Fe 3p region, there is a red shift of F0 and F50 samples, indicating higher valence. The specific Fe species show that F0 and F50 possess higher ratio of Fe^{3+}, while F25 and F75 contain lower Fe^{3+}. Our former work of NiFe LDH with different composition has proved the importance of Fe at high valence on OER activity, so here it might also affect the catalytical performance. The O 1s region and corresponding oxygen species content are similar for all these four samples, in contrast, the more ratio of O-H content agrees with the higher concentration of Fe^{3+}, which also have some influence on the catalytical process.

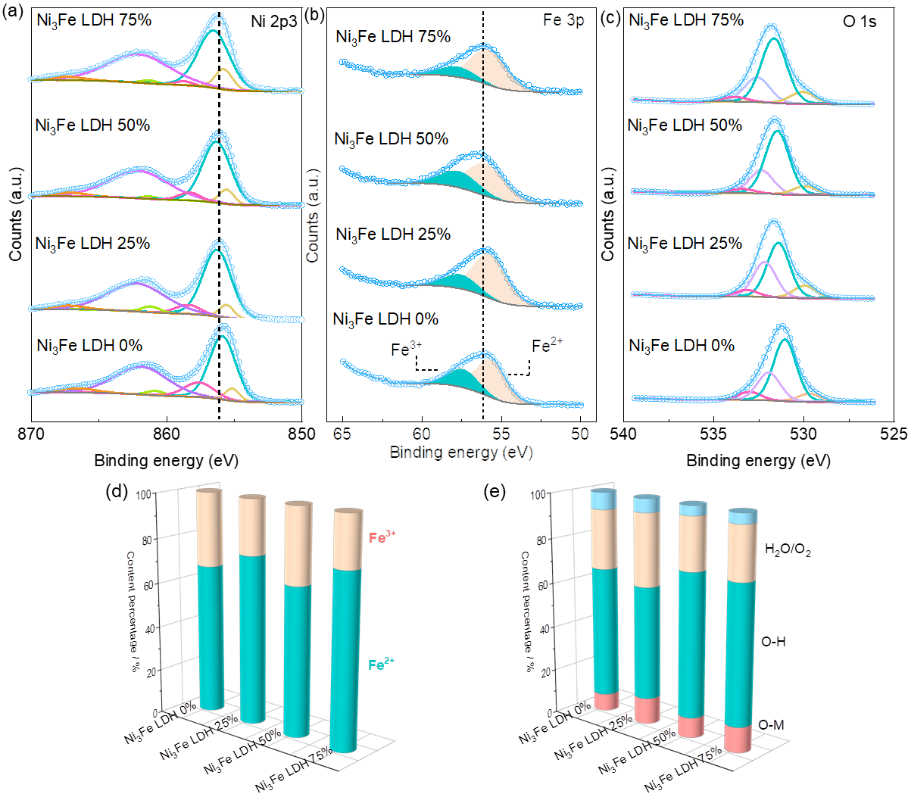

Figure 5.2 XPS spectra of NiFe LDH-F samples. (a) Ni 2p region. (b) Fe 3p region. (c) O 1s region. (d) (f) the Fe and O species calculated from corresponding XPS spectra.

The catalytical electrochemical performance of these Ni$_3$Fe LDH-F catalysts has been evaluated in **Figure 5.3**. First, the OER activity of these Ni$_3$Fe LDH-F catalysts are quite excellent, although a little lower than Ni$_3$Fe LDH (overpotential of 246 mV at 10 mA/cm2), but still not high (ranging from 260 to 280 mV). At the same time, the activity trend of the OER activity for these Ni$_3$Fe LDH-F catalysts are: F50 > F0 > F25 ≈ F75. The distinct changes of Ni redox peak of Ni$_3$Fe LDH-F in **Figure 5.3**b is also quite interesting, which indicate the different electronic structure and dynamic transition process. And the Tafel slope of Ni$_3$Fe LDH-F75 is quite low as shown in **Figure 5.3**c, indicating a fast electron/charge transfer process, especially at higher current density region. For their ECSA in **Figure**

5.3d, there is no big difference between each other. And the strange issue is the Tafel slopes differ from the activity trend: more active F0 and F50 show larger slopes while the less active F25 and F75 show lower Tafel slopes.

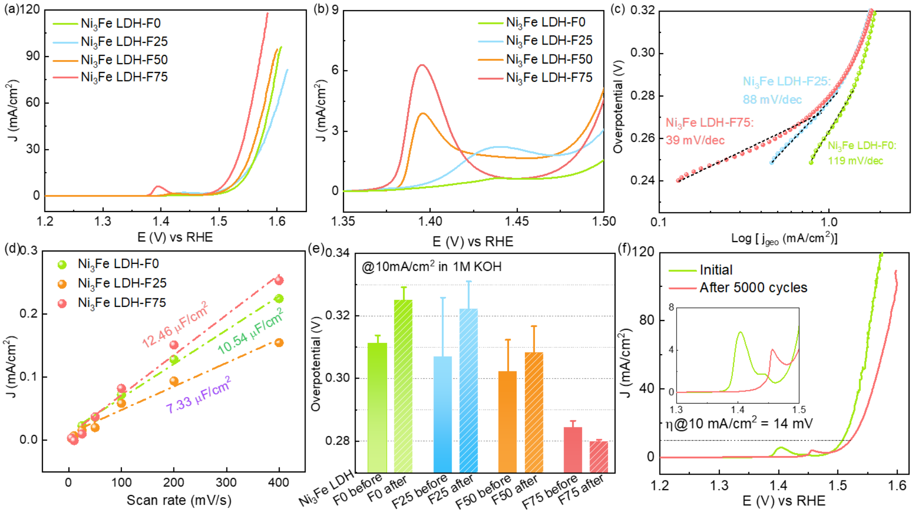

Figure 5.3 Electrochemical performance of NiFe LDH-F samples. (a) polarization curves. (b) corresponding amplified Ni oxidation peak region. (c) Tafel slope. (d) ECSA. (e) the overpotential at 10 mA/cm^2 during 1000 cycles between 1.0-1.7 V. (f) polarization curve and insert Ni oxidation peak during 5000 cycles between 1.0-1.7 V.

To compare the OER stability of these catalysts, the overpotentials before and after 1000 cycles are listed in **Figure 5.3**e. Their OER stability firstly decrease then improve as the ratio of formamide increase, so Ni3Fe LDH-F75 is the most stable one with nearly no degradation during 1000 cycles. Its good stability has been confirmed at extended condition 5000 cycles in **Figure 5.3**f and the slight degradation could be observed during this process, although not severe, the overpotential at 50 mA/cm^2 will increase 14 mV.

As we know, the OER stability of NiFe LDHs correlated to its layer structure, therefore, looking back to the XRD data of Ni3Fe LDH F0-75, we found F50 sample show higher peak intensity of (003) plane, indicating its multilayer structure, while this peak for F25 and F75 is less intense, meaning reduced layers.

This different layer structure could make clear the difference in stability.

To further verify the most stable Ni_3Fe LDH-F75 catalyst, we recorded the polarization curves after keeping at constant potential 1.6 V at extended time. As shown in **Figure 5.4**a and d, the long-time potentiostatic test of Ni_3Fe LDH-F75 on NF show some degradation. At the same time, we could find the main degradation occur at first 200 hours, later with a very stable performance. So its general stability is quite robust, and might be better with higher loadings. This is consistent with the results from 5000 cycling process, and these results indicate the degradation might occur mainly at OER process so the potentiostatic test won't show a very stable performance.

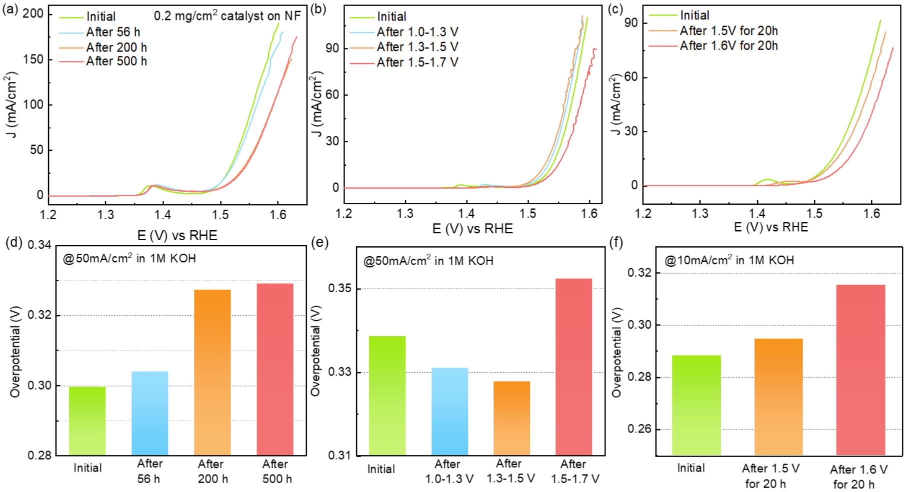

Figure 5.4 Extended stability test of NiFe LDH-F75 catalyst. (a-c) LSV curves before and after (a) keeping at 1.6 V for certain hours, (b) 5000 cycles between different ranges, and (c) keeping at certain potentials for 20 hours, (d-f) the corresponding comparison of overpotentials from (a-c) respectively.

Therefore, to figure out the range of this degradation, we compared the corresponding LSV curves after CV at different potential ranges for 5000 cycles: capacitance region (1.0-1.3 V), nickel redox region (1.3-1.5 V) and OER region (1.5-1.7 V), as shown in **Figure 5.4**b and e. Compared with initial activity, the OER current do not show any decline, but small increment after cycling between capacitance region (1.0-1.3 V), Ni redox region (1.3-1.5 V) for 5000 cycles. This means the phase transition between NiFe LDH and NiFeOOH won't affect the OER stability. While cycling at OER potential affects the stability of Ni_3Fe LDH-F75, the degradation appears. This indicates the possible mechanism is the metal dissolution at OER process as reported. Based on this conclusion, it is reasonable to observe the steady degradation when holding the Ni_3Fe LDH-F75 at constant OER potentials in **Figure 5.4**c and f.

In addition, the dynamic structure transition during the potential cycling process was also investigated by in situ Raman of Ni_3Fe LDH-F0 and F75 catalysts in **Figure 5.5**. The Raman spectra for pristine samples show similar Raman spectra with the peaks at 575, 785, and 1100 cm^{-1}. The peaks at 570 and 785 cm^{-1} are associated with NiFe LDH. While the band centered at 1100 cm^{-1} corresponds to interlayer nitrate ions from the synthesis process.

When the applied potential initiates and up to 1.3 V, the Raman spectra of Ni_3Fe LDH-F75 displays no extra characteristics peaks. From 1.4 V to 1.7 V in the forward direction and from 1.7 to 1.3 V backward direction, the catalyst shows peaks at 480 and 555 cm^{-1} which correspond to NiOOH.[203,168] In contrast, the Raman spectrum of Ni_3Fe LDH-F0 shows a series of characteristic peaks at around 520, 590, 685 cm^{-1} at 1.6 V in the forward direction. At 1.7 and 1.6 V in the backward direction, the catalyst displays Raman peaks at 485 and 555 cm^{-1} corresponding to bending and stretching of NiOOH.[203,168] Once the applied potential is reduced to 1.6 V and up to 1.3 V in the backward direction, the catalyst state transforms from NiOOH to the initial state with peaks correspond to NiFe LDH. Based on the above results, although Ni_3Fe LDH-F75 and Ni_3Fe LDH-F0 present similar chemical composition and ex-situ Raman signal, they behave differently under OER conditions. Ni_3Fe LDH-F75 shows the presence of active intermediate Ni(Fe)OOH at low potentials compared to Ni_3Fe LDH-F0, which also agrees well with their OER activity.

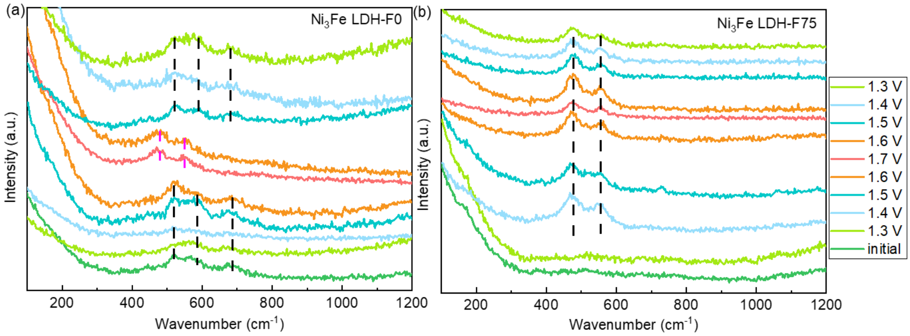

Figure 5.5 In situ Raman spectra of (a) Ni_3Fe LDH-F0 and (b) Ni_3Fe LDH-F75 catalysts.

In summary, the introduction of formamide in the solvent could modify the layer structure. The reduced stacked layer of Ni_3Fe LDH-F75 shows improved stability than pristine sample, and the further investigation confirm the main degradation occurs at OER region. The in-situ Raman spectra reveals lower potential for the presence of active species for Ni_3Fe LDH-F75, accounting for its better OER activity. Generally, all the different OER performance of these Ni_3Fe LDH-F catalysts could be understand by their spatial and electronic structures, supporting the conclusion from last chapter. And this strategy could improve the OER activity and stability, but still not obtain a perfect NiFe LDH catalyst.

5.3 Incorporation of interlayer ions

According to reported works, the interlayer ions in the LDH structure could affect the basal spacing and size, therefore, their catalytical performance.[170,182] Based on this, incorporation of certain ion with bigger radius into the NiFe LDH might enlarge the layer spacing and further exfoliate the former multilayer into monolayer NiFe LDHs, as illustrated in **Figure 5.6**a. So we synthesize a series of Ni_3Fe- $xMnO_4$ -LDH samples (x=0, 0.5, 1 and 2, the input ratio of MnO_4^- ions) as follows: 25 ml mixed Ni/Fe solution (3 mmol $Ni(NO_3)_2·6H_2O$ and 0.75 mmol $Fe(NO_3)_3·9H_2O$), and 25 ml NaOH + x mmol MnO_4^- solution, were mixed and stirred strongly (1000 rpm) for 10 minutes, then the precipitate was washed by DI water and ethanol then collected.

As the ratio of MnO_4^- ions increased, the color of powder inks in **Figure 5.6**b gets dark gradually, implying the possible structure changes. Their elemental compositions were verified by ICP-OES in **Table 5.1**, and the incorporation of MnO_4 were only small amount even the input ratio is higher than Fe, and the composition does not change severely for the three samples. Then their XRD patterns were obtained and compared in **Figure 5.6**c. First, the introduction of MnO_4^- ions does not change the crystal structure of NiFe LDH, regardless of the amount. However, there are changes of peak intensities and position indicating modified layer structure after incorporating MnO_4^- ions: the peaks of (003) and (006) planes at 11 and 23 ° in **Figure 5.6**e shift negatively, meaning the enlarged layer spacing according to the equation $2d*\sin\theta=\lambda$. This is consistent with the reported linear correlation of measured basal spacing with anionic radii other LDH system if we assume the MnO_4 anions did indeed reside in the interlayers.[170]

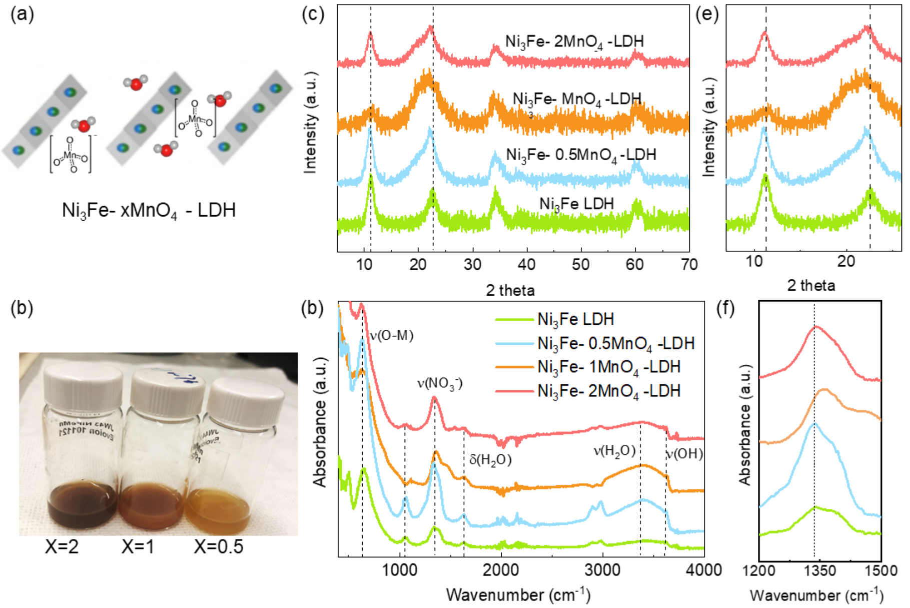

Figure 5.6 (a) Illustration of crystal structure of Ni_3Fe- $xMnO_4$ -LDH. (b) corresponding powders inks. (c,e) XRD pattern and (b,f) IR spectra of NiFe- $xMnO_4$ -LDH samples.

Table 5.1 Element ratio of metals in the NiFe- $xMnO_4$ -LDH samples.

Sample	Actual ratio by ICP OES (ε ≤ 1%)		
	Ni	Fe	Mn
Ni_3Fe- 0.5MnO_4 -LDH	73.7	19.8	6.5
Ni_3Fe- MnO_4 -LDH	66.6	27.1	6.3
Ni_3Fe- 2MnO_4 -LDH	68.3	18.1	13.6

To further verify the successful incorporation of MnO_4^- ions into the NiFe LDH interlayers, we carried out IR tests to check the interlayer ions and possible structural changes. As shown in **Figure 5.6**b, all the Ni_3Fe -$xMnO_4$ -LDH samples show similar IR spectrum as pristine NiFe LDH, but as the amount of doped MnO_4^- increased, the peaks at 1060 and 3300-3600 cm^{-1} decrease, indicating the reduced amount of absorbed OH/H_2O. At the same time, another obvious peak of Ni_3Fe-MnO_4-LDH at 1200-1500 cm^{-1}, ascribed to the interlayer ions, show distinct peak shape and position in **Figure 5.6**f. This characteristic signal changes agree with the effect from MnO_4 ions,[211] also consistent well with the phenomenon from XRD patterns.

The effect from incorporated MnO_4^- ions on the electronic structure of Ni_3Fe LDH was also studied by XPS and the spectra of typical Ni_3Fe -MnO_4- LDH and Ni_3Fe LDH were compared in **Figure 5.7**. The similar survey spectra contain the signal from common elements O, Ni and Fe. While the three deconvoluted oxygen species of Ni_3Fe -MnO_4- LDH could be attributed to oxide (5.6%), OH (85.2%) and H_2O (12.2%) groups, close to the contents of Ni_3Fe LDH. The general shape of O 1s region is slightly different, which might come from the doped MnO_4 ions. For the Ni 2p region, consistent with former analysis, all the peaks agree well with the Ni^{2+}. The Fe 3p region were fitted as Fe^{2+} and Fe^{3+} species, and there are also no obvious differences for the general signals. Therefore, the XPS data confirm the incorporation of MnO_4^- ions does not change the same chemical states of Ni and Fe, only minor variation of oxygen species.

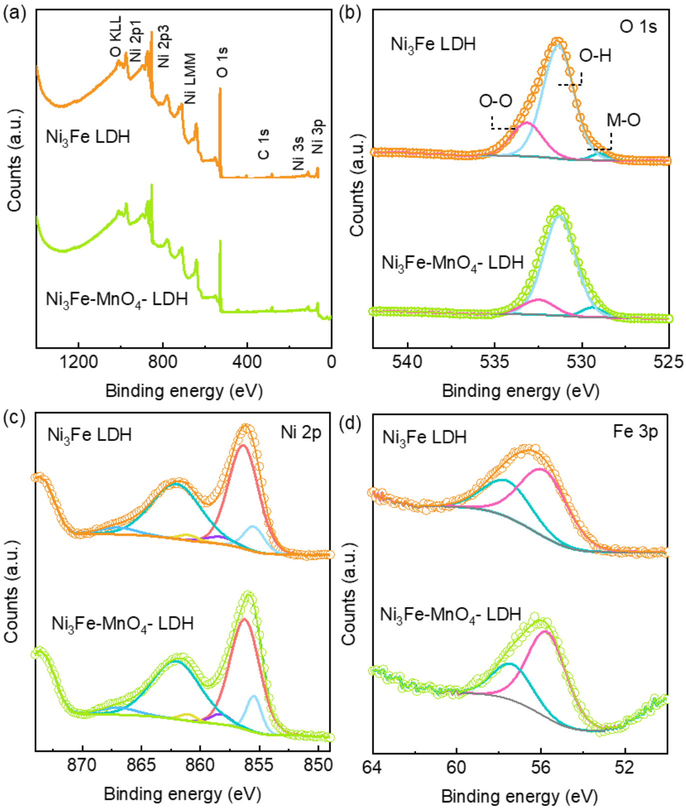

Figure 5.7 XPS spectra of Ni_3Fe- MnO_4 -LDH and Ni_3Fe LDH samples. (a) survey spectra. (b) O 1s region. (c) Ni 2p region. (d) Fe 3p region.

Then the OER performance of these Ni_3Fe- xMnO_4 -LDH catalysts were evaluated and the polarization curves with overpotentials during 1000 cycles were compared in **Figure 5.8**. The initial samples exhibit excellent OER activity with overpotentials comparable to Ni_3Fe LDH but at same time its stability during 1000 Cs is not robust as well. As the ratio of MnO_4^- increases, their OER activity decreases, while the other two samples with more MnO_4^- show no degradation after 1000 cycles. Same as the trend in the NiFe LDHs, this strategy leads to worse activity but better stability.

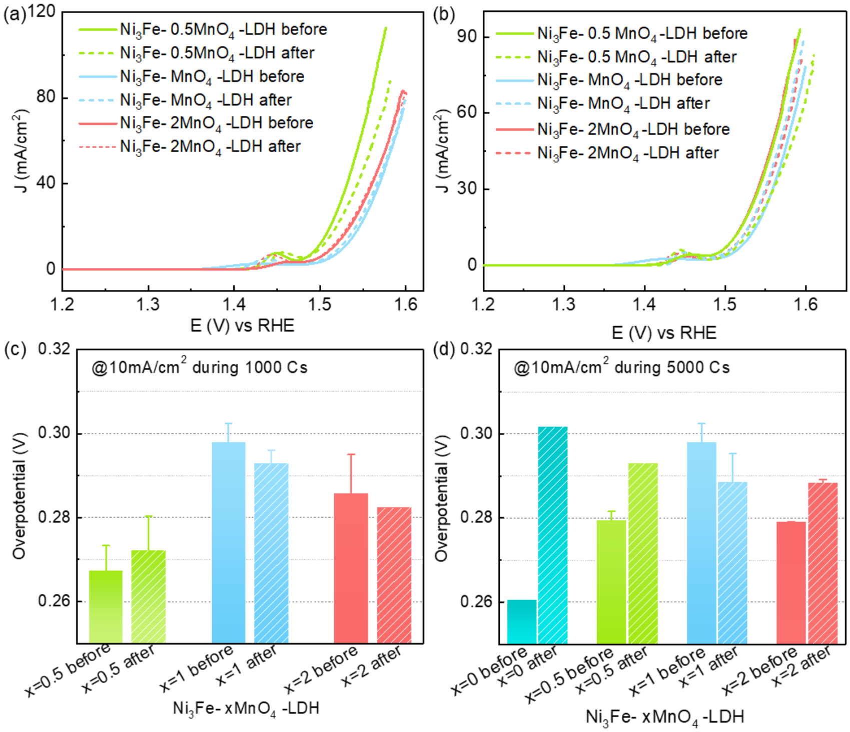

Figure 5.8 (a,b) Polarization curves and (c,d) corresponding overpotentials at 10 mA/cm^2 of Ni_3Fe-xMnO_4-LDH catalysts before and after (a,c) 1000 and (b,d) 5000 cycles between 1.0-1.7 V in 1 M KOH.

Then their longer stability was tested at extended 5000 cycles, and found Ni_3Fe-2MnO_4-LDH did not exhibit even better activity than Ni_3Fe-MnO_4-LDH as expected, but both of them are more stable than Ni_3Fe LDH. In contrast, the extended stability of Ni_3Fe-0.5MnO_4 -LDH is not as good as the others, indicating the amount of MnO_4^- works. It should be at a certain range around Fe: Mn=1:1 while less or excessive doping will not help further.

In summary, incorporation of MnO_4^- ions into the interlayer of Ni_3Fe LDH could modify the layer structure by enlarging spacing and reducing stacked layers. At the same time, it won't change the chemical states of metal sites. The incorporation will lead to improved OER stability compared with Ni_3Fe LDH, however, the activity is not boosted as expected, which requires further studies.

5.4 Heat treatment

As reported, the layer spacing of LDH would shrink upon annealing, and this structure change would lead to the influence on their OER performance.[118] Therefore, we put the Ni_3Fe LDH for heat treatment to check the effect of temperature on structure and electrochemical properties of Ni_3Fe LDHs. The Ni_3Fe LDH powders are put into the ceramic boat, and then transferred into vacuum oven at controlled temperature for 1h. The pressure is kept at 100 mbar, temperatures are 100, 150 and 200 °C (named as Ni_3Fe LDH-100, 150, 200).

Firstly, the crystal structure changes from heat treatment were studied by XRD patterns. As shown in **Figure 5.9**a, the series of peaks change as temperature increase compared with initial Ni_3Fe LDH: from 100 to 150 °C, the intensity of peaks at 12° and 24° decrease, and at the same time, there is a red shrift, indicating the shrinkage of layer distance at higher temperature. The constant peak at 34° and 60° confirm the reliability of peak shrift, not owing to signal drift, and the stable matrix LDH structure. This trend is consistent with previous report, but the difference is the XRD pattern of Ni_3Fe LDH-100 is nearly same as 150 °C, while all the peaks disappeared in the report,[118] indicating different structure change and effect from heat treatment process.

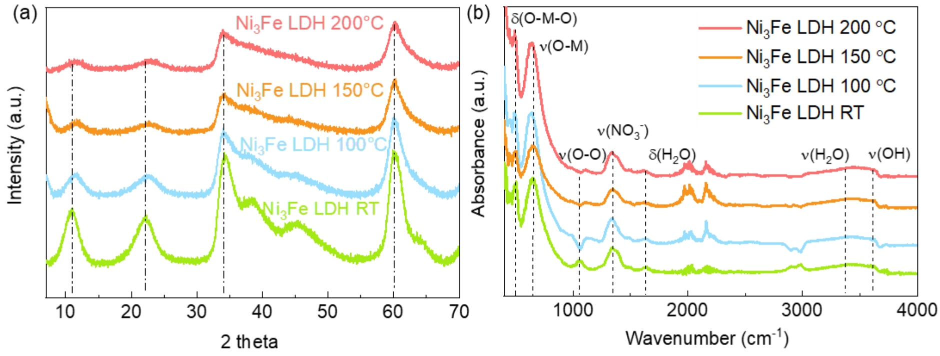

Figure 5.9 (a) XRD pattern and (b) IR spectra of Ni_3Fe LDH after heat treatment at various temperatures, 100, 150 and 200 °C for 2 hours.

The infrared spectra were also collected in **Figure 5.9**b to check the structure evolution of Ni_3Fe LDH upon annealing from 100 to 200 °C. The bands centered at 617 and 797 cm^{-1} are attributed to the scissoring and stretching vibrations of M-O. The intensities and frequencies of the vibrations are influenced by hydrogen bond. The changed intensity and position of the scissoring vibration (δ(M-O)) and the stretching vibration (v(M-O)) are both related to reduced hydrogen bonding, which confirm the effects from high temperature. At the same time, the bands at 1350, 1620, and 3365 cm^{-1} are characteristic for NO_3^-, scissoring, and stretching mode of structure water, respectively. The sharp and intensive vibration at around 3630 cm^{-1} is related to free O-H groups, these nearly unchanged peaks during annealing indicate that NiFe LDH only undergoes water desorption without hydroxide decomposition, consistent with report.

However, the difference from our result with literature is that there is no obvious decline in relative intensity at 1350 cm^{-1} owing to the release of CO_2 with increasing annealing temperature, so to some extent, we could conclude that NO_3^- ion interlayer LDHs show better structural stability under annealing conditions. This might also be the reason why our NiFe LDH after heat treatment did not show obvious structure changes in XRD patterns.

Then the chemical states of Ni_3Fe LDH after heat treatment were revealed by XPS spectra in **Figure 5.10**. For O 1s region, the Ni_3Fe LDH-100 shows similar signal and the deconvoluted peaks, indicating unchanged electronic structures. As the temperature increases to 150 °C and 200 °C, the species of OH gradually takes more proportion. At the same time, the XPS spectra of Ni 2p region exhibit close signals without peak shift or shape variation. And all the fitted peaks are consistent with Ni^{2+} content, confirming the same oxidation state during heat treatment process. In contrast, the Fe 3p region exhibit a certain difference of peaks. The deconvoluted peak at 58 eV, attributed to Fe^{3+}, increases as temperature rises. This trend is also confirmed by the quantitative analysis of each content for different O and Fe species. As we know, these electronic structure changes of these catalysts will affect the dynamic absorption and desorption of intermediate species thus the catalytical performance.

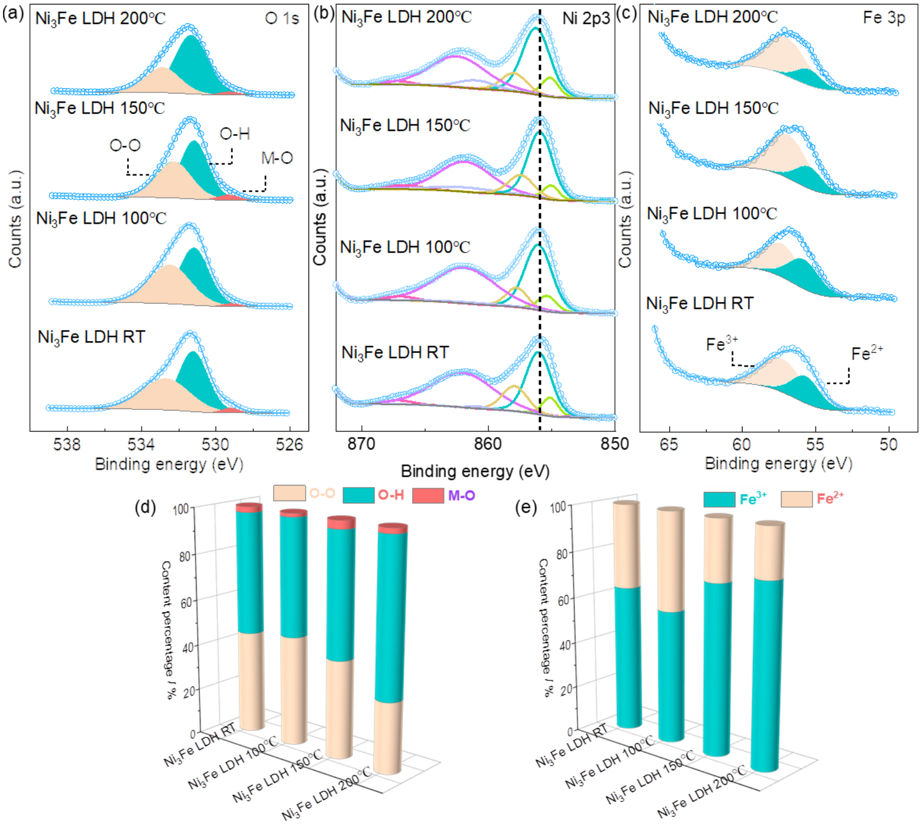

Figure 5.10 XPS spectra of Ni3Fe LDH after heat treatment at various temperatures. (a) O 1s region. (b) Ni 2p region. (c) Fe 3p region. (d) (f) the O and Fe species calculated from corresponding XPS spectra.

The electrochemical tests of these Ni3Fe LDHs in 1M KOH show the general activity in **Figure 5.11**, and as annealing temperature increases, their current density decease slightly, also revealed by the corresponding overpotentials. It could be explained as the temperature increase, the layer spacing decrease, leading to the decreased ECSA. The Tafel slope of these annealed sample are close to each other, implying similar kinetic process for OER. Moreover, their stability over 1000 cycles gradually improved slightly at higher temperature, revealed by the less increasement of overpotentials. But the degradation still exists for all these Ni_3Fe LDH catalysts, which mean this method does not work.

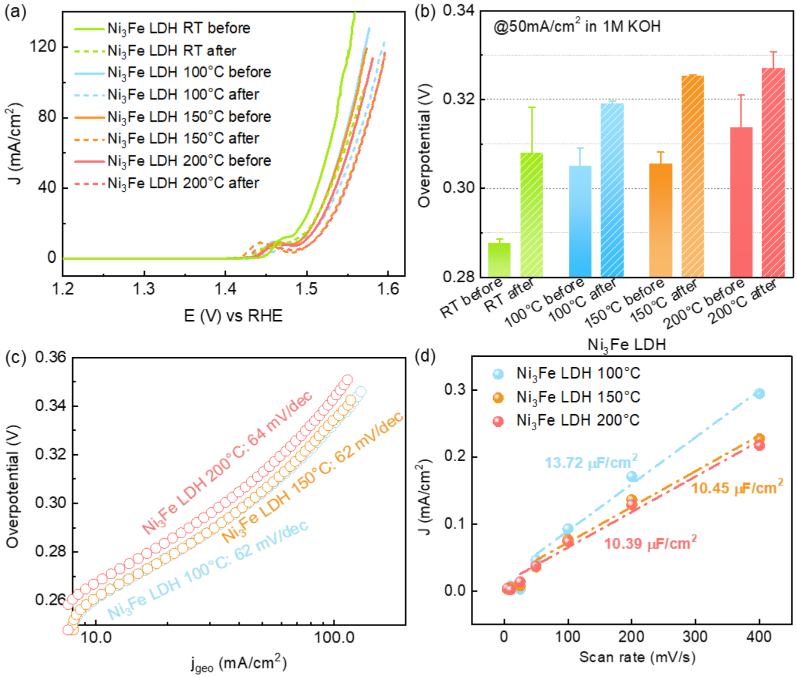

Figure 5.11 Electrochemical test of Ni_3Fe LDH after heat treatment at various temperatures. (a) LSV curves and (b) overpotential after 1000 cycles between 1.0-1.7V and (c) their initial ECSA and (d) Tafel slopes.

In summary, the heat treatment results in the layer spacing shrinkage to some extent, but does not form the monolayer Ni_3Fe LDH. This layer structure change affects the chemical states of oxygen and iron to some extent, and therefore, the OER activity. But the OER stability only improves in a limited range, and the general catalytical performance is not as good as initial Ni_3Fe LDH. From this perspective, this strategy does not meet our former expectation, and further investigation is required to improve it later.

5.5 Hydrothermal treatment

The NiFe LDHs synthesized by precipitation method are regarded as with low crystallinity with higher disorder degree,[202] which was also confirmed by our structural analysis of the NiFe LDHs with different composition in chapter 3. Previous work has reported numerous NiFe LDH catalysts obtained at hydrothermal process with well-defined hexagonal shape and excellent crystallinity,[166,214] and the precipitated LDH after hydrothermal treatment at higher temperature and extended time could increase the crystallinity as well.[201] Therefore, hydrothermal treatment of NiFe LDH might be a feasible strategy to increase the crystallinity and improve the OER stability of catalysts.

Therefore, Ni_3Fe LDH and $NiFe_3$ LDH were selected as examples and their powders were transferred into autoclave at 200°C for 2 h for hydrothermal treatment. Then the new samples Ni_3Fe LDH 2 h and $NiFe_3$ LDH 2 h are obtained. The elemental ratio in **Table 5.2** proves the hydrothermal process did not affect their composition of Ni and Fe, but probably structures of NiFe LDHs. The XRD patterns of Ni_3Fe LDH 2h in **Figure 5.12**a verify the new sample is still NiFe LDH, but the intensities of a series of peaks at ~35°, 39° and 60°, 62° (refers to (101), (012), (110) (013) planes) increased compared with the ones of layer structure (11° and 23°, refer to (003) (006) planes) after hydrothermal process, indicating the enhanced crystallinity of LDH matrix.

Table 5.2 Element ratio of NiFe LDH before and after hydrothermal treatment.

Sample	Actual ratio by ICP OES ($\varepsilon \leq 1\%$）	
	Ni	Fe
Ni_3Fe LDH	77.0	23.0
Ni_3Fe LDH 2h	78.7	21.3
$NiFe_3$ LDH	23.6	76.4
$NiFe_3$ LDH 2h	27.5	72.5

The difference is initial $NiFe_3$ LDH exhibit almost amorphous structure in **Figure 5.12**b, and the $NiFe_3$ LDH 2h sample shows obvious crystal peaks of NiFe hydroxides (PDF#14-0556), also could be regarded as monolayer LDH. Here, the crystallinity index, the ratio of the area from crystalline peaks to the total of crystalline and amorphous peak, is calculated and compared. The corresponding crystallinity degree increases from 5% to 79% during this process as shown in **Figure 5.12**c. It means the treatment could not increase the stacked layers, but enhance the crystallinity of nanosheet matrix from amorphous structure to good nanocrystals.

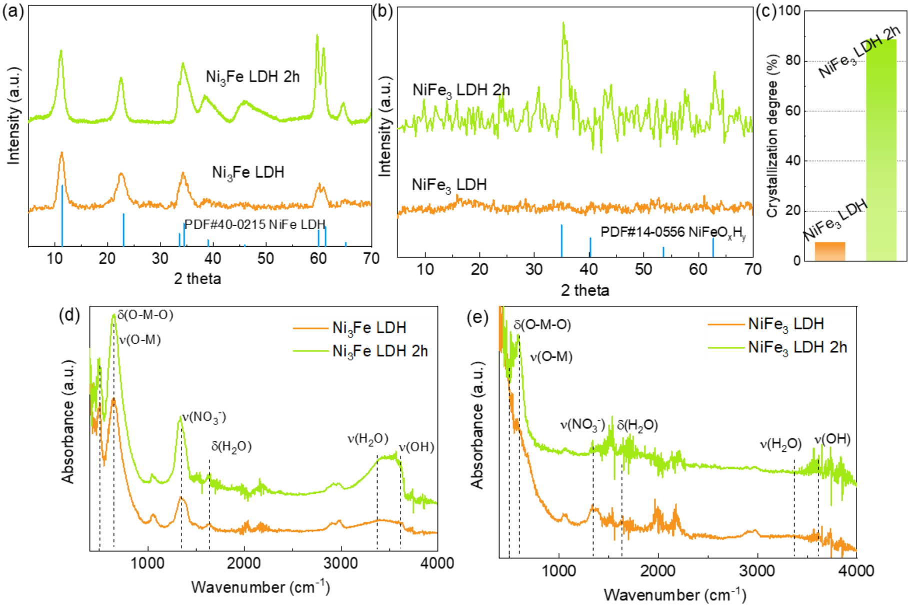

Figure 5.12 (a-c) XRD patterns and (d-e) IR spectra of NiFe LDH before and after hydrothermal treatment. (a,d) Ni_3Fe LDH. (b,c,e) $NiFe_3$ LDH.

More IR tests were conducted to check the structural evolution during the hydrothermal process for these NiFe LDH samples. As shown in **Figure 5.12**d-e, Ni_3Fe LDH and Ni_3Fe LDH 2h show all similar peaks but with different intensity, especially at 1350 and 3300-3600 cm^{-1}, attributed to interlayer ions and H_2O/OH^-, indicating the increased stacking layer structure of NiFe LDH nanosheets, consistent with former XRD data.

Surely such kind of structural and crystallinity could be observed more directly by TEM images. The initial Ni_3Fe LDH shows dispersed multilayer nanosheets, while the stacked layers increased after hydrothermal thermal process in **Figure 5.13**a and b, consistent with the results from XRD and IR. In contrast, the morphology changed more obvious for $NiFe_3$ LDH samples. The monolayer amorphous nanosheet transited into distributed ultrasmall nanoplates, and the corresponding diffraction pattern confirm the improved crystallinity.

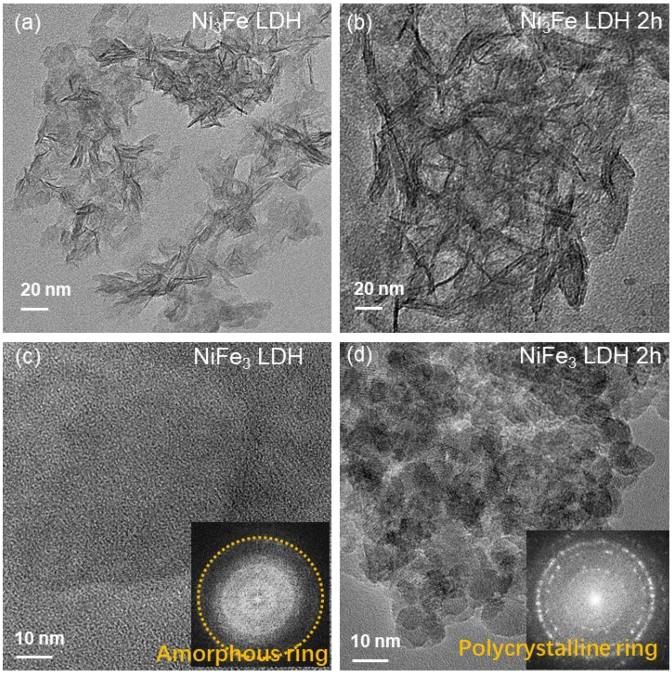

Figure 5.13 TEM images of NiFe LDH (a,c) before and (b,d) after hydrothermal treatment. (a,b) Ni_3Fe LDH. (c,d) $NiFe_3$ LDH.

Then we evaluated the OER performance of these NiFe LDH catalysts by cycling the electrode in 1M KOH for 1000 cycles between 1.0 and 1.7 V. The polarization curves and corresponding overpotentials are compared in **Figure 5.14**. For the activity, it is reasonable to find the more crystalline catalysts with less active sites present lower current density for the Ni_3Fe LDH 2 h sample. This is also confirmed by the reduced ECSA. While for the stability, here the Ni_3Fe LDH 2 h sample did not show improved stability although it is generally holding that crystalline catalysts are more stable. The possible reason could be the increased stacked layers during hydrothermal process for Ni_3Fe LDH 2 h will lead to the severe dissolution according to our current understanding.

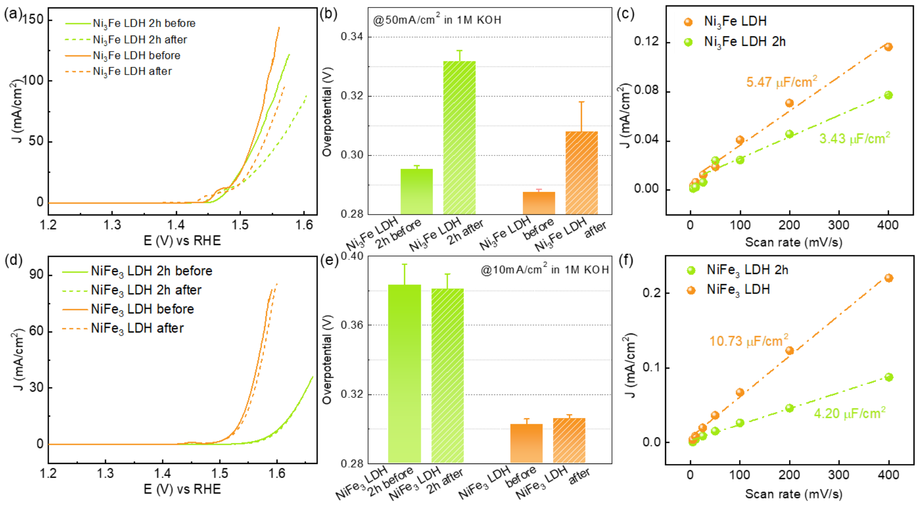

Figure 5.14 Electrochemical performance of holding NiFe LDH before and after hydrothermal treatment. (a,d) polarization curves and (b,e) corresponding overpotentials at 50 mA/cm^2 during 1000 cycles between 1.0-1.7 V. (c,f) ECSA. (a-c) Ni_3Fe LDH. (d-f) $NiFe_3$ LDH.

Similarly, we also reported the OER performance of $NiFe_3$ LDH and $NiFe_3$ LDH 2 h, which transited from amorphous to crystalline structure. The treated $NiFe_3$ LDH 2 h catalyst exhibits much worse OER activity but slightly increased stability. For the activity, one reason is the crystalline catalysts with less active sites, verified by the reduced ECSA. Another reason is the possible elemental segregation to form a Ni core and Fe shell structure. Then the Fe-rich surface is far away from the best ratio of Ni/Fe ratio, so exhibit worse activity then homogenous $NiFe_3$ LDH. While for the stability, firstly there is no more layer stacked, which is harm to the durability. And even if the core/shell Fe/Ni structure really exists, it also presents improved activity during the cycling process.

Based on above discussion, the hydrothermal effect works more obviously for amorphous NiFe LDH. Therefore, it is necessary to study the effects of hydrothermal treatment on a series of other NiFe-based materials, including sulfides and molybdate, phosphate. The pristine precipitate samples named as a-NiFe (a-Ni_3FeS and a-Ni_3FeMoO_4) and the one after hydrothermal process at 200 °C for 2 h named as c-NiFe (c-Ni_3FeS and c-Ni_3FeMoO_4).

The crystal changes are compared by XRD patterns in **Figure 5.15**a and b. The precipitate a-Ni_3FeMoO_4 sample show only a wide peak at ~22°, while the crystalline sample exist a series of peaks, which corresponds to the $NiMoO_4$ phase (PDF#33-0948)., the slight deviation could be from the modified lattice from doped Fe. The Ni_3FeS is consistent well with Ni_3FeMoO_4 sample: precipitate powder shows no obvious crystal peaks while after hydrothermal treatment, Ni_3FeS agrees well with the $NiFeS_2$ structure (PDF#02-0850). In general, the hydrothermal treatment could assist the transition of amorphous samples into crystalline NiFe sulfides and molybdates, and it can be expected for their different morphologies.

Then we check the structures and morphologies of Ni_3Fe sulfides and molybdates by SEM images. As shown in **Figure 5.15**c-d, the a-Ni_3FeMoO_4 consists of nanoparticles with radius of the tens of nanometers, while the new sample c-Ni_3FeMoO_4 are well-defined nanorods with certain remaining nanoparticles after hydrothermal process. The nanorods are typical shape of molybdates consistent with previous report,[215,216] while the remaining nanoparticles could be the excessive MoO_4 at precipitation process. For sulfides, the pristine a-Ni_3FeS presents various species, the majority are several micromanometer plates, probably $Ni(OH)_2$ after precipitation, while the others are smaller size particles. After hydrothermal process, the c-Ni_3FeS shows more regular shaped nanoparticles with uniform sizes, indicating the formation of crystalline sulfides. It could be deduced the atomic structure migration and rearrangement of these samples, and lead to well-defined nanocrystals. But the resolution of SEM is limited to observe more details of these samples, so TEM or HRTEM images are required for further information.

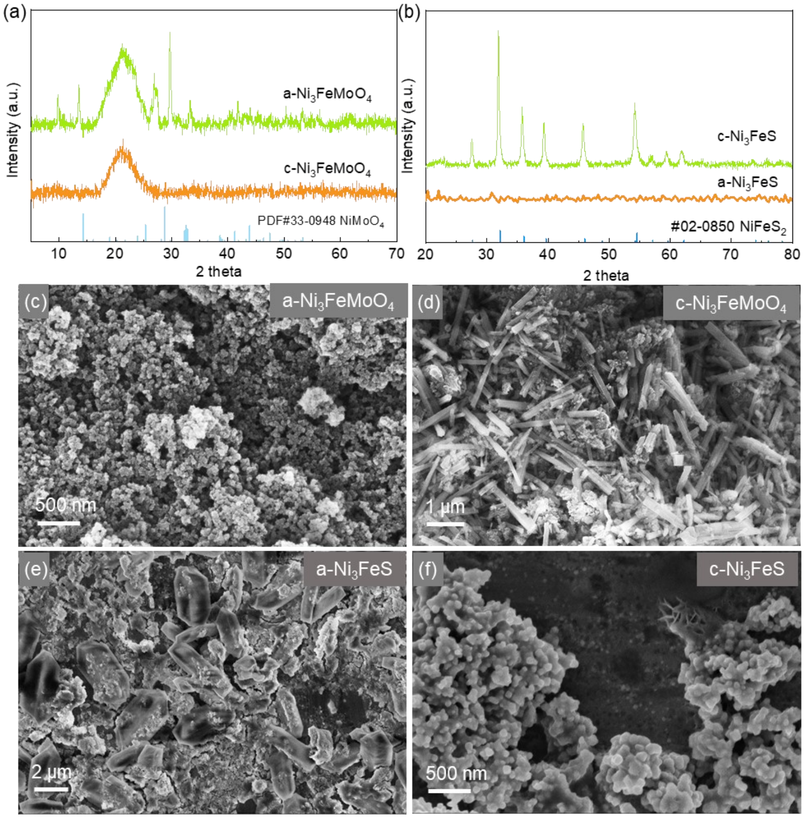

Figure 5.15 XRD patterns of (a) amorphous and crystalline Ni_3FeMoO_4, (b) amorphous and crystalline Ni_3FeS. (c-f) SEM images of (c) amorphous and (d) crystalline Ni_3FeMoO_4, (e) amorphous and (f) crystalline Ni_3FeS samples.

The (HR)TEM of these Ni_3Fe sulfides and molybdates are presented in **Figure 5.16**. The a-Ni_3FeMoO_4 looks like fluffy porous sponge, a typical morphology of amorphous samples, confirmed by its HRTEM image and corresponding FFT pattern. In contrast, the c-Ni_3FeMoO_4 exists the nanorods with the length of hundreds of nanometers. And the HRTEM image reveals the lattice spacing of 8.6 Å, attributed to the (100) planes of $NiMoO_4$. The insert FFT patterns corresponds to the (011) and (111) planes in the <011> axis. For NiFe sulfides, STEM images show pristine a-Ni_3FeS consists of various irregular particles to form aggregates, while c-Ni_3FeS are mostly regular octahedrons with the size close to 100 nm. These results confirm the structure evolution of NiFe sulfides and molybdates during the hydrothermal process.

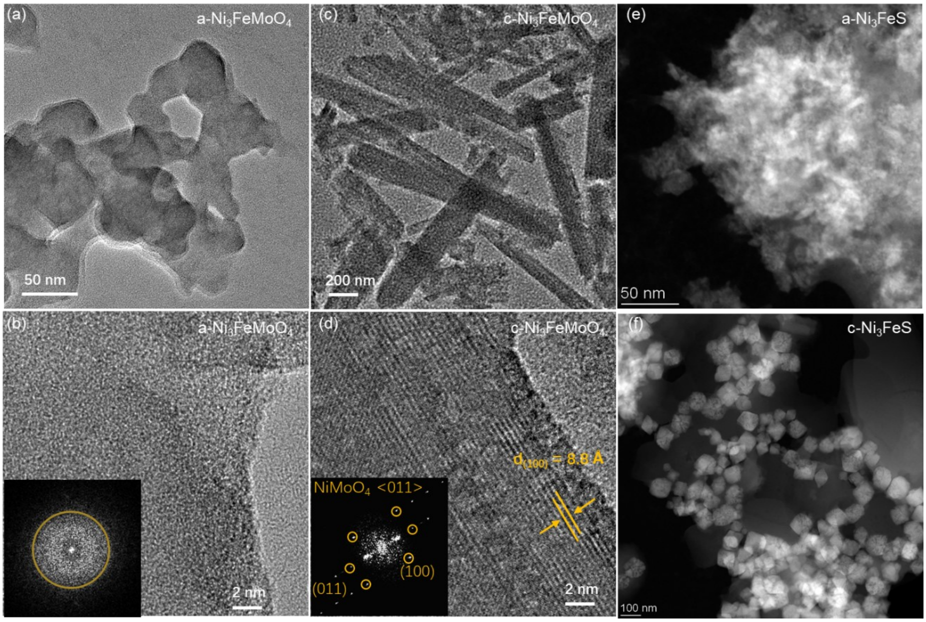

Figure 5.16 TEM images of (a,c) amorphous and (b,d) crystalline Ni_3FeMoO_4. STEM images of (e) amorphous and (f) crystalline Ni_3FeS samples.

The influence of these structure changes on OER performance were verified in **Figure 5.17**. The c-Ni_3FeMoO_4 exhibits slightly lower OER activity than pristine a-Ni_3FeMoO_4, revealed by their LSV curves and overpotentials at 10 mA/cm^2. This difference could result from their lower surface area for crystalline samples. While after 1000 cycles, a-Ni_3FeMoO_4 shows more obvious degradation with increased overpotentials, but the counterpart for c-Ni_3FeMoO_4 even deceased. This trend is similar for NiFe sulfide system. The c-Ni_3FeS is less active but more stable than a-Ni_3FeS catalysts. All these findings agree with the common view that the crystalline structure possess robust stability than amorphous ones.

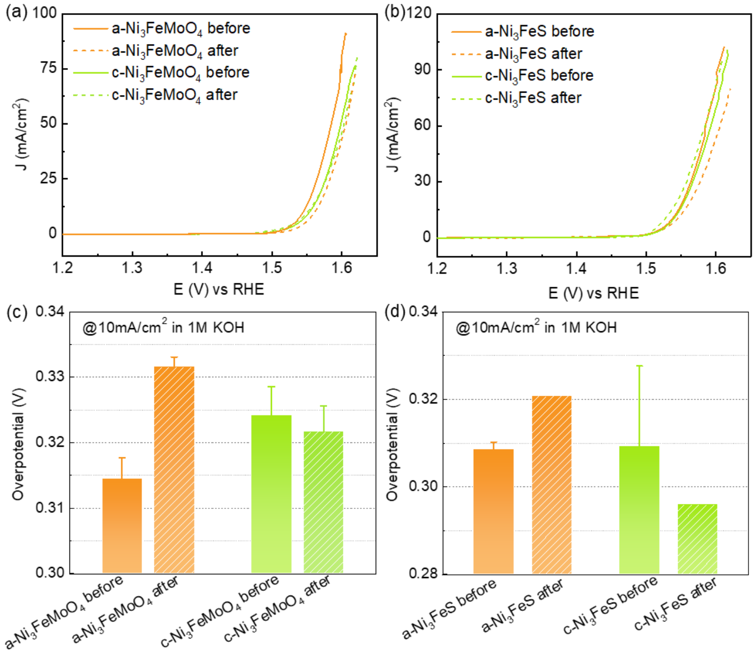

Figure 5.17 Electrochemical performance of (a,c) amorphous and crystalline Ni_3FeMoO_4, (b,d) amorphous and crystalline Ni_3FeS samples. (a,b) polarization curves and (c,d) corresponding overpotentials at 50 mA/cm^2 during 1000 cycles between 1.0-1.7 V.

5.6 Chapter summary

To sum up, we have adopted and conducted several kinds of strategies to modulate the structure of NiFe LDH for optimized OER activity and stability. Among them, heat treatment brings the shrinkage of layer spacing but not the expected improved catalytical performance. The introduction of formamide in the solvent and incorporation of MnO_4^- ions into the interlayers could help to reduce the stacked numbers and layer distance, therefore, lead to enhanced OER stability. Similarly, the hydrothermal treatment could also increase the stability by forming of more crystalline nanocrystals. And this approach was also extended and applied in other NiFe-based systems, confirming it is a reliable method to increase the crystallinity and further catalytical durability of these catalysts.

Chapter 6 Discussion

For the evaluation of catalytical performance of electrocatalysts on half cell RDE, all kinds of detailed parameters from the testing setup and procedures matter but these are still not universal up to now even electrolysis has been developed over 100 years and massive related work has been published every year. The reason could come from the complexity of different kinds of catalysts or there is no a strong enough call or mandatory rule to get everyone to follow a uniform protocol in their publications. Therefore, these influential test conditions are flexible and variable, so the fairness and reasonableness when reporting catalyst performance depend on the scientific conscience of the experimenter sometimes. From our perspectives, we aim to conduct relevant investigations on the effects of testing protocols, then determine an objective standard procedure for our catalyst and the whole scientific community.

The parallel experiments from the different choices of experimental testing setup confirm the effects of counter electrode, cell, electrolyte and working electrode. The Pt and graphite make no difference on the initial actives on all three kinds of electrodes, but the gradual oxidation of carbon at extended cycles will contribute extra current and overlap with the OER current, thus finally lead to the overestimation of catalyst performance. And this phenomenon exists only after 1000 cycles, not a very long-term test, so we think the graphite is not suitable to use as a counter electrode for stability evaluation, and in contrast, Pt is a better choice.

For electrochemical cells, catalytical performance measured in the glassy and Teflon cell are consistent with each other for both activity and cycling stability. Although previous works have reported the slow dissolution of glassy material in alkaline solution, the possible derived ions probably do not affect the OER process as they are not OER active and there is no redeposition process to cover the catalyst surface at oxidative potential. Considering the protection of the electrochemical cell itself, the Teflon cell is more stable and reliable in alkaline conditions.

The electrolytes, not only provide the OH group as the reactant, but also work as media for charge transfer and mass transfer in the reaction. Therefore, the physicochemical properties, for instance, electrical conductivity and viscosity, of different electrolytes KOH and NaOH will affect the performance of the catalysts tested. We found the activity trend to be better in KOH than in NaOH. The impurity Fe ions in initial KOH are absorbed and affect the activity of OER performance of the catalyst. Especially for nickel-based materials dual NiFe active species are formed. It makes sense that the difference in stability is more pronounced than the activity performance in purified and unpurified KOH as the absorption of Fe takes time then works continuously at the cycling process. At the same time, the potentiostatic stability in both purified and unpurified KOH do not exhibit severe degradation during the cycling process, implying the role of potential on the stability mechanism of Ni-based OER catalysts. It could be deduced the reduction reaction at cycling process leaves negative effect on degradation, possible the metal dissolution at phase transition, a similar mechanism as we proposed later for NiFe LDH.

Without any doubt, the working electrode, composed mainly but not fully of catalysts, have even more evident impact on the presented performance. Needless to say, the type of binder, the ink configuration and the catalyst itself, even the two basic parameters, loading and substrate, of working electrode, exhibit dependent activities. The coated loading determines the total amount of catalyst on the substrate, but not the number of active sites as only surface sites could participate in the reaction. Too high loading will lead to the mutual coverage and increased charger transfer and mass transfer resistance during catalytical process. Therefore, the OER activity of catalysts increase first as loading increase then decrease while further more catalysts were added. The nature effect from substrates on catalysts is also similar, which influence the number of active sites and dynamic transfer process. The porous three-dimensional NF and CP could assist catalysts presenting higher activity than common GC substrate. But these factors do not affect the stability trend at both cycling process and potentiostatic conditions.

For the testing protocols, we consider to exclude all possible inconsistent factors on the catalyst surface, for instance, the oxidation state and attached bubbles. The CV activation was pretreated to reach a similar status and reductive potential was applied to remove the bubbles at surface before the activity evaluation, thus a relatively consistent and reliable result could be obtained. As we know, there is continuous oxygen bubbles generated at the catalyst surface, which will interrupt the subsequent catalytic process and apparent currents. Therefore, the consecutive record of current or potential during stability tests are mostly unreliable with periodic oscillation, while the comparison of polarization curves before and after this period could skip the affected part and provide objective evaluation.

Based on the above determined testing setup and measurement procedure, we also synthesized a series of reported high-performance catalysts and compared their OER performance in our universal protocol, which exhibit distinct nominal activity. At the same time, the benchmark of various OER catalysts points out NiFe LDH is a kind of active and durable catalyst on RDE and promising for alkaline water electrolyzer. So we synthesized different NiFe LDH with tunable composition by precipitation principle. This method could provide large scale powders at room temperature without any additives. From the perspective of cost, this catalyst is economical and suitable for potential commercial application.

The structures of these NiFe LDH were investigated by various techniques, which collectively demonstrate the compositional dependent morphology, size crystallinity and chemical environment. According to the growth mechanism, iron ions are precipitated earlier than nickel then followed by the diffusion and migration process to form homogenous material. The nature of these differences come from the modulated physical and chemical property of these bimetallic hydroxides. As more Fe incorporated in the NiFe LDHs, the higher disordered level and the unsaturated oxygen coordination around Fe of the sample presents, so the trend is reduced crystallinity. Meanwhile, as the amount of Fe^{3+} is reduced, the interlayer hydrogen bonds weaken, and therefore leads to a monolayer nanosheet.

Here it is worthwhile to discuss more about the structure of NiFe LDHs, especially at higher Fe ratio. As the XRD pattern and TEM image of the $NiFe_3$ LDH do not present characteristic signal to distinguish its crystal phase, and previous work has pointed out the characteristic solubility limit of Fe in NiFe LDH materials. Here our synthesis process is varying from common hydrothermal thermal process, therefore, although there is a theoretical sequential precipitation of Ni/Fe, the precipitation process is completed in a very short time at the environment of excessive OH^-, so the former already uniformly dispersed Ni/Fe ions in the solution come into homogenously distributed solids accompanied by high-speed stirring. But even though there is some segregated FeOOH phase, it could not be detected by XRD. However, the corresponding structural changes could be observed by other techniques. The elemental distribution of Ni/Fe is checked by SEM-EDS at various regions and the STEM EDS mapping, although they are not precise to the atomic level due to the limitation of resolution, it has been proved at least that they are uniformly distributed in the nm level. It is similar for Raman spectra, there are no other Raman-active modes from expected FeOOH phase even for $NiFe_3$ LDH. Moreover, the bond length of Fe-O in NiFe LDH and γ-FeOOH are different, but here it is similar for all our NiFe LDHs revealed by EXAFS analysis. In general, even we cannot prove that there is no separate FeOOH phase for $NiFe_3$ LDH, the essential structure of Ni_3Fe LDH should be Fe incorporated into NiOOH structure, while $NiFe_3$ LDH is probably Ni incorporated into FeOOH matrix structure. Former work has confirmed that the cations (Ni and Fe) are not randomly distributed across the LDH layers and display increasing Fe clustering for higher iron contents. Therefore, there might be also the coexistence of different local Fe environment and from the essence of the structure, the intrinsic structural variation between these three NiFe LDHs is only the ratio of Fe-O-Fe to Fe-O-Ni. As we know, LDH is a term to describe the lamellar hydroxides, while the detailed local structure could vary. So, it might not be a big problem to name the amorphous monolayer $NiFe_3$ as LDH in a broad sense.

For the OER performance, the activity trend is Ni_3Fe LDH > Ni_3Fe_2 LDH > $NiFe_3$ LDH while the stability trend is reversed. Besides of the ECSA, the number of active sites of the catalyst, the intrinsic activity is dominated by the electronic structure. In situ techniques have proved the high valence Ni^{4+}, Fe^{4+} at OER conditions, here although we do not study the chemical states of metal at high potential, the characterization of pristine NiFe LDH has proved the larger proportion of Fe^{3+} with more oxygen coordination. The other perspective to understand the activity trend is the transition of intermediate species, including the potential for transition and the structure of species. Our in-situ Raman data confirm the existence of the active Ni(Fe)OOH phase, and their disorder levels are also different. It is a pity that we cannot distinguish the accurate potential for phase transition as the potential step is too huge, but our results could also help to make clear the structure for catalytic processes, in general, consistent with reported theory. But for stability, there are few targeted studies and mature theory to explain the mechanism. We found the metal dissolution is the main reason for their different degradation. The cyclic stability in different potential intervals verify the main degradation range for Ni_3Fe LDH is the OER process, which is correlated with the steady-state dissolution while the $NiFe_3$ LDH shows only some degradation when cycled in the nickel redox region, which is referred to as transient dissolution, possibly due to the surface reconstruction process. It could also be understood by the pristine atomic and electronic structure of NiFe LDHs: well-crystalline and ordered Ni_3Fe LDH with more coordinated oxygen atoms are, therefore, stable for the phase transition process, only exhibiting slight degradation during the nickel redox region. However, the $NiFe_3$ LDH with a lower order degree possess probably poor structural stability, and cannot transit back from the intermediate phase formed at high potential anymore, leading to a corresponding irreversible dynamic process and more metal dissolution. But these mechanisms are more kind of hypothesis which lack of direct evidence, like flow cell ICP-MS to observe the in-time metal dissolution and isotope labeling to track the OER pathways. It is believed that there will be more studies and reports on the stability mechanism of non-precious OER catalysts in the future.

According to the above understanding of the correlation between catalyst structure and performance, we adopted several different strategies to tune and optimize the structure of NiFe LDHs, aiming to get both active and durable catalyst for alkaline water electrolyzer. The ideal target is monolayer Ni_3Fe LDH, which possess the optimal composition for activity and layer structure for stability. Heat treatment of NiFe LDH leads to the shrinkage of layer spacing as reported, and the chemical states of oxygen and iron changed to some extent but not form monolayer structure and the corresponding OER performance do not improve. It could be deduced that the different results from our work reported is due to the material itself. The NiFe LDH prepared by different process could present distinct structural changes during heat treatment. From this perspective, this strategy does not meet our expectation. We also introduce formamide in the solvent to modify the layer structure. The experimental results confirm the less stacked layer possibly due to the incorporation of formamide into the LDH layers. The in-situ Raman spectra reveals lower potential for the presence of active species for Ni_3Fe LDH-F75, accounting for its better OER activity. Here we could observe this different potential, indicating the greater structural and performance variability of NiFe LDH in polar solvent formamide. Similarly, the incorporation of MnO_4^- ions into the interlayer of Ni_3Fe LDH could modify the layer structure by enlarging spacing and reducing stacked layers due to the larger ion radius, like kind of strain effect in the layer direction. XPS data shows it won't change the chemical states of metal sites, indicating there is no oxidation reaction during the synthesis process and charge transfer between the Ni/Fe in the matrix and interlayer MnO_4^- ions. Another trial is the hydrothermal treatment to increase the crystallinity. Theoretically, catalysts with higher crystallinity are usually less active and more stable. So here the time is set only 2 hours to get the balance of activity and stability for NiFe LDHs. We found this short-term hydrothermal process really increase the stability for these more crystalline nanocrystals, and this effect is more obvious for amorphous samples so we also confirm this approach in other systems. The initial amorphous NiFe molybdate and sulfide both transit into well-defined nanocrystals and exhibit enhanced OER stability, confirming it is a universal strategy enabling facile and cost-effective crystallization recovery from amorphous to well-fined nanocrystals as OER catalysts.

Chapter 7 Conclusion

The development of novel catalysts for AEM water electrolysis requires accurate characterization techniques to assess their performance. So first we use nickel electrode and Ni/NiO on a carbon support, as benchmark catalysts to develop a detailed test protocol leading to comparable results between different laboratories. By experimentally comparing various test components, we discussed their underlying effects on the evaluation of catalysts. For example, the oxidation current for carbon material as a counter electrode will overlap with nickel redox peak and total activity, so Pt should be used for the stability test. The dynamic changes of bubbles on the electrode during the long-term tests will lead to an unreliable evaluation of OER stability, thus the comparison of polarization curves during this process is more reliable. Based on our study, we recommend a set of protocols to fairly evaluate OER catalysts.

Then we focused on the synthesis of efficient and durable OER catalysts for AEM water electrolysis. The NiFe LDH electrocatalyst was obtained by a facile precipitation method, which exhibits compositional-dependent morphology, atomic and electronic structure. The correlation between the composition and structure of NiFe LDHs was investigated by various techniques. We found when more Fe is incorporated into LDHs, the lower crystallinity, stacked layers, the proportion of Fe^{3+} and number of coordinated oxygen atoms will be, while the disorder and the degree of amorphism increase. The multilayer Ni_3Fe LDH shows higher OER activity than other LDHs on RDE and also outperforms most reported NiFe LDHs. In addition, the single cell utilized Ni_3Fe LDH as anode catalysts for alkaline exchange membrane water electrolysis exhibits superior current density compared to its Ir-based counterpart, as well as a robust long-term stability. In-situ Raman shows that the dynamic self-constructed Ni(Fe)OOH phase is the actual active species of all NiFe LDHs at the OER potential, while the more disordered Ni_3Fe_2 and $NiFe_3$ LDHs show different intermediate structure and an irreversible phase transition during the potential change, the more ordered Ni_3Fe LDHs is able to return to the initial stage with good crystallinity. These results also imply the Ni_3Fe and $NiFe_3$ LDH possess different OER pathway and dissolution behavior. $NiFe_3$ LDH is conventional AEM with transient dissolution during the redox process while Ni_3Fe LDH is LOM mechanism with steady-state dissolution as OER occurs.

Thereafter, several strategies were adapted to improve the structure and OER stability of NiFe LDHs. Among them, heat treatment leads to the shrinkage of layer spacing but not improved the catalytical performance obviously. The assisting of formamide in solvent and the incorporated MnO_4^- into interlayers affect its layer structure, thus improve the OER stability to some extent. Hydrothermal treatment of NiFe LDHs could increase the crystallinity, making amorphous $NiFe_3$ LDH into crystalline nanoparticles. And this idea could be extended to Ni_3FeS and Ni_3FeMoO_4 system to obtain well defined nanocrystals as durable OER catalysts.

List of Abbreviations

AEM	Anion exchange membrane
CA	Chronoamperometry
CN	Coordination number
CV	Cyclic voltammetry
CP	Carbon paper
CNF	Carbon nanoframes
CQDs	Carbon quantum dots
DEMS	Differential electrochemical mass spectrometry
EDX	Energy dispersive X-ray
EIS	Electrochemical impedance spectroscopy
EELS	Electron energy loss spectroscopy
ECSA	Electrochemical surface area
ErGO	Electrochemically reduced graphene oxide
EXAFS	Extended X-ray absorption fine structure
GC	Glassy carbon
HAADF	High angle annular dark field
HRTEM	High resolution TEM
ICP-MS	Inductively coupled plasma mass spectrometry
ICP-OES	Inductively coupled optical emission spectroscopy
IR	Infrared spectroscopy
LSV	Linear sweep voltammetry
NF	Nickel foam
NiFe LDH	NiFe layered double hydroxide
OER	Oxygen evolution reaction
OCV	Open circuit voltage

PEM	Proton exchange membrane
PTL	Porous transport layer
RDE	Rotation disk electrode
SOE	Solid oxide electrolyzers
SEM	Scanning electron microscopy
STEM	Scanning transmission electron microscopy
SWNT	Single-walled carbon nanotubes
TEM	Transmission electron microscopy
TOF	Turnover frequency
XAS	X-ray absorption spectroscopy
XANES	X-ray absorption near edge structure
XPS	X-ray photoelectron spectroscopy
XRD	X-ray diffraction

Acknowledgements

First of all, I would like to thanks my supervisors for their support and help. Prof. Werner Lehnert not only offers his assistance with all kinds of issues from RWTH Aachen University from registration, courses to graduation, but also provides detailed and valuable comments and suggestions for my research progress. Moreover, like a family member, he gave me great tolerance and understanding for my mistakes, comforted and encouraged me when I was down, which made me deeply touched and encouraged in a foreign country. Dr. Shviro Meital gave me the most support in research, not only providing guidance on ideas, discussing the details of experiments, but even participating in some of the experiments by herself. During my PhD period, she is always proactive in discussing the results of experiments, giving advice and guidance, and revising reports and papers. I would also like to thanks Dr. Marcelo Carmo and Dr. Shviro Meital for offering me the opportunity to work in Forschungszentrum Jülich.

Likewise, I would also like to thank my colleagues in EEL department: Daniel Holtz helps to deal with the daily issues in the labs. Birgit Schumacher helps to do SEM tests. Denise Beate Günther, Stefanie Fisher and Norbert Commerscheidt also supports my work in labs. For fellow doctoral students Cina Karacan, Ali Karaca, Park Seoungen, Nikolai Utsch and Irina Galkina express their goodwill when I was just starting out. Chang Liu and Lu Xia gave a lot of guidance and help in both study and life. As well as other colleagues, Osmando Lopes, Ilias Stamatelos, Tereza Bautkinova, Akhila Nair and Kaiyue Lou, life is a road trip, and I'm grateful for this period together.

In addition to EEL group, there are many colleagues on other groups or institutes who have given me help. Sebastin Holtwelth and Edward Rauls are kind colleagues to offer all kinds of help. In BZL, Dr. Christian Rodenbücher taught me

how to work with the Raman spectrometer, Katja Klafki trained me the polishing machine and system, Yingzhen Chen helped me to use the infrared spectrometer. Andresas Everwand finished the XRD and SEM tests for me. Johannes Häusler helped with the synthesis in furnace. Dr. Anna Houben in IEK-4 offered me the access to XRD and got me trained. Dr. Heinrich Hartmann and Dr. Astrid Besmehn in ZEA-3 helped the test and analysis of XPS data. Dr. Volker Nischwitz in ZEA-3 assisted with the ICP tests. Baolin Wu in IEK-9 helped with some Raman tests.

There are also quite a few collaborators contributed to my PhD work so a great thanks for their cooperation and supports. Dr. Alaa Faid and Prof. Svein Sunde in Norwegian University of Science and Technology helped the in-situ Raman tests. Dr. Bruna Ferreira Gomes Lobo and Prof. Christina Roth from University of Bayreuth assisted the related XAS experiments. Dr. Moulay Sougrati and Dr. Lorenzo Stievano from University of Montpellier, France supported to get the Mössbauer spectroscopy. Additionally, I am grateful to the CHANNEL project for the financial support for my PhD research in Germany.

Finally, I would like to thank the friends who had fun with me in my daily life. Thanks to my family and my girlfriend, who becomes my wife during PhD period. Firm and wordless companionship and support is the longest love.

Time flies, and I may not have great achievement, but the PhD stage is still an important milestone in life. Thank you all as no piece of help is deserved, and I wish we all the best together. Thanks to the kindness, integrity and motivation that I have been sticking to and pursuing. I will continue to move forward and never stop.

References

(1) Yu, Z.; Duan, Y.; Feng, X.; Yu, X.; Gao, M.; Yu, S. Clean and Affordable Hydrogen Fuel from Alkaline Water Splitting : Past , Recent Progress , and Future Prospects. *Adv. Mater.* **2021**, *2007100*, 1–35. https://doi.org/10.1002/adma.202007100.

(2) Sapountzi, F. M.; Gracia, J. M.; Weststrate, C. J.; Fredriksson, H. O. A.; Niemantsverdriet, J. W. Electrocatalysts for the Generation of Hydrogen, Oxygen and Synthesis Gas. *Prog. Energy Combust. Sci.* **2017**, *58*, 1–35. https://doi.org/10.1016/j.pecs.2016.09.001.

(3) Suen, N. T.; Hung, S. F.; Quan, Q.; Zhang, N.; Xu, Y. J.; Chen, H. M. Electrocatalysis for the Oxygen Evolution Reaction: Recent Development and Future Perspectives. *Chem. Soc. Rev.* **2017**, *46* (2), 337–365. https://doi.org/10.1039/c6cs00328a.

(4) Hong, W. T.; Risch, M.; Stoerzinger, K. A.; Grimaud, A.; Suntivich, J.; Shao-Horn, Y. Toward the Rational Design of Non-Precious Transition Metal Oxides for Oxygen Electrocatalysis. *Energy Environ. Sci.* **2015**, *8* (5), 1404–1427. https://doi.org/10.1039/c4ee03869j.

(5) *Electrochemical Methods for Hydrogen Production*; Scott, K., Ed.; Energy and Environment Series; The Royal Society of Chemistry, 2020. https://doi.org/10.1039/9781788016049.

(6) Jens K. Nørskov, Felix Studt, F. A. and T. B. *Fundamental Concepts in Heterogeneous Catalysis*; John Wiley & Sons, 2015.

(7) McCrory, C. C. L.; Jung, S.; Peters, J. C.; Jaramillo, T. F. Benchmarking Heterogeneous Electrocatalysts for the Oxygen Evolution Reaction. *J. Am. Chem. Soc.* **2013**, *135* (45), 16977–16987. https://doi.org/10.1021/ja407115p.

(8) Shao, M.; Chang, Q.; Dodelet, J. P.; Chenitz, R. Recent Advances in Electrocatalysts for Oxygen Reduction Reaction. *Chem. Rev.* **2016**, *116* (6), 3594–3657. https://doi.org/10.1021/acs.chemrev.5b00462.

(9) Wu, Z.; Lu, X. F.; Zang, S.; Lou, X. W. Non ‐ Noble ‐ Metal ‐ Based Electrocatalysts toward the Oxygen Evolution Reaction. *Adv. Funct. Mater.* **2020**, 1910274. https://doi.org/10.1002/adfm.201910274.

(10) Zhou, W.; Zhou, M.; Hu, J.; Dong, H.; Ou, Y.; Yang, L.; Wei, X.; Xiao, P.; Zhang, Y. Shape-Controlled Synthesis of Ni Nanocrystals via a Wet-Chemistry Strategy and Their Shape-Dependent Catalytic Activity. *CrystEngComm* **2019**, *21* (9), 1416–1422. https://doi.org/10.1039/c8ce01915k.

(11) Sun, T.; Xu, L.; Yan, Y.; Zakhidov, A. A.; Baughman, R. H.; Chen, J. Ordered Mesoporous Nickel Sphere Arrays for Highly Efficient Electrocatalytic Water Oxidation. *ACS Catal.* **2016**, *6* (3), 1446–1450. https://doi.org/10.1021/acscatal.5b02571.

(12) Fominykh, K.; Feckl, J. M.; Sicklinger, J.; Döblinger, M.; Böcklein, S.; Ziegler, J.; Peter, L.; Rathousky, J.; Scheidt, E.-W.; Bein, T.; Fattakhova-Rohlfing, D. Ultrasmall Dispersible Crystalline Nickel Oxide Nanoparticles as High-Performance Catalysts for Electrochemical Water Splitting. *Adv. Funct. Mater.* **2014**, *24* (21), 3123–3129. https://doi.org/10.1002/adfm.201303600.

(13) Kim, B.; Oh, A.; Kabiraz, M. K.; Hong, Y.; Joo, J.; Baik, H.; Choi, S. I.; Lee, K. NiOOH Exfoliation-Free Nickel Octahedra as Highly Active and Durable Electrocatalysts Toward the Oxygen Evolution Reaction in an Alkaline Electrolyte. *ACS Appl Mater Interfaces* **2018**, *10* (12), 10115–10122. https://doi.org/10.1021/acsami.7b19457.

(14) Doyle, R. L.; Godwin, I. J.; Brandon, M. P.; Lyons, M. E. Redox and Electrochemical Water Splitting Catalytic Properties of Hydrated Metal Oxide Modified Electrodes. *Phys. Chem. Chem. Phys.* **2013**, *15* (33), 13737–13783. https://doi.org/10.1039/c3cp51213d.

(15) Dionigi, F.; Strasser, P. NiFe-Based (Oxy)Hydroxide Catalysts for Oxygen Evolution Reaction in Non-Acidic Electrolytes. *Adv. Energy Mater.* **2016**, *6* (23). https://doi.org/10.1002/aenm.201600621.

(16) Subbaraman, R.; Tripkovic, D.; Chang, K. C.; Strmcnik, D.; Paulikas, A. P.; Hirunsit, P.; Chan, M.; Greeley, J.; Stamenkovic, V.; Markovic, N. M. Trends in Activity for the Water Electrolyser Reactions on 3d M(Ni,Co,Fe,Mn) Hydr(Oxy)Oxide Catalysts. *Nat. Mater.* **2012**, *11* (6), 550–557. https://doi.org/10.1038/nmat3313.

(17) Jia, Y.; Zhang, L.; Gao, G.; Chen, H.; Wang, B.; Zhou, J.; Soo, M. T.; Hong, M.; Yan, X.; Qian, G.; Zou, J.; Du, A.; Yao, X. A Heterostructure Coupling of Exfoliated Ni-Fe Hydroxide Nanosheet and Defective Graphene as a Bifunctional Electrocatalyst for Overall Water Splitting. *Adv. Mater.* **2017**, *29* (17), 1700017. https://doi.org/10.1002/adma.201700017.

(18) Dai, L.; Chen, Z. N.; Li, L.; Yin, P.; Liu, Z.; Zhang, H. Ultrathin Ni(0)-Embedded Ni(OH)2 Heterostructured Nanosheets with Enhanced Electrochemical Overall Water Splitting. *Adv. Mater.* **2020**, e1906915. https://doi.org/10.1002/adma.201906915.

(19) He, Q.; Wan, Y.; Jiang, H.; Pan, Z.; Wu, C.; Wang, M.; Wu, X.; Ye, B.; Ajayan, P. M.; Song, L. Nickel Vacancies Boost Reconstruction in Nickel Hydroxide Electrocatalyst. *ACS Energy Lett.* **2018**, *3* (6), 1373–1380. https://doi.org/10.1021/acsenergylett.8b00515.

(20) Gorlin, M.; Ferreira de Araujo, J.; Schmies, H.; Bernsmeier, D.; Dresp, S.; Gliech, M.; Jusys, Z.; Chernev, P.; Kraehnert, R.; Dau, H.; Strasser, P. Tracking Catalyst Redox States and Reaction Dynamics in Ni-Fe Oxyhydroxide Oxygen Evolution Reaction Electrocatalysts: The Role of Catalyst Support and Electrolyte PH. *J. Am. Chem. Soc.* **2017**, *139* (5), 2070–2082. https://doi.org/10.1021/jacs.6b12250.

(21) Tripkovic, V.; Hansen, H. A.; Vegge, T. From 3D to 2D Co and Ni Oxyhydroxide Catalysts: Elucidation of the Active Site and Influence of Doping on the Oxygen Evolution Activity. *ACS Catal.* **2017**, *7* (12), 8558–8571. https://doi.org/10.1021/acscatal.7b02712.

(22) Enman, L. J.; Burke, M. S.; Batchellor, A. S.; Boettcher, S. W. Effects of Intentionally Incorporated Metal Cations on the Oxygen Evolution Electrocatalytic Activity of Nickel (Oxy)Hydroxide in Alkaline Media. *ACS Catal.* **2016**, *6* (4), 2416–2423. https://doi.org/10.1021/acscatal.5b02924.

(23) Trotochaud, L.; Young, S. L.; Ranney, J. K.; Boettcher, S. W. Nickel-Iron Oxyhydroxide Oxygen-Evolution Electrocatalysts: The Role of Intentional and Incidental Iron Incorporation. *J. Am. Chem. Soc.* **2014**, *136* (18), 6744–6753. https://doi.org/10.1021/ja502379c.

(24) Klaus, S.; Cai, Y.; Louie, M. W.; Trotochaud, L.; Bell, A. T. Effects of Fe Electrolyte Impurities on Ni(OH)2/NiOOH Structure and Oxygen Evolution Activity. *J. Phys. Chem. C* **2015**, *119* (13), 7243–7254. https://doi.org/10.1021/acs.jpcc.5b00105.

(25) Louie, M. W.; Bell, A. T. An Investigation of Thin-Film Ni-Fe Oxide Catalysts for the Electrochemical Evolution of Oxygen. *J. Am. Chem. Soc.* **2013**, *135* (33), 12329–12337. https://doi.org/10.1021/ja405351s.

(26) Gong, M.; Dai, H. A Mini Review of NiFe-Based Materials as Highly Active Oxygen Evolution Reaction Electrocatalysts. *Nano Res.* **2014**, *8* (1), 23–39. https://doi.org/10.1007/s12274-014-0591-z.

(27) Zhu, K.; Zhu, X.; Yang, W. Application of In Situ Techniques for the Characterization of NiFe-Based Oxygen Evolution Reaction (OER) Electrocatalysts. *Angew Chem Int Ed Engl* **2019**, *58* (5), 1252–1265. https://doi.org/10.1002/anie.201802923.

(28) Görlin, M.; Chernev, P.; De Araújo, J. F.; Reier, T.; Dresp, S.; Paul, B.; Krähnert, R.; Dau, H.; Strasser, P. Oxygen Evolution Reaction Dynamics, Faradaic Charge Efficiency, and the Active Metal Redox States of Ni-Fe Oxide Water Splitting Electrocatalysts. *J. Am. Chem. Soc.* **2016**, *138* (17), 5603–5614. https://doi.org/10.1021/jacs.6b00332.

(29) Francas, L.; Corby, S.; Selim, S.; Lee, D.; Mesa, C. A.; Godin, R.; Pastor, E.; Stephens, I. E. L.; Choi, K. S.; Durrant, J. R. Spectroelectrochemical Study of Water Oxidation on Nickel and Iron Oxyhydroxide Electrocatalysts. *Nat. Commun.*

2019, *10* (1), 5208. https://doi.org/10.1038/s41467-019-13061-0.

(30) Mohammed-Ibrahim, J. A Review on NiFe-Based Electrocatalysts for Efficient Alkaline Oxygen Evolution Reaction. *J. Power Sources* **2019**. https://doi.org/10.1016/j.jpowsour.2019.227375.

(31) Friebel, D.; Louie, M. W.; Bajdich, M.; Sanwald, K. E.; Cai, Y.; Wise, A. M.; Cheng, M. J.; Sokaras, D.; Weng, T. C.; Alonso-Mori, R.; Davis, R. C.; Bargar, J. R.; Norskov, J. K.; Nilsson, A.; Bell, A. T. Identification of Highly Active Fe Sites in (Ni,Fe)OOH for Electrocatalytic Water Splitting. *J. Am. Chem. Soc.* **2015**, *137* (3), 1305–1313. https://doi.org/10.1021/ja511559d.

(32) Stevens, M. B.; Trang, C. D. M.; Enman, L. J.; Deng, J.; Boettcher, S. W. Reactive Fe-Sites in Ni/Fe (Oxy)Hydroxide Are Responsible for Exceptional Oxygen Electrocatalysis Activity. *J. Am. Chem. Soc.* **2017**, *139* (33), 11361–11364. https://doi.org/10.1021/jacs.7b07117.

(33) Xiao, H.; Shin, H.; Goddard, W. A. Synergy between Fe and Ni in the Optimal Performance of (Ni, Fe) OOH Catalysts for the Oxygen Evolution Reaction. *Proc. Natl. Acad. Sci.* **2018**, *115* (23), 5872–5877.

(34) Li, N.; Bediako, D. K.; Hadt, R. G.; Hayes, D.; Kempa, T. J.; von Cube, F.; Bell, D. C.; Chen, L. X.; Nocera, D. G. Influence of Iron Doping on Tetravalent Nickel Content in Catalytic Oxygen Evolving Films. *Proc. Natl. Acad. Sci.* **2017**, *114* (7), 1486–1491. https://doi.org/10.1073/pnas.1620787114.

(35) Goldsmith, Z. K.; Harshan, A. K.; Gerken, J. B.; Vörös, M.; Galli, G.; Stahl, S. S.; Hammes-Schiffer, S. Characterization of NiFe Oxyhydroxide Electrocatalysts by Integrated Electronic Structure Calculations and Spectroelectrochemistry. *Proc. Natl. Acad. Sci. U. S. A.* **2017**, *114* (12), 3050–3055. https://doi.org/10.1073/pnas.1702081114.

(36) Zheng, X.; Zhang, B.; De Luna, P.; Liang, Y.; Comin, R.; Voznyy, O.; Han, L.; Garcia de Arquer, F. P.; Liu, M.; Dinh, C. T.; Regier, T.; Dynes, J. J.; He, S.; Xin, H. L.; Peng, H.; Prendergast, D.; Du, X.; Sargent, E. H. Theory-Driven Design of High-Valence Metal Sites for Water Oxidation Confirmed Using in Situ Soft X-Ray Absorption. *Nat. Chem.* **2018**, *10* (2), 149–154. https://doi.org/10.1038/nchem.2886.

(37) Hunter, B. M.; Gray, H. B.; Muller, A. M. Earth-Abundant Heterogeneous Water Oxidation Catalysts. *Chem. Rev.* **2016**, *116* (22), 14120–14136. https://doi.org/10.1021/acs.chemrev.6b00398.

(38) Fabbri, E.; Nachtegaal, M.; Binninger, T.; Cheng, X.; Kim, B. J.; Durst, J.; Bozza, F.; Graule, T.; Schaublin, R.; Wiles, L.; Pertoso, M.; Danilovic, N.; Ayers, K. E.; Schmidt, T. J. Dynamic Surface Self-Reconstruction Is the Key of Highly Active Perovskite Nano-Electrocatalysts for Water Splitting. *Nat. Mater.* **2017**.

https://doi.org/10.1038/nmat4938.

(39) Suntivich, J.; May, K. J.; Gasteiger, H. A.; Goodenough, J. B.; Shao-Horn, Y. A Perovskite Oxide Optimized for Oxygen Evolution Catalysis from Molecular Orbital Principles. *Science* **2011**, *334* (6061), 1383–1385. https://doi.org/10.1126/science.1212858.

(40) Suntivich, J.; Gasteiger, H. A.; Yabuuchi, N.; Nakanishi, H.; Goodenough, J. B.; Shao-Horn, Y. Design Principles for Oxygen-Reduction Activity on Perovskite Oxide Catalysts for Fuel Cells and Metal-Air Batteries. *Nat. Chem.* **2011**, *3* (7), 546–550. https://doi.org/10.1038/nchem.1069.

(41) Han, B.; Stoerzinger, K. A.; Tileli, V.; Gamalski, A. D.; Stach, E. A.; Shao-Horn, Y. Nanoscale Structural Oscillations in Perovskite Oxides Induced by Oxygen Evolution. *Nat. Mater.* **2017**, *16* (1), 121–126. https://doi.org/10.1038/nmat4764.

(42) Lee, J. G.; Hwang, J.; Hwang, H. J.; Jeon, O. S.; Jang, J.; Kwon, O.; Lee, Y.; Han, B.; Shul, Y. G. A New Family of Perovskite Catalysts for Oxygen-Evolution Reaction in Alkaline Media: BaNiO3 and BaNi(0.83)O(2.5). *J. Am. Chem. Soc.* **2016**, *138* (10), 3541–3547. https://doi.org/10.1021/jacs.6b00036.

(43) Bak, J.; Bin Bae, H.; Chung, S. Y. Atomic-Scale Perturbation of Oxygen Octahedra via Surface Ion Exchange in Perovskite Nickelates Boosts Water Oxidation. *Nat. Commun.* **2019**, *10* (1), 2713. https://doi.org/10.1038/s41467-019-10838-1.

(44) Suntivich, J.; Hong, W. T.; Lee, Y.-L.; Rondinelli, J. M.; Yang, W.; Goodenough, J. B.; Dabrowski, B.; Freeland, J. W.; Shao-Horn, Y. Estimating Hybridization of Transition Metal and Oxygen States in Perovskites from O K-Edge X-Ray Absorption Spectroscopy. *J. Phys. Chem. C* **2014**, *118* (4), 1856–1863. https://doi.org/10.1021/jp410644j.

(45) Hong, W. T.; Stoerzinger, K. A.; Lee, Y.-L.; Giordano, L.; Grimaud, A.; Johnson, A. M.; Hwang, J.; Crumlin, E. J.; Yang, W.; Shao-Horn, Y. Charge-Transfer-Energy-Dependent Oxygen Evolution Reaction Mechanisms for Perovskite Oxides. *Energy Environ. Sci.* **2017**, *10* (10), 2190–2200. https://doi.org/10.1039/c7ee02052j.

(46) Grimaud, A.; May, K. J.; Carlton, C. E.; Lee, Y. L.; Risch, M.; Hong, W. T.; Zhou, J.; Shao-Horn, Y. Double Perovskites as a Family of Highly Active Catalysts for Oxygen Evolution in Alkaline Solution. *Nat. Commun.* **2013**, *4*, 2439. https://doi.org/10.1038/ncomms3439.

(47) Grimaud, A.; Diaz-Morales, O.; Han, B.; Hong, W. T.; Lee, Y. L.; Giordano, L.; Stoerzinger, K. A.; Koper, M. T. M.; Shao-Horn, Y. Activating Lattice Oxygen Redox Reactions in Metal Oxides to Catalyse Oxygen Evolution. *Nat. Chem.* **2017**, *9* (5), 457–465. https://doi.org/10.1038/nchem.2695.

(48) Petrie, J. R.; Cooper, V. R.; Freeland, J. W.; Meyer, T. L.; Zhang, Z.; Lutterman,

D. A.; Lee, H. N. Enhanced Bifunctional Oxygen Catalysis in Strained $LaNiO_3$ Perovskites. *J. Am. Chem. Soc.* **2016**, *138* (8), 2488–2491. https://doi.org/10.1021/jacs.5b11713.

(49) Carta, D.; Casula, M. F.; Falqui, A.; Loche, D.; Mountjoy, G.; Sangregorio, C.; Corrias, A. A Structural and Magnetic Investigation of the Inversion Degree in Ferrite Nanocrystals MFe_2O_4 (M = Mn, Co, Ni). *J. Phys. Chem. C* **2009**, *113* (20), 8606–8615.

(50) Wei, C.; Feng, Z.; Baisariyev, M.; Yu, L.; Zeng, L.; Wu, T.; Zhao, H.; Huang, Y.; Bedzyk, M. J.; Sritharan, T.; Xu, Z. J. Valence Change Ability and Geometrical Occupation of Substitution Cations Determine the Pseudocapacitance of Spinel Ferrite XFe_2O_4(X = Mn, Co, Ni, Fe). *Chem. Mater.* **2016**, *28* (12), 4129–4133. https://doi.org/10.1021/acs.chemmater.6b00713.

(51) Wu, G.; Wang, J.; Ding, W.; Nie, Y.; Li, L.; Qi, X.; Chen, S.; Wei, Z. A Strategy to Promote the Electrocatalytic Activity of Spinels for Oxygen Reduction by Structure Reversal. *Angew Chem Int Ed Engl* **2016**, *55* (4), 1340–1344. https://doi.org/10.1002/anie.201508809.

(52) Liu, Y.; Ying, Y.; Fei, L.; Liu, Y.; Hu, Q.; Zhang, G.; Pang, S. Y.; Lu, W.; Mak, C. L.; Luo, X.; Zhou, L.; Wei, M.; Huang, H. Valence Engineering via Selective Atomic Substitution on Tetrahedral Sites in Spinel Oxide for Highly Enhanced Oxygen Evolution Catalysis. *J. Am. Chem. Soc.* **2019**, *141* (20), 8136–8145. https://doi.org/10.1021/jacs.8b13701.

(53) Wei, C.; Feng, Z.; Scherer, G. G.; Barber, J.; Shao-Horn, Y.; Xu, Z. J. Cations in Octahedral Sites: A Descriptor for Oxygen Electrocatalysis on Transition-Metal Spinels. *Adv. Mater.* **2017**, *29* (23). https://doi.org/10.1002/adma.201606800.

(54) Zhou, Y.; Sun, S.; Song, J.; Xi, S.; Chen, B.; Du, Y.; Fisher, A. C.; Cheng, F.; Wang, X.; Zhang, H.; Xu, Z. J. Enlarged CoO Covalency in Octahedral Sites Leading to Highly Efficient Spinel Oxides for Oxygen Evolution Reaction. *Adv. Mater.* **2018**, *30* (32), e1802912. https://doi.org/10.1002/adma.201802912.

(55) Wang, X. T.; Ouyang, T.; Wang, L.; Zhong, J. H.; Liu, Z. Q. Surface Reorganization on Electrochemically-Induced Zn-Ni-Co Spinel Oxides for Enhanced Oxygen Electrocatalysis. *Angew Chem Int Ed Engl* **2020**. https://doi.org/10.1002/anie.202000690.

(56) Hsu, C. S.; Suen, N. T.; Hsu, Y. Y.; Lin, H. Y.; Tung, C. W.; Liao, Y. F.; Chan, T. S.; Sheu, H. S.; Chen, S. Y.; Chen, H. M. Valence- and Element-Dependent Water Oxidation Behaviors: In Situ X-Ray Diffraction, Absorption and Electrochemical Impedance Spectroscopies. *Phys. Chem. Chem. Phys.* **2017**, *19* (13), 8681–8693. https://doi.org/10.1039/c6cp07630k.

(57) Kim, T. W.; Woo, M. A.; Regis, M.; Choi, K. S. Electrochemical Synthesis of Spinel

Type ZnCo2O4 Electrodes for Use as Oxygen Evolution Reaction Catalysts. *J. Phys. Chem. Lett.* **2014**, *5* (13), 2370–2374. https://doi.org/10.1021/jz501077u.

(58) Wang, H. Y.; Hung, S. F.; Chen, H. Y.; Chan, T. S.; Chen, H. M.; Liu, B. In Operando Identification of Geometrical-Site-Dependent Water Oxidation Activity of Spinel Co3O4. *J. Am. Chem. Soc.* **2016**, *138* (1), 36–39. https://doi.org/10.1021/jacs.5b10525.

(59) Schwanke, C.; Stein, H. S.; Xi, L.; Sliozberg, K.; Schuhmann, W.; Ludwig, A.; Lange, K. M. Correlating Oxygen Evolution Catalysts Activity and Electronic Structure by a High-Throughput Investigation of Ni1-y-ZFeyCrzOx. *Sci. Rep.* **2017**, *7*, 44192. https://doi.org/10.1038/srep44192.

(60) Li, J.; Chu, D.; Dong, H.; Baker, D. R.; Jiang, R. Boosted Oxygen Evolution Reactivity by Igniting Double Exchange Interaction in Spinel Oxides. *J. Am. Chem. Soc.* **2020**, *142* (1), 50–54. https://doi.org/10.1021/jacs.9b10882.

(61) Yu, F.; Zhou, H.; Huang, Y.; Sun, J.; Qin, F.; Bao, J.; Goddard, W. A.; Chen, S.; Ren, Z. High-Performance Bifunctional Porous Non-Noble Metal Phosphide Catalyst for Overall Water Splitting. *Nat. Commun.* **2018**, *9* (1), 1–9. https://doi.org/10.1038/s41467-018-04746-z.

(62) Dionigi, F.; Zhu, J.; Zeng, Z.; Merzdorf, T.; Sarodnik, H.; Gliech, M.; Pan, L.; Li, W.; Greeley, J.; Strasser, P. Intrinsic Electrocatalytic Activity for Oxygen Evolution of Crystalline 3d ‐ Transition Metal Layered Double Hydroxides. *Angew. Chemie* **2021**, *133* (26), 14567–14578. https://doi.org/10.1002/ange.202100631.

(63) Xiang, Q.; Li, F.; Chen, W.; Ma, Y.; Wu, Y.; Gu, X.; Qin, Y.; Tao, P.; Song, C.; Shang, W.; Zhu, H.; Deng, T.; Wu, J. In Situ Vertical Growth of Fe–Ni Layered Double-Hydroxide Arrays on Fe–Ni Alloy Foil: Interfacial Layer Enhanced Electrocatalyst with Small Overpotential for Oxygen Evolution Reaction. *ACS Energy Lett.* **2018**, *3* (10), 2357–2365. https://doi.org/10.1021/acsenergylett.8b01466.

(64) Stern, L.-A.; Feng, L.; Song, F.; Hu, X. Ni2P as a Janus Catalyst for Water Splitting: The Oxygen Evolution Activity of Ni2P Nanoparticles. *Energy Environ. Sci.* **2015**, *8* (8), 2347–2351. https://doi.org/10.1039/c5ee01155h.

(65) You, B.; Jiang, N.; Sheng, M.; Bhushan, M. W.; Sun, Y. Hierarchically Porous Urchin-Like Ni2P Superstructures Supported on Nickel Foam as Efficient Bifunctional Electrocatalysts for Overall Water Splitting. *ACS Catal.* **2015**, *6* (2), 714–721. https://doi.org/10.1021/acscatal.5b02193.

(66) You, B.; Sun, Y. Hierarchically Porous Nickel Sulfide Multifunctional Superstructures. *Adv. Energy Mater.* **2016**, *6* (7). https://doi.org/10.1002/aenm.201502333.

(67) Chen, P.; Zhou, T.; Zhang, M.; Tong, Y.; Zhong, C.; Zhang, N.; Zhang, L.; Wu, C.;

Xie, Y. 3D Nitrogen-Anion-Decorated Nickel Sulfides for Highly Efficient Overall Water Splitting. *Adv. Mater.* **2017**, *29* (30). https://doi.org/10.1002/adma.201701584.

(68) Zhang, J.; Wang, Y.; Zhang, C.; Gao, H.; Lv, L.; Han, L.; Zhang, Z. Self-Supported Porous NiSe2 Nanowrinkles as Efficient Bifunctional Electrocatalysts for Overall Water Splitting. *ACS Sustain. Chem. Eng.* **2017**, *6* (2), 2231–2239. https://doi.org/10.1021/acssuschemeng.7b03657.

(69) Dinh, K. N.; Sun, Y.; Pei, Z.; Yuan, Z.; Suwardi, A.; Huang, Q.; Liao, X.; Wang, Z.; Chen, Y.; Yan, Q. Electronic Modulation of Nickel Disulfide toward Efficient Water Electrolysis. *Small* **2020**, e1905885. https://doi.org/10.1002/smll.201905885.

(70) Gao, M.; Sheng, W.; Zhuang, Z.; Fang, Q.; Gu, S.; Jiang, J.; Yan, Y. Efficient Water Oxidation Using Nanostructured Alpha-Nickel-Hydroxide as an Electrocatalyst. *J. Am. Chem. Soc.* **2014**, *136* (19), 7077–7084. https://doi.org/10.1021/ja502128j.

(71) Wang, J.; Ji, L.; Chen, Z. In Situ Rapid Formation of a Nickel–Iron-Based Electrocatalyst for Water Oxidation. *ACS Catal.* **2016**, *6* (10), 6987–6992. https://doi.org/10.1021/acscatal.6b01837.

(72) Yang, H.; Liu, Y.; Luo, S.; Zhao, Z.; Wang, X.; Luo, Y.; Wang, Z.; Jin, J.; Ma, J. Lateral-Size-Mediated Efficient Oxygen Evolution Reaction: Insights into the Atomically Thin Quantum Dot Structure of NiFe2O4. *ACS Catal.* **2017**, *7* (8), 5557–5567. https://doi.org/10.1021/acscatal.7b00007.

(73) Dong, C.; Kou, T.; Gao, H.; Peng, Z.; Zhang, Z. Eutectic-Derived Mesoporous Ni-Fe-O Nanowire Network Catalyzing Oxygen Evolution and Overall Water Splitting. *Adv. Energy Mater.* **2018**, *8* (5). https://doi.org/10.1002/aenm.201701347.

(74) Zhong, D.; Zhang, L.; Li, C.; Li, D.; Wei, C.; Zhao, Q.; Li, J.; Gong, J. Nanostructured NiFe (Oxy)Hydroxide with Easily Oxidized Ni towards Efficient Oxygen Evolution Reactions. *J. Mater. Chem. A* **2018**, *6* (35), 16810–16817. https://doi.org/10.1039/c8ta04721a.

(75) Liu, K.; Wang, F.; He, P.; Shifa, T. A.; Wang, Z.; Cheng, Z.; Zhan, X.; He, J. The Role of Active Oxide Species for Electrochemical Water Oxidation on the Surface of 3d-Metal Phosphides. *Adv. Energy Mater.* **2018**, *8* (15). https://doi.org/10.1002/aenm.201703290.

(76) Qian, M.; Cui, S.; Jiang, D.; Zhang, L.; Du, P. Highly Efficient and Stable Water-Oxidation Electrocatalysis with a Very Low Overpotential Using FeNiP Substitutional-Solid-Solution Nanoplate Arrays. *Adv. Mater.* **2017**, *29* (46). https://doi.org/10.1002/adma.201704075.

(77) Song, B.; Li, K.; Yin, Y.; Wu, T.; Dang, L.; Cabán-Acevedo, M.; Han, J.; Gao, T.; Wang, X.; Zhang, Z.; Schmidt, J. R.; Xu, P.; Jin, S. Tuning Mixed Nickel Iron

Phosphosulfide Nanosheet Electrocatalysts for Enhanced Hydrogen and Oxygen Evolution. *ACS Catal.* **2017**, *7* (12), 8549–8557. https://doi.org/10.1021/acscatal.7b02575.

(78) Zhang, X.; Xu, H.; Li, X.; Li, Y.; Yang, T.; Liang, Y. Facile Synthesis of Nickel–Iron/Nanocarbon Hybrids as Advanced Electrocatalysts for Efficient Water Splitting. *ACS Catal.* **2015**, *6* (2), 580–588. https://doi.org/10.1021/acscatal.5b02291.

(79) Zhang, Y.; Xia, X.; Cao, X.; Zhang, B.; Tiep, N. H.; He, H.; Chen, S.; Huang, Y.; Fan, H. J. Ultrafine Metal Nanoparticles/N-Doped Porous Carbon Hybrids Coated on Carbon Fibers as Flexible and Binder-Free Water Splitting Catalysts. *Adv. Energy Mater.* **2017**, *7* (15). https://doi.org/10.1002/aenm.201700220.

(80) Yu, L.; Zhou, H.; Sun, J.; Qin, F.; Yu, F.; Bao, J.; Yu, Y.; Chen, S.; Ren, Z. Cu Nanowires Shelled with NiFe Layered Double Hydroxide Nanosheets as Bifunctional Electrocatalysts for Overall Water Splitting. *Energy Environ. Sci.* **2017**, *10* (8), 1820–1827. https://doi.org/10.1039/c7ee01571b.

(81) Yu, L.; Zhou, H.; Sun, J.; Mishra, I. K.; Luo, D.; Yu, F.; Yu, Y.; Chen, S.; Ren, Z. Amorphous NiFe Layered Double Hydroxide Nanosheets Decorated on 3D Nickel Phosphide Nanoarrays: A Hierarchical Core–Shell Electrocatalyst for Efficient Oxygen Evolution. *J. Mater. Chem. A* **2018**, *6* (28), 13619–13623. https://doi.org/10.1039/c8ta02967a.

(82) Zhang, G.; Yuan, J.; Liu, Y.; Lu, W.; Fu, N.; Li, W.; Huang, H. Boosting the Oxygen Evolution Reaction in Non-Precious Catalysts by Structural and Electronic Engineering. *J. Mater. Chem. A* **2018**, *6* (22), 10253–10263. https://doi.org/10.1039/c8ta02542h.

(83) Nai, J.; Lu, Y.; Yu, L.; Wang, X.; Lou, X. W. D. Formation of Ni-Fe Mixed Diselenide Nanocages as a Superior Oxygen Evolution Electrocatalyst. *Adv. Mater.* **2017**, *29* (41). https://doi.org/10.1002/adma.201703870.

(84) Xu, X.; Song, F.; Hu, X. A Nickel Iron Diselenide-Derived Efficient Oxygen-Evolution Catalyst. *Nat. Commun.* **2016**, *7*, 12324. https://doi.org/10.1038/ncomms12324.

(85) Bae, S.-H.; Kim, J.-E.; Randriamahazaka, H.; Moon, S.-Y.; Park, J.-Y.; Oh, I.-K. Seamlessly Conductive 3D Nanoarchitecture of Core-Shell Ni-Co Nanowire Network for Highly Efficient Oxygen Evolution. *Adv. Energy Mater.* **2017**, *7* (1). https://doi.org/10.1002/aenm.201601492.

(86) Liang, H.; Gandi, A. N.; Anjum, D. H.; Wang, X.; Schwingenschlogl, U.; Alshareef, H. N. Plasma-Assisted Synthesis of NiCoP for Efficient Overall Water Splitting. *Nano Lett* **2016**, *16* (12), 7718–7725. https://doi.org/10.1021/acs.nanolett.6b03803.

(87) Hu, E.; Feng, Y.; Nai, J.; Zhao, D.; Hu, Y.; Lou, X. W. Construction of Hierarchical Ni–Co–P Hollow Nanobricks with Oriented Nanosheets for Efficient Overall Water Splitting. *Energy Environ. Sci.* **2018**, *11* (4), 872–880. https://doi.org/10.1039/c8ee00076j.

(88) Wang, C.; Jiang, J.; Ding, T.; Chen, G.; Xu, W.; Yang, Q. Monodisperse Ternary NiCoP Nanostructures as a Bifunctional Electrocatalyst for Both Hydrogen and Oxygen Evolution Reactions with Excellent Performance. *Adv. Mater. Interfaces* **2016**, *3* (4). https://doi.org/10.1002/admi.201500454.

(89) Zhang, P.; Li, L.; Nordlund, D.; Chen, H.; Fan, L.; Zhang, B.; Sheng, X.; Daniel, Q.; Sun, L. Dendritic Core-Shell Nickel-Iron-Copper Metal/Metal Oxide Electrode for Efficient Electrocatalytic Water Oxidation. *Nat. Commun.* **2018**, *9* (1), 381. https://doi.org/10.1038/s41467-017-02429-9.

(90) Chen, M.; Lu, S.; Fu, X. Z.; Luo, J. L. Core–Shell Structured NiFeSn@NiFe (Oxy)Hydroxide Nanospheres from an Electrochemical Strategy for Electrocatalytic Oxygen Evolution Reaction. *Adv. Sci.* **2020**, *7* (10). https://doi.org/10.1002/advs.201903777.

(91) Tavakkoli, M.; Nosek, M.; Sainio, J.; Davodi, F.; Kallio, T.; Joensuu, P. M.; Laasonen, K. Functionalized Carbon Nanotubes with Ni(II) Bipyridine Complexes as Efficient Catalysts for the Alkaline Oxygen Evolution Reaction. *ACS Catal.* **2017**, *7* (12), 8033–8041. https://doi.org/10.1021/acscatal.7b02878.

(92) Zhu, Y.; Chen, G.; Zhong, Y.; Chen, Y.; Ma, N.; Zhou, W.; Shao, Z. A Surface-Modified Antiperovskite as an Electrocatalyst for Water Oxidation. *Nat. Commun.* **2018**, *9* (1), 2326. https://doi.org/10.1038/s41467-018-04682-y.

(93) Xu, H.; Shi, Z. X.; Tong, Y. X.; Li, G. R. Porous Microrod Arrays Constructed by Carbon-Confined NiCo@NiCoO2 Core@Shell Nanoparticles as Efficient Electrocatalysts for Oxygen Evolution. *Adv. Mater.* **2018**, *30* (21), e1705442. https://doi.org/10.1002/adma.201705442.

(94) Song, H. J.; Yoon, H.; Ju, B.; Lee, G.-H.; Kim, D.-W. 3D Architectures of Quaternary Co-Ni-S-P/Graphene Hybrids as Highly Active and Stable Bifunctional Electrocatalysts for Overall Water Splitting. *Adv. Energy Mater.* **2018**, *8* (33). https://doi.org/10.1002/aenm.201802319.

(95) Qu, S.; Chen, W.; Yu, J.; Chen, G.; Zhang, R.; Chu, S.; Huang, J.; Wang, X.; Li, C.; Ostrikov, K. (Ken). Cross-Linked Trimetallic Nanopetals for Electrocatalytic Water Splitting. *J. Power Sources* **2018**, *390* (January), 224–233. https://doi.org/10.1016/j.jpowsour.2018.04.061.

(96) Li, H.; Chen, S.; Zhang, Y.; Zhang, Q.; Jia, X.; Zhang, Q.; Gu, L.; Sun, X.; Song, L.; Wang, X. Systematic Design of Superaerophobic Nanotube-Array Electrode Comprised of Transition-Metal Sulfides for Overall Water Splitting. *Nat. Commun.*

2018, *9* (1), 2452. https://doi.org/10.1038/s41467-018-04888-0.

(97) Xiaowen Yu, Miao Zhang, Wenjing Yuan, and G. S. High-Performance Three-Dimensional Ni-Fe Layered Double Hydroxide/Graphene Electrode for Water Oxidation. *J. Mater. Chem. A* **2015**, No. 3, 6921–6928. https://doi.org/10.1039/x0xx00000x.

(98) Wang, Q.; Shang, L.; Shi, R.; Zhang, X.; Zhao, Y.; Waterhouse, G. I. N.; Wu, L. Z.; Tung, C. H.; Zhang, T. NiFe Layered Double Hydroxide Nanoparticles on Co,N-Codoped Carbon Nanoframes as Efficient Bifunctional Catalysts for Rechargeable Zinc–Air Batteries. *Adv. Energy Mater.* **2017**, *7* (21), 1–7. https://doi.org/10.1002/aenm.201700467.

(99) Liu, H.; Zhou, J.; Wu, C.; Wang, C.; Zhang, Y.; Liu, D.; Lin, Y.; Jiang, H.; Song, L. Integrated Flexible Electrode for Oxygen Evolution Reaction: Layered Double Hydroxide Coupled with Single-Walled Carbon Nanotubes Film. *ACS Sustain. Chem. Eng.* **2018**, *6* (3), 2911–2915. https://doi.org/10.1021/acssuschemeng.8b00084.

(100) Yin, S.; Tu, W.; Sheng, Y.; Du, Y.; Kraft, M.; Borgna, A.; Xu, R. A Highly Efficient Oxygen Evolution Catalyst Consisting of Interconnected Nickel–Iron-Layered Double Hydroxide and Carbon Nanodomains. *Adv. Mater.* **2018**, *30* (5), 1–9. https://doi.org/10.1002/adma.201705106.

(101) Gao, Z. W.; Liu, J. Y.; Chen, X. M.; Zheng, X. L.; Mao, J.; Liu, H.; Ma, T.; Li, L.; Wang, W. C.; Du, X. W. Engineering NiO/NiFe LDH Intersection to Bypass Scaling Relationship for Oxygen Evolution Reaction via Dynamic Tridimensional Adsorption of Intermediates. *Adv. Mater.* **2019**, *31* (11), 1–8. https://doi.org/10.1002/adma.201804769.

(102) Song, F.; Hu, X. Exfoliation of Layered Double Hydroxides for Enhanced Oxygen Evolution Catalysis. *Nat. Commun.* **2014**, *5*, 4477. https://doi.org/10.1038/ncomms5477.

(103) Liang, H.; Meng, F.; Caban-Acevedo, M.; Li, L.; Forticaux, A.; Xiu, L.; Wang, Z.; Jin, S. Hydrothermal Continuous Flow Synthesis and Exfoliation of NiCo Layered Double Hydroxide Nanosheets for Enhanced Oxygen Evolution Catalysis. *Nano Lett.* **2015**, *15* (2), 1421–1427. https://doi.org/10.1021/nl504872s.

(104) Yu, L.; Yang, J. F.; Guan, B. Y.; Lu, Y.; Lou, X. W. D. Hierarchical Hollow Nanoprisms Based on Ultrathin Ni-Fe Layered Double Hydroxide Nanosheets with Enhanced Electrocatalytic Activity towards Oxygen Evolution. *Angew. Chemie Int. Ed.* **2018**, *57* (1), 172–176. https://doi.org/10.1002/anie.201710877.

(105) Zhang, J.; Yu, L.; Chen, Y.; Lu, X. F.; Gao, S.; Lou, X. W. D. Designed Formation of Double-Shelled Ni-Fe Layered-Double-Hydroxide Nanocages for Efficient Oxygen Evolution Reaction. *Adv. Mater.* **2020**, e1906432.

https://doi.org/10.1002/adma.201906432.

(106) Wang, Y.; Qiao, M.; Li, Y.; Wang, S. Tuning Surface Electronic Configuration of NiFe LDHs Nanosheets by Introducing Cation Vacancies (Fe or Ni) as Highly Efficient Electrocatalysts for Oxygen Evolution Reaction. *Small* **2018**, *14* (17), 1–6. https://doi.org/10.1002/smll.201800136.

(107) Lee, S.; Bai, L.; Hu, X. Deciphering Iron-Dependent Activity in Oxygen Evolution Catalyzed by Nickel-Iron Layered Double Hydroxide. *Angew Chem Int Ed Engl* **2020**, *59* (21), 8072–8077. https://doi.org/10.1002/anie.201915803.

(108) Zhou, D.; Wang, S.; Jia, Y.; Xiong, X.; Yang, H.; Liu, S.; Tang, J.; Zhang, J.; Liu, D.; Zheng, L.; Kuang, Y.; Sun, X.; Liu, B. NiFe Hydroxide Lattice Tensile Strain: Enhancement of Adsorption of Oxygenated Intermediates for Efficient Water Oxidation Catalysis. *Angew Chem Int Ed Engl* **2019**, *58* (3), 736–740. https://doi.org/10.1002/anie.201809689.

(109) Zhao, Y.; Zhang, X.; Jia, X.; Waterhouse, G. I. N.; Shi, R.; Zhang, X.; Zhan, F.; Tao, Y.; Wu, L.-Z.; Tung, C.-H.; O'Hare, D.; Zhang, T. Sub-3 Nm Ultrafine Monolayer Layered Double Hydroxide Nanosheets for Electrochemical Water Oxidation. *Adv. Energy Mater.* **2018**, *8* (18), 1703585. https://doi.org/10.1002/aenm.201703585.

(110) Zhang, X.; Zhao, Y.; Zhao, Y.; Shi, R.; Waterhouse, G. I. N.; Zhang, T. A Simple Synthetic Strategy toward Defect-Rich Porous Monolayer NiFe-Layered Double Hydroxide Nanosheets for Efficient Electrocatalytic Water Oxidation. *Adv. Energy Mater.* **2019**, *9* (24), 1–7. https://doi.org/10.1002/aenm.201900881.

(111) Li, P.; Duan, X.; Kuang, Y.; Li, Y.; Zhang, G.; Liu, W.; Sun, X. Tuning Electronic Structure of NiFe Layered Double Hydroxides with Vanadium Doping toward High Efficient Electrocatalytic Water Oxidation. *Adv. Energy Mater.* **2018**, *8* (15), 1–8. https://doi.org/10.1002/aenm.201703341.

(112) Cai, Z.; Zhou, D.; Wang, M.; Bak, S.-M.; Wu, Y.; Wu, Z.; Tian, Y.; Xiong, X.; Li, Y.; Liu, W.; Siahrostami, S.; Kuang, Y.; Yang, X.-Q.; Duan, H.; Feng, Z.; Wang, H.; Sun, X. Introducing Fe 2+ into Nickel-Iron Layered Double Hydroxide: Local Structure Modulated Water Oxidation Activity . *Angew. Chemie* **2018**, *130* (30), 9536–9540. https://doi.org/10.1002/ange.201804881.

(113) Zhang, J.; Liu, J.; Xi, L.; Yu, Y.; Chen, N.; Sun, S.; Wang, W.; Lange, K. M.; Zhang, B. Single-Atom Au/NiFe Layered Double Hydroxide Electrocatalyst: Probing the Origin of Activity for Oxygen Evolution Reaction. *J. Am. Chem. Soc.* **2018**, *140* (11), 3876–3879. https://doi.org/10.1021/jacs.8b00752.

(114) Zhang, B.; Zhu, C.; Wu, Z.; Stavitski, E.; Lui, Y. H.; Kim, T. H.; Liu, H.; Huang, L.; Luan, X.; Zhou, L.; Jiang, K.; Huang, W.; Hu, S.; Wang, H.; Francisco, J. S. Integrating Rh Species with NiFe-Layered Double Hydroxide for Overall Water

Splitting. *Nano Lett.* **2020**, *20* (1), 136–144. https://doi.org/10.1021/acs.nanolett.9b03460.

(115) Xia, Z.; Guo, S. Strain Engineering of Metal-Based Nanomaterials for Energy Electrocatalysis. *Chem. Soc. Rev.* **2019**, *48* (12), 3265–3278. https://doi.org/10.1039/c8cs00846a.

(116) Zhou, D.; Wang, S.; Jia, Y.; Xiong, X.; Yang, H.; Liu, S.; Tang, J.; Zhang, J.; Liu, D.; Zheng, L.; Kuang, Y.; Sun, X.; Liu, B. NiFe Hydroxide Lattice Tensile Strain: Enhancement of Adsorption of Oxygenated Intermediates for Efficient Water Oxidation Catalysis. *Angew. Chemie Int. Ed.* **2019**, *58* (3), 736–740. https://doi.org/10.1002/anie.201809689.

(117) Dionigi, F.; Zeng, Z.; Sinev, I.; Merzdorf, T.; Deshpande, S.; Lopez, M. B.; Kunze, S.; Zegkinoglou, I.; Sarodnik, H.; Fan, D.; Bergmann, A.; Drnec, J.; Araujo, J. F. de; Gliech, M.; Teschner, D.; Zhu, J.; Li, W. X.; Greeley, J.; Cuenya, B. R.; Strasser, P. In-Situ Structure and Catalytic Mechanism of NiFe and CoFe Layered Double Hydroxides during Oxygen Evolution. *Nat. Commun.* **2020**, *11* (1), 2522. https://doi.org/10.1038/s41467-020-16237-1.

(118) Chen, R.; Hung, S. F.; Zhou, D.; Gao, J.; Yang, C.; Tao, H.; Yang, H. B.; Zhang, L.; Zhang, L.; Xiong, Q.; Chen, H. M.; Liu, B. Layered Structure Causes Bulk NiFe Layered Double Hydroxide Unstable in Alkaline Oxygen Evolution Reaction. *Adv. Mater.* **2019**, *31* (41), e1903909. https://doi.org/10.1002/adma.201903909.

(119) Pavel, C. C.; Cecconi, F.; Emiliani, C.; Santiccioli, S.; Scaffidi, A.; Catanorchi, S.; Comotti, M. Highly Efficient Platinum Group Metal Free Based Membrane-Electrode Assembly for Anion Exchange Membrane Water Electrolysis. *Angew. Chemie Int. Ed.* **2014**, *53* (5), 1378–1381. https://doi.org/10.1002/anie.201308099.

(120) Varcoe, J. R.; Atanassov, P.; Dekel, D. R.; Herring, A. M.; Hickner, M. A.; Kohl, P. A.; Kucernak, A. R.; Mustain, W. E.; Nijmeijer, K.; Scott, K.; Xu, T.; Zhuang, L. Anion-Exchange Membranes in Electrochemical Energy Systems. *Energy Environ. Sci.* **2014**, *7* (10), 3135–3191. https://doi.org/10.1039/c4ee01303d.

(121) Xu, D.; Stevens, M. B.; Cosby, M. R.; Oener, S. Z.; Smith, A. M.; Enman, L. J.; Ayers, K. E.; Capuano, C. B.; Renner, J. N.; Danilovic, N.; Li, Y.; Wang, H.; Zhang, Q.; Boettcher, S. W. Earth-Abundant Oxygen Electrocatalysts for Alkaline Anion-Exchange-Membrane Water Electrolysis: Effects of Catalyst Conductivity and Comparison with Performance in Three-Electrode Cells. *ACS Catal.* **2019**, *9* (1), 7–15. https://doi.org/10.1021/acscatal.8b04001.

(122) Kaczur, J. J.; Yang, H.; Liu, Z.; Sajjad, S. D.; Masel, R. I. Carbon Dioxide and Water Electrolysis Using New Alkaline Stable Anion Membranes. *Front. Chem.* **2018**, *6* (JUL), 1–16. https://doi.org/10.3389/fchem.2018.00263.

(123) Thangavel, P.; Ha, M.; Kumaraguru, S.; Meena, A.; Singh, A. N.; Harzandi, A. M.;

Kim, K. S. Graphene-Nanoplatelets-Supported NiFe-MOF: High-Efficiency and Ultra-Stable Oxygen Electrodes for Sustained Alkaline Anion Exchange Membrane Water Electrolysis. *Energy Environ. Sci.* **2020**, *13* (10), 3447–3458. https://doi.org/10.1039/d0ee00877j.

(124) Koshikawa, H.; Murase, H.; Hayashi, T.; Nakajima, K.; Mashiko, H.; Shiraishi, S.; Tsuji, Y. Single Nanometer-Sized NiFe-Layered Double Hydroxides as Anode Catalyst in Anion Exchange Membrane Water Electrolysis Cell with Energy Conversion Efficiency of 74.7% at 1.0 A Cm-2. *ACS Catal.* **2020**, *10* (3), 1886–1893. https://doi.org/10.1021/acscatal.9b04505.

(125) Ruska-centre, E.; Ruska-centre, E.; Ruska-centre, E. FEI Titan 80-300 TEM Ernst Ruska-Centre for Microscopy and Spectroscopy with Electrons. *J. large-scale Res. Facil.* **2016**, *41*, 3–6.

(126) Rades, S.; Hodoroaba, V. D.; Salge, T.; Wirth, T.; Lobera, M. P.; Labrador, R. H.; Natte, K.; Behnke, T.; Gross, T.; Unger, W. E. S. High-Resolution Imaging with SEM/T-SEM, EDX and SAM as a Combined Methodical Approach for Morphological and Elemental Analyses of Single Engineered Nanoparticles. *RSC Adv.* **2014**, *4* (91), 49577–49587. https://doi.org/10.1039/c4ra05092d.

(127) Deng, Y.; Yeo, B. S. Characterization of Electrocatalytic Water Splitting and CO2 Reduction Reactions Using in Situ/Operando Raman Spectroscopy. *ACS Catal.* **2017**, *7* (11), 7873–7889. https://doi.org/10.1021/acscatal.7b02561.

(128) Griffiths, P. R. Fourier Transform Infrared Spectrometry. *Science* **1983**, *222* (4621), 297–302. https://doi.org/10.1126/science.6623077.

(129) Wang, D.; Zhou, J.; Hu, Y.; Yang, J.; Han, N.; Li, Y.; Sham, T.-K. In Situ X-Ray Absorption Near-Edge Structure Study of Advanced NiFe(OH)x Electrocatalyst on Carbon Paper for Water Oxidation. *J. Phys. Chem. C* **2015**, *119* (34), 19573–19583. https://doi.org/10.1021/acs.jpcc.5b02685.

(130) Faid, A. Y.; Barnett, A. O.; Seland, F.; Sunde, S. Ni/NiO Nanosheets for Alkaline Hydrogen Evolution Reaction: In Situ Electrochemical-Raman Study. *Electrochim. Acta* **2020**, *361*, 137040. https://doi.org/10.1016/j.electacta.2020.137040.

(131) Faid, A. Y.; Barnett, A. O.; Seland, F.; Sunde, S. NiCu Mixed Metal Oxide Catalyst for Alkaline Hydrogen Evolution in Anion Exchange Membrane Water Electrolysis. *Electrochim. Acta* **2021**, *371*. https://doi.org/10.1016/j.electacta.2021.137837.

(132) Niu, S.; Li, S.; Du, Y.; Han, X.; Xu, P. How to Reliably Report the Overpotential of an Electrocatalyst. *ACS Energy Letters*. American Chemical Society April 2020, pp 1083–1087. https://doi.org/10.1021/acsenergylett.0c00321.

(133) Welter, E.; Chernikov, R.; Herrmann, M.; Nemausat, R. A Beamline for Bulk Sample X-Ray Absorption Spectroscopy at the High Brilliance Storage Ring PETRA III. *AIP Conf. Proc.* **2019**, *2054* (January), 1–6.

https://doi.org/10.1063/1.5084603.

(134) Ravel, B.; Newville, M. ATHENA, ARTEMIS, HEPHAESTUS: Data Analysis for X-Ray Absorption Spectroscopy Using IFEFFIT. *J. Synchrotron Radiat.* **2005**, *12* (4), 537–541. https://doi.org/10.1107/S0909049505012719.

(135) Ravel, B. ATOMS: Crystallography for the X-Ray Absorption Spectroscopist. *J. Synchrotron Radiat.* **2001**, *8* (2), 314–316. https://doi.org/10.1107/S090904950001493X.

(136) Scott, F. J.; Mukerjee, S.; Ramaker, D. E. CO Coverage/Oxidation Correlated with PtRu Electrocatalyst Particle Morphology in 0.3 M Methanol by In Situ XAS. *J. Electrochem. Soc.* **2007**, *154* (5), A396. https://doi.org/10.1149/1.2709496.

(137) Calvin, S. *XAFS for Everyone*; CRC Press, 2013. https://doi.org/10.1201/b14843.

(138) Wei, C.; Rao, R. R.; Peng, J.; Huang, B.; Stephens, I. E. L.; Risch, M.; Xu, Z. J.; Shao-Horn, Y. Recommended Practices and Benchmark Activity for Hydrogen and Oxygen Electrocatalysis in Water Splitting and Fuel Cells. *Adv. Mater.* **2019**, *31* (31), e1806296. https://doi.org/10.1002/adma.201806296.

(139) Garcia, A. C.; Koper, M. T. M. Effect of Saturating the Electrolyte with Oxygen on the Activity for the Oxygen Evolution Reaction. *ACS Catal.* **2018**, *8* (10), 9359–9363. https://doi.org/10.1021/acscatal.8b01447.

(140) Mayrhofer, K. J. J.; Crampton, A. S.; Wiberg, G. K. H.; Arenz, M. Analysis of the Impact of Individual Glass Constituents on Electrocatalysis on Pt Electrodes in Alkaline Solution. *J. Electrochem. Soc.* **2008**, *155* (6). https://doi.org/10.1149/1.2904882.

(141) Jin, W.; Du, H.; Zheng, S.; Xu, H.; Zhang, Y. Comparison of the Oxygen Reduction Reaction between NaOH and KOH Solutions on a Pt Electrode: The Electrolyte-Dependent Effect. *J. Phys. Chem. B* **2010**, *114* (19), 6542–6548. https://doi.org/10.1021/jp102367u.

(142) Duan, Y.; Yu, Z.; Hu, S.; Zheng, X.; Zhang, C.; Ding, H.; Hu, B.; Fu, Q.; Yu, Z.; Zheng, X.; Zhu, J.; Gao, M.; Yu, S. Scaled‐Up Synthesis of Amorphous NiFeMo Oxides and Their Rapid Surface Reconstruction for Superior Oxygen Evolution Catalysis. *Angew. Chemie* **2019**, *131* (44), 15919–15924. https://doi.org/10.1002/ange.201909939.

(143) Wang, R.; Jiang, W.; Xia, D.; Liu, T.; Gan, L. Improving the Wettability of Thin-Film Rotating Disk Electrodes for Reliable Activity Evaluation of Oxygen Electrocatalysts by Triggering Oxygen Reduction at the Catalyst-Electrolyte-Bubble Triple Phase Boundaries. *J. Electrochem. Soc.* **2018**, *165* (7), F436–F440. https://doi.org/10.1149/2.0371807jes.

(144) Voiry, D.; Chhowalla, M.; Gogotsi, Y.; Kotov, N. A.; Li, Y.; Penner, R. M.; Schaak,

R. E.; Weiss, P. S. Best Practices for Reporting Electrocatalytic Performance of Nanomaterials. *ACS Nano* **2018**, *12* (10), 9635–9638. https://doi.org/10.1021/acsnano.8b07700.

(145) Maass, S.; Finsterwalder, F.; Frank, G.; Hartmann, R.; Merten, C. Carbon Support Oxidation in PEM Fuel Cell Cathodes. *J. Power Sources* **2008**, *176* (2), 444–451. https://doi.org/10.1016/j.jpowsour.2007.08.053.

(146) Dubau, L.; Castanheira, L.; Berthomé, G.; Maillard, F. An Identical-Location Transmission Electron Microscopy Study on the Degradation of Pt/C Nanoparticles under Oxidizing, Reducing and Neutral Atmosphere. *Electrochim. Acta* **2013**, *110*, 273–281. https://doi.org/10.1016/j.electacta.2013.03.184.

(147) Arenz, M.; Zana, A. Fuel Cell Catalyst Degradation: Identical Location Electron Microscopy and Related Methods. *Nano Energy* **2016**, *29*, 299–313. https://doi.org/10.1016/j.nanoen.2016.04.027.

(148) Garcia, A. C.; Touzalin, T.; Nieuwland, C.; Perini, N.; Koper, M. T. M. Enhancement of Oxygen Evolution Activity of Nickel Oxyhydroxide by Electrolyte Alkali Cations. *Angew. Chemie Int. Ed.* **2019**, *58* (37), 12999–13003. https://doi.org/10.1002/anie.201905501.

(149) Görlin, M.; Stenlid, J. H.; Koroidov, S.; Wang, H.; Börner, M.; Shipilin, M.; Kalinko, A.; Murzin, V.; Safonova, O. V; Nachtegaal, M.; Uheida, A.; Dutta, J.; Bauer, M.; Nilsson, A.; Diaz-morales, O. Key Activity Descriptors of Nickel-Iron Oxygen Evolution Electrocatalysts in the Presence of Alkali Metal Cations. *Nat. Commun.* **2020**, 1–11. https://doi.org/10.1038/s41467-020-19729-2.

(150) Alia, S. M.; Pivovar, B. S. Evaluating Hydrogen Evolution and Oxidation in Alkaline Media to Establish Baselines. *J. Electrochem. Soc.* **2018**, *165* (7), F441–F455. https://doi.org/10.1149/2.0361807jes.

(151) Corrigan, D. A. The Catalysis of the Oxygen Evolution Reaction by Iron Impurities in Thin Film Nickel Oxide Electrodes. *J. Electrochem. Soc.* **1987**, *134* (2), 377. https://doi.org/10.1149/1.2100463.

(152) Li, G.-F.; Yang, D.; Abel Chuang, P.-Y. Defining Nafion Ionomer Roles for Enhancing Alkaline Oxygen Evolution Electrocatalysis. *ACS Catal.* **2018**, *8* (12), 11688–11698. https://doi.org/10.1021/acscatal.8b02217.

(153) Ramírez-Rico, D. S.; Larios-Durán, E. R. Electrochemical Study on Electrodissolution of Gold in Acidic Medium Using Chlorides as Ligands. *J. Electrochem. Soc.* **2017**, *164* (14), H994–H1002. https://doi.org/10.1149/2.0351714jes.

(154) Cherevko, S.; Topalov, A. A.; Katsounaros, I.; Mayrhofer, K. J. J. Electrochemical Dissolution of Gold in Acidic Medium. *Electrochem. commun.* **2013**, *28*, 44–46. https://doi.org/10.1016/j.elecom.2012.11.040.

(155) Lee, S.; Kim, I.; Cho, H.; Kim, C.; Lee, Y. Resolving Potential-Dependent Degradation of Electrodeposited Ni(OH)2 Catalysts in Alkaline Oxygen Evolution Reaction (OER): In Situ XANES Studies. *"Applied Catal. B, Environ.* **2020**, No. July, 119729. https://doi.org/10.1016/j.apcatb.2020.119729.

(156) Qian, M.; Liu, X.; Cui, S.; Jia, H.; Du, P. Copper Oxide Nanosheets Prepared by Molten Salt Method for Efficient Electrocatalytic Oxygen Evolution Reaction with Low Catalyst Loading. *Electrochim. Acta* **2018**, *263*, 318–327. https://doi.org/10.1016/j.electacta.2018.01.053.

(157) Cui, S.; Liu, X.; Sun, Z.; Du, P. Noble Metal-Free Copper Hydroxide as an Active and Robust Electrocatalyst for Water Oxidation at Weakly Basic PH. *ACS Sustain. Chem. Eng.* **2016**, *4* (5), 2593–2600. https://doi.org/10.1021/acssuschemeng.6b00067.

(158) Wang, B.; Zhao, K.; Yu, Z.; Sun, C.; Wang, Z.; Feng, N.; Mai, L.; Wang, Y.; Xia, Y. In-Situ Structural Evolution of Multi-Site Alloy Electrocatalyst to Manipulate Intermediate for Enhanced Water Oxidation Reaction . *Energy Environ. Sci.* **2020**. https://doi.org/10.1039/d0ee00755b.

(159) Zeng, K.; Zheng, X.; Li, C.; Yan, J.; Tian, J. H.; Jin, C.; Strasser, P.; Yang, R. Recent Advances in Non-Noble Bifunctional Oxygen Electrocatalysts toward Large-Scale Production. *Adv. Funct. Mater.* **2020**, *2000503*, 1–23. https://doi.org/10.1002/adfm.202000503.

(160) Li, L.; Wang, P.; Shao, Q.; Huang, X. Metallic Nanostructures with Low Dimensionality for Electrochemical Water Splitting. *Chem. Soc. Rev.* **2020**, *49* (10), 3072–3106. https://doi.org/10.1039/d0cs00013b.

(161) Fan, K.; Chen, H.; Ji, Y.; Huang, H.; Claesson, P. M.; Daniel, Q.; Philippe, B.; Rensmo, H.; Li, F.; Luo, Y.; Sun, L. Nickel-Vanadium Monolayer Double Hydroxide for Efficient Electrochemical Water Oxidation. *Nat. Commun.* **2016**, *7*, 11981. https://doi.org/10.1038/ncomms11981.

(162) Zhou, D.; Wang, S.; Jia, Y.; Xiong, X.; Yang, H.; Liu, S.; Tang, J.; Zhang, J.; Liu, D.; Zheng, L.; Kuang, Y.; Sun, X.; Liu, B. NiFe Hydroxide Lattice Tensile Strain: Enhancement of Adsorption of Oxygenated Intermediates for Efficient Water Oxidation Catalysis. *Angew. Chemie Int. Ed.* **2019**, *58* (3), 736–740. https://doi.org/10.1002/anie.201809689.

(163) Zhang, J.; Yu, L.; Chen, Y.; Lu, X. F.; Gao, S.; Lou, X. W. D. Designed Formation of Double-Shelled Ni-Fe Layered-Double-Hydroxide Nanocages for Efficient Oxygen Evolution Reaction. *Adv. Mater.* **2020**, e1906432. https://doi.org/10.1002/adma.201906432.

(164) Dionigi, F.; Zhu, J.; Zeng, Z.; Merzdorf, T.; Sarodnik, H.; Gliech, M.; Pan, L.; Li, W. X.; Greeley, J.; Strasser, P. Intrinsic Electrocatalytic Activity for Oxygen Evolution

of Crystalline 3d-Transition Metal Layered Double Hydroxides. *Angew. Chemie Int. Ed.* **2021**, *60* (26), 14446–14457. https://doi.org/10.1002/anie.202100631.

(165) Jiang, W.; Faid, A. Y.; Gomes, B. F.; Galkina, I.; Xia, L.; Desmau, C. M. S. L. M.; Borowski, P.; Hartmann, H.; Maljusch, A.; Besmehn, A.; Roth, C.; Sunde, S.; Lehnert, W.; Shviro, M. Composition-Dependent Morphology, Structure and Catalytical Performance of Nickel Iron Layered Double Hydroxide as Highly-Efficient and Stable Anode Catalyst in Anion Exchange Membrane Water Electrolysis. *Adv. Funct. Mater.* **2022**, *2203520*. https://doi.org/10.1002/adfm.202203520.

(166) Han, Y.; Liu, Z. H.; Yang, Z.; Wang, Z.; Tang, X.; Wang, T.; Fan, L.; Ooi, K. Preparation of Ni2+- Fe3+ Layered Double Hydroxide Material with High Crystallinity and Well-Defined Hexagonal Shapes. *Chem. Mater.* **2008**, *20* (2), 360–363. https://doi.org/10.1021/cm7023789.

(167) Hunter, B. M.; Blakemore, J. D.; Deimund, M.; Gray, H. B.; Winkler, J. R.; Múller, A. M. Highly Active Mixed-Metal Nanosheet Water Oxidation Catalysts Made by Pulsed-Laser Ablation in Liquids. *J. Am. Chem. Soc.* **2014**, *136* (38), 13118–13121. https://doi.org/10.1021/ja506087h.

(168) Tang, F.; Liu, T.; Jiang, W.; Gan, L. Windowless Thin Layer Electrochemical Raman Spectroscopy of Ni-Fe Oxide Electrocatalysts during Oxygen Evolution Reaction. *J. Electroanal. Chem.* **2020**, *871*, 114282. https://doi.org/10.1016/j.jelechem.2020.114282.

(169) Frost, R. L.; Weier, M. L.; Kloprogge, J. T. Raman Spectroscopy of Some Natural Hydrotalcites with Sulphate and Carbonate in the Interlayer. *J. Raman Spectrosc.* **2003**, *34* (10), 760–768. https://doi.org/10.1002/jrs.1050.

(170) Hunter, B. M.; Hieringer, W.; Winkler, J. R.; Gray, H. B.; Müller, A. M. Effect of Interlayer Anions on [NiFe]-LDH Nanosheet Water Oxidation Activity. *Energy Environ. Sci.* **2016**, *9* (5), 1734–1743. https://doi.org/10.1039/c6ee00377j.

(171) Abellán, G.; Coronado, E.; Martí-Gastaldo, C.; Waerenborgh, J.; Ribera, A. Interplay between Chemical Composition and Cation Ordering in the Magnetism of Ni/Fe Layered Double Hydroxides. *Inorg. Chem.* **2013**, *52* (17), 10147–10157. https://doi.org/10.1021/ic401576q.

(172) Biesinger, M. C.; Payne, B. P.; Grosvenor, A. P.; Lau, L. W. M.; Gerson, A. R.; Smart, R. S. C. Resolving Surface Chemical States in XPS Analysis of First Row Transition Metals, Oxides and Hydroxides: Cr, Mn, Fe, Co and Ni. *Appl. Surf. Sci.* **2011**, *257* (7), 2717–2730. https://doi.org/10.1016/j.apsusc.2010.10.051.

(173) Grosvenor, A. P.; Kobe, B. A.; Biesinger, M. C.; McIntyre, N. S. Investigation of Multiplet Splitting of Fe 2p XPS Spectra and Bonding in Iron Compounds. *Surf. Interface Anal.* **2004**, *36* (12), 1564–1574. https://doi.org/10.1002/sia.1984.

(174) Trotochaud, L.; Young, S. L.; Ranney, J. K.; Boettcher, S. W. Nickel-Iron Oxyhydroxide Oxygen-Evolution Electrocatalysts: The Role of Intentional and Incidental Iron Incorporation. *J. Am. Chem. Soc.* **2014**, *136* (18), 6744–6753. https://doi.org/10.1021/ja502379c.

(175) Bao, F.; Kemppainen, E.; Dorbandt, I.; Xi, F.; Bors, R.; Maticiuc, N.; Wenisch, R.; Bagacki, R.; Schary, C.; Michalczik, U.; Bogdanoff, P.; Lauermann, I.; Van De Krol, R.; Schlatmann, R.; Calnan, S. Host, Suppressor, and Promoter?The Roles of Ni and Fe on Oxygen Evolution Reaction Activity and Stability of NiFe Alloy Thin Films in Alkaline Media. *ACS Catal.* **2021**, *11*, 10537–10552. https://doi.org/10.1021/acscatal.1c01190.

(176) Wu, C.; Li, H.; Xia, Z.; Zhang, X.; Deng, R.; Wang, S.; Sun, G. NiFe Layered Double Hydroxides with Unsaturated Metal Sites via Precovered Surface Strategy for Oxygen Evolution Reaction. *ACS Catal.* **2020**, *10* (19), 11127–11135. https://doi.org/10.1021/acscatal.0c02501.

(177) Liu, S.; Zhang, H.; Hu, E.; Zhu, T.; Zhou, C.; Huang, Y.; Ling, M.; Gao, X.; Lin, Z. Boosting Oxygen Evolution Activity of NiFe-LDH Using Oxygen Vacancies and Morphological Engineering. *J. Mater. Chem. A* **2021**, *9* (41), 23697–23702. https://doi.org/10.1039/d1ta06263h.

(178) Munonde, T. S.; Zheng, H.; Nomngongo, P. N. Ultrasonic Exfoliation of NiFe LDH/CB Nanosheets for Enhanced Oxygen Evolution Catalysis. *Ultrason. Sonochem.* **2019**, *59* (July), 104716. https://doi.org/10.1016/j.ultsonch.2019.104716.

(179) Grégoire, B.; Ruby, C.; Carteret, C. Hydrolysis of Mixed Ni2+–Fe3+ and Mg2+–Fe3+ Solutions and Mechanism of Formation of Layered Double Hydroxides. *J. Chem. Soc. Dalt. Trans.* **2013**, *42* (44), 15687–15698. https://doi.org/10.1039/c3dt51521d.

(180) Grégoire, B.; Ruby, C.; Carteret, C. Structural Cohesion of M II-M III Layered Double Hydroxides Crystals: Electrostatic Forces and Cationic Polarizing Power. *Cryst. Growth Des.* **2012**, *12* (9), 4324–4333. https://doi.org/10.1021/cg3006053.

(181) Steimecke, M.; Seiffarth, G.; Bron, M. In Situ Characterization of Ni and Ni/Fe Thin Film Electrodes for Oxygen Evolution in Alkaline Media by a Raman-Coupled Scanning Electrochemical Microscope Setup. *Anal. Chem.* **2017**, *89* (20), 10679–10686. https://doi.org/10.1021/acs.analchem.7b01060.

(182) Dang, L.; Liang, H.; Zhuo, J.; Lamb, B. K.; Sheng, H.; Yang, Y.; Jin, S. Direct Synthesis and Anion Exchange of Noncarbonate-Intercalated NiFe-Layered Double Hydroxides and the Influence on Electrocatalysis. *Chem. Mater.* **2018**, *30* (13), 4321–4330. https://doi.org/10.1021/acs.chemmater.8b01334.

(183) Liu, Z.; Dawar Sajjad, S.; Gao, Y.; Yang, H.; Kaczur, J. J.; Masel, R. I. The Effect

of Membrane on an Alkaline Water Electrolyzer. *Inorg. Chem. Front.* **2017**, 29661–29665. https://doi.org/10.1016/j.ijhydene.2017.10.050.

(184) Xiao, J.; Oliveira, A. M.; Wang, L.; Zhao, Y.; Wang, T.; Wang, J.; Setzler, B. P.; Yan, Y. Water-Fed Hydroxide Exchange Membrane Electrolyzer Enabled by a Fluoride-Incorporated Nickel-Iron Oxyhydroxide Oxygen Evolution Electrode. *ACS Catal.* **2021**, *11* (1), 264–270. https://doi.org/10.1021/acscatal.0c04200.

(185) Faid, A. Y.; Barnett, A. O.; Seland, F.; Sunde, S. Highly Active Nickel-Based Catalyst for Hydrogen Evolution in Anion Exchange Membrane Electrolysis. *Catalysts* **2018**, *8* (12), 1–8. https://doi.org/10.3390/catal8120614.

(186) Lim, A.; Kim, H. juhn; Henkensmeier, D.; Jong Yoo, S.; Young Kim, J.; Young Lee, S.; Sung, Y. E.; Jang, J. H.; Park, H. S. A Study on Electrode Fabrication and Operation Variables Affecting the Performance of Anion Exchange Membrane Water Electrolysis. *J. Ind. Eng. Chem.* **2019**, *76*, 410–418. https://doi.org/10.1016/j.jiec.2019.04.007.

(187) Park, J. E.; Kang, S. Y.; Oh, S. H.; Kim, J. K.; Lim, M. S.; Ahn, C. Y.; Cho, Y. H.; Sung, Y. E. High-Performance Anion-Exchange Membrane Water Electrolysis. *Electrochim. Acta* **2019**, *295*, 99–106. https://doi.org/10.1016/j.electacta.2018.10.143.

(188) Zignani, S. C.; Faro, M. Lo; Trocino, S.; Aricò, A. S. Investigation of NiFe-Based Catalysts for Oxygen Evolution in Anion-Exchange Membrane Electrolysis. *Energies* **2020**, *13* (7), 1720. https://doi.org/10.3390/en13071720.

(189) Pushkareva, I. V.; Pushkarev, A. S.; Grigoriev, S. A.; Modisha, P.; Bessarabov, D. G. Comparative Study of Anion Exchange Membranes for Low-Cost Water Electrolysis. *Int. J. Hydrogen Energy* **2020**, *45* (49), 26070–26079. https://doi.org/10.1016/j.ijhydene.2019.11.011.

(190) Cho, M. K.; Park, H. Y.; Lee, H. J.; Kim, H. J.; Lim, A.; Henkensmeier, D.; Yoo, S. J.; Kim, J. Y.; Lee, S. Y.; Park, H. S.; Jang, J. H. Alkaline Anion Exchange Membrane Water Electrolysis: Effects of Electrolyte Feed Method and Electrode Binder Content. *J. Power Sources* **2018**, *382* (February), 22–29. https://doi.org/10.1016/j.jpowsour.2018.02.025.

(191) Xia, L.; Jiang, W.; Hartmann, H.; Mayer, J.; Lehnert, W.; Shviro, M. Multistep Sulfur Leaching for the Development of a Highly Efficient and Stable NiS x/Ni(OH)2/NiOOH Electrocatalyst for Anion Exchange Membrane Water Electrolysis. *ACS Appl. Mater. Interfaces* **2022**, *14* (17), 19397–19408. https://doi.org/10.1021/acsami.2c01302.

(192) Park, J. E.; Kim, M. J.; Lim, M. S.; Kang, S. Y.; Kim, J. K.; Oh, S. H.; Her, M.; Cho, Y. H.; Sung, Y. E. Graphitic Carbon Nitride-Carbon Nanofiber as Oxygen Catalyst in Anion-Exchange Membrane Water Electrolyzer and Rechargeable Metal–Air

Cells. *Appl. Catal. B Environ.* **2018**, *237*, 140–148. https://doi.org/10.1016/j.apcatb.2018.05.073.

(193) Carbone, A.; Zignani, S. C.; Gatto, I.; Trocino, S.; Aricò, A. S. Assessment of the FAA3-50 Polymer Electrolyte in Combination with a NiMn2O4 Anode Catalyst for Anion Exchange Membrane Water Electrolysis. *Int. J. Hydrogen Energy* **2020**, *45* (16), 9285–9292. https://doi.org/10.1016/J.IJHYDENE.2020.01.150.

(194) Chen, P.; Hu, X. High-Efficiency Anion Exchange Membrane Water Electrolysis Employing Non-Noble Metal Catalysts. *Adv. Energy Mater.* **2020**, *10* (39), 1–6. https://doi.org/10.1002/aenm.202002285.

(195) Zhang, F.; Zhang, H.; Salla, M.; Qin, N.; Gao, M.; Ji, Y.; Huang, S.; Wu, S.; Zhang, R.; Lu, Z.; Wang, Q. Decoupled Redox Catalytic Hydrogen Production with a Robust Electrolyte-Borne Electron and Proton Carrier. *J. Am. Chem. Soc.* **2021**, *143* (1), 223–231. https://doi.org/10.1021/jacs.0c09510.

(196) Loh, A.; Li, X.; Taiwo, O. O.; Tariq, F.; Brandon, N. P.; Wang, P.; Xu, K.; Wang, B. Development of Ni–Fe Based Ternary Metal Hydroxides as Highly Efficient Oxygen Evolution Catalysts in AEM Water Electrolysis for Hydrogen Production. *Int. J. Hydrogen Energy* **2020**, *45* (46), 24232–24247. https://doi.org/10.1016/j.ijhydene.2020.06.253.

(197) Li, X.; Walsh, F. C.; Pletcher, D. Nickel Based Electrocatalysts for Oxygen Evolution in High Current Density, Alkaline Water Electrolysers. *Phys. Chem. Chem. Phys.* **2011**, *13* (3), 1162–1167. https://doi.org/10.1039/c0cp00993h.

(198) López-Fernández, E.; Gil-Rostra, J.; Espinós, J. P.; González-Elipe, A. R.; De Lucas Consuegra, A.; Yubero, F. Chemistry and Electrocatalytic Activity of Nanostructured Nickel Electrodes for Water Electrolysis. *ACS Catal.* **2020**, *10* (11), 6159–6170. https://doi.org/10.1021/acscatal.0c00856.

(199) McCrory, C. C.; Jung, S.; Peters, J. C.; Jaramillo, T. F. Benchmarking Heterogeneous Electrocatalysts for the Oxygen Evolution Reaction. *J. Am. Chem. Soc.* **2013**, *135* (45), 16977–16987. https://doi.org/10.1021/ja407115p.

(200) Bates, M. K.; Jia, Q.; Doan, H.; Liang, W.; Mukerjee, S. Charge-Transfer Effects in Ni–Fe and Ni–Fe–Co Mixed-Metal Oxides for the Alkaline Oxygen Evolution Reaction. *ACS Catal.* **2015**, *6* (1), 155–161. https://doi.org/10.1021/acscatal.5b01481.

(201) Zhang, B.; Wang, L.; Cao, Z.; Kozlov, S. M.; Arquer, F. P. G. De; Dinh, C. T.; Li, J.; Wang, Z.; Zheng, X.; Zhang, L.; Wen, Y.; Voznyy, O.; Comin, R.; Luna, P. De; Regier, T.; Bi, W.; Alp, E. E.; Pao, C.; Zheng, L.; Hu, Y.; Ji, Y.; Li, Y.; Zhang, Y.; Cavallo, L.; Peng, H.; Sargent, E. H. High-Valence Metals Improve Oxygen Evolution Reaction Performance by Modulating 3d Metal Oxidation Cycle Energetics. *Nat. Catal.* **2020**, No. 3, 985–992. https://doi.org/10.1038/s41929-

020-00525-6.

(202) Qiu, Z.; Tai, C. W.; Niklasson, G. A.; Edvinsson, T. Direct Observation of Active Catalyst Surface Phases and the Effect of Dynamic Self-Optimization in NiFe-Layered Double Hydroxides for Alkaline Water Splitting. *Energy Environ. Sci.* **2019**, *12* (2), 572–581. https://doi.org/10.1039/c8ee03282c.

(203) Louie, M. W.; Bell, A. T. An Investigation of Thin-Film Ni-Fe Oxide Catalysts for the Electrochemical Evolution of Oxygen. *J. Am. Chem. Soc.* **2013**, *135* (33), 12329–12337. https://doi.org/10.1021/ja405351s.

(204) Trześniewski, B. J.; Diaz-Morales, O.; Vermaas, D. A.; Longo, A.; Bras, W.; Koper, M. T. M.; Smith, W. A. In Situ Observation of Active Oxygen Species in Fe-Containing Ni-Based Oxygen Evolution Catalysts: The Effect of PH on Electrochemical Activity. *J. Am. Chem. Soc.* **2015**, *137* (48), 15112–15121. https://doi.org/10.1021/jacs.5b06814.

(205) Huang, J.; Li, Y.; Zhang, Y.; Rao, G.; Wu, C.; Hu, Y.; Wang, X.; Lu, R.; Li, Y.; Xiong, J. Identification of Key Reversible Intermediates in Self-Reconstructed Nickel-Based Hybrid Electrocatalysts for Oxygen Evolution. *Angew. Chemie Int. Ed.* **2019**, *58* (48), 17458–17464. https://doi.org/10.1002/anie.201910716.

(206) Chen, F.-Y.; Wu, Z.-Y.; Adler, Z.; Wang, H. Stability Challenges of Electrocatalytic Oxygen Evolution Reaction: From Mechanistic Understanding to Reactor Design. *Joule* **2021**. https://doi.org/10.1016/j.joule.2021.05.005.

(207) Chen, F.-Y.; Wu, Z.-Y.; Adler, Z.; Wang, H. Stability Challenges of Electrocatalytic Oxygen Evolution Reaction: From Mechanistic Understanding to Reactor Design. *Joule* **2021**, 1–28. https://doi.org/10.1016/j.joule.2021.05.005.

(208) Cherevko, S.; Zeradjanin, A. R.; Keeley, G. P.; Mayrhofer, K. J. J. A Comparative Study on Gold and Platinum Dissolution in Acidic and Alkaline Media. *J. Electrochem. Soc.* **2014**, *161* (12), H822–H830. https://doi.org/10.1149/2.0881412jes.

(209) Ma, R.; Liu, Z.; Li, L.; Iyi, N.; Sasaki, T. Exfoliating Layered Double Hydroxides in Formamide: A Method to Obtain Positively Charged Nanosheets. *J. Mater. Chem.* **2006**, *16* (39), 3809–3813. https://doi.org/10.1039/b605422f.

(210) Kang, H.; Huang, G.; Ma, S.; Bai, Y.; Ma, H.; Li, Y.; Yang, X. Coassembly of Inorganic Macromolecule of Exfoliated LDH Nanosheets with Cellulose. *J. Phys. Chem. C* **2009**, *113* (21), 9157–9163. https://doi.org/10.1021/jp900861k.

(211) Dou, R.; Ma, J.; Huang, D.; Fan, C.; Zhao, W.; Peng, M.; Komarneni, S. Bisulfite Assisted Photocatalytic Degradation of Methylene Blue by Ni-Fe-Mn Oxide from MnO4 Intercalated LDH. *Appl. Clay Sci.* **2018**, *161*, 235–241. https://doi.org/10.1016/j.clay.2018.04.020.

(212) Saiah, F. B. D.; Su, B. L.; Bettahar, N. Nickel-Iron Layered Double Hydroxide (LDH): Textural Properties upon Hydrothermal Treatments and Application on Dye Sorption. *J. Hazard. Mater.* **2009**, *165* (1–3), 206–217. https://doi.org/10.1016/j.jhazmat.2008.09.125.

(213) Dionigi, F.; Strasser, P. NiFe-Based (Oxy)Hydroxide Catalysts for Oxygen Evolution Reaction in Non-Acidic Electrolytes. *Adv. Energy Mater.* **2016**, *6* (23). https://doi.org/10.1002/aenm.201600621.

(214) Gong, M.; Li, Y.; Wang, H.; Liang, Y.; Wu, J. Z.; Zhou, J.; Wang, J.; Regier, T.; Wei, F.; Dai, H. An Advanced Ni-Fe Layered Double Hydroxide Electrocatalyst for Water Oxidation. *J. Am. Chem. Soc.* **2013**, *135* (23), 8452–8455. https://doi.org/10.1021/ja4027715.

(215) Cai, D.; Wang, D.; Liu, B.; Wang, Y.; Liu, Y.; Wang, L.; Li, H.; Huang, H.; Li, Q.; Wang, T. Comparison of the Electrochemical Performance of Nimoo4 Nanorods and Hierarchical Nanospheres for Supercapacitor Applications. *ACS Appl. Mater. Interfaces* **2013**, *5* (24), 12905–12910. https://doi.org/10.1021/am403444v.

(216) Jothi, P. R.; Shanthi, K.; Salunkhe, R. R.; Pramanik, M.; Malgras, V.; Alshehri, S. M.; Yamauchi, Y. Synthesis and Characterization of α-NiMoO4 Nanorods for Supercapacitor Application. *Eur. J. Inorg. Chem.* **2015**, *2015* (22), 3694–3699. https://doi.org/10.1002/ejic.201500410.

Band / Volume 579
Application-Specific Calibration of Condensation Particle Counters under Low Pressure Conditions
O. B. F. Bischof (2022), ix, 137 pp
ISBN: 978-3-95806-629-8

Band / Volume 580
Konzepte und Potenziale von Demonstrationsanlagen für die Produktion von erneuerbarem synthetischen Flugzeugtreibstoff als Beitrag zur Transformation der Reviere in NRW – Abschlussbericht
S. Weiske, F. Schorn, J. L. Breuer, L. Becka, N. Beltermann, N. Wegener, R. C. Samsun, P. Moser, S. Schmidt, C. Götte, E. Rietmann, U. Balfanz, A. Spieckermann, D. Beckmann, J. Edler-Krupp, F. Steffen und R. Peters (2022), 167 pp
ISBN: 978-3-95806-630-4

Band / Volume 581
Schlussbericht
Accelerating Low- carbon Industrial Growth through CCUS (ALIGN-CCUS)
S. Weiske, S. Schemme, R. C. Samsun, R. Peters, S. Troy, S. Morgenthaler, D. Schumann, P. Zapp (2022), 216 pp
ISBN: 978-3-95806-632-8

Band / Volume 582
Closed Carbon Cycle Mobility –
Klimaneutrale Kraftstoffe für den Verkehr der Zukunft
F. Schorn, J. Häusler, J. L. Breuer, S. Weiske, J. Pasel, R. C. Samsun, R. Peters (2022), 220 pp
ISBN: 978-3-95806-636-6

Band / Volume 583
Machine learning for monitoring groundwater resources over Europe
Y. Ma (2022), viii, 125 pp
ISBN: 978-3-95806-638-0

Band / Volume 584
Mechanical properties of single and dual phase proton conducting membranes
W. Zhou (2022), IV, VI, 133 pp
ISBN: 978-3-95806-645-8

Band / Volume 585
Improvements to gravity wave physics from an observational perspective
M. Geldenhuys (2022), vii, 136 pp
ISBN: 978-3-95806-647-2

Band / Volume 586
Impact of severe convection on the water vapor mixing ratio in the extra-tropical stratosphere
D. Khordakova (2022), ii, 136 pp
ISBN: 978-3-95806-648-9

Band / Volume 587
Effects of salt precipitation during evaporation on porosity and permeability of porous media
J. Piotrowski (2022), xxvii, 139 pp
ISBN: 978-3-95806-650-2

Band / Volume 588
IEK-14 Report 2022
Forschung für die Energiewende und den Wandel im Rheinischen Revier
B. Emonts (Hrsg.) (2022)
ISBN: 978-3-95806-652-6

Band / Volume 589
Oxidation of monoterpenes studied in atmospheric simulation chambers
L. L. Hantschke (2022), 188 pp
ISBN: 978-3-95806-653-3

Band / Volume 590
NiFe Layered Double Hydroxide Catalysts for Oxygen Evolution Reaction in Alkaline Water Electrolysis
W. Jiang (2022), 165 pp
ISBN: 978-3-95806-658-8

Weitere ***Schriften des Verlags im Forschungszentrum Jülich*** unter
http://wwwzb1.fz-juelich.de/verlagextern1/index.asp

Energie & Umwelt / Energy & Environment
Band / Volume 590
ISBN 978-3-95806-658-8

Mitglied der Helmholtz-Gemeinschaft

JÜLICH
Forschungszentrum